HIGH TEMPERATURE OXIDATION KINETICS OF ALUMINA FORMING STEELS FOR PETROCHEMICAL PROCESSES

by

Kao Zoua Yang

A Dissertation Submitted in

Partial Fulfillment of the

Requirements for the Degree of

Doctor of Philosophy

in Engineering

at

The University of Wisconsin-Milwaukee

December 2023

ABSTRACT

HIGH TEMPERATURE OXIDATION KINETICS OF ALUMINA FORMING STEELS FOR PETROCHEMICAL PROCESSES

by

Kao Zoua Yang

The University of Wisconsin-Milwaukee, 2023
Under the Supervision of Professor Benjamin Church

Petrochemical industries produce 14.33 million barrels of petroleum products per day and by 2023, are expected to produce over a trillion dollars in sales annually. Petroleum is the number one used fuel source and is the raw material used to produce a wide range of petrochemical products including ethylene which is the raw chemical precursors that is crucial to the polymer market. Ethylene is created by the process of cracking ethane and other hydrocarbons in steel reactors at high temperature and potentially oxidizing conditions. The cracking process produces a range of byproducts including a detrimental solid carbon, called coke, which forms on the inner walls of the ethylene cracking reactor. The coke coats the reactor and thus reduces the efficiency of the process. The coke can also attack the steel reactor material through various degradation mechanisms such as carburization, metal dusting, or related carbon-based attack. Petrochemical processors periodically stop the cracking process to "de-coke" the reactor by flowing a mixture of high-temperature (~850°C) steam and air to remove the coke deposits. This cleaning process costs the petrochemical industries over 1.3 billion dollars a year due to downtime. Additionally, the repeated cycling between carbon-rich and oxidizing atmospheres can further damage the steel

reactor tubes and reduce their lifetimes which, over the long term, create additional costs for the producers.

Ethylene production reactors have traditionally used cast heat resistant austenitic stainless-steel alloys such as HP. These traditional materials form chromium oxide scales during exposure to oxidizing conditions and are classified as chromia-forming austenitics (CFAs). Chromia has been shown to have poor chemical resistance to steam conditions in high temperatures and is vulnerable to carbon- and sulphur-containing environments (sulphur being a potential contaminant in petrochemical feedstocks).

One promising option to combat the problems is using a modified class of heat-resistant austenitic steel that is designed to form aluminum oxide scales upon exposure to oxidizing conditions. These alumina forming austenitic (AFA) alloys are intended to offer better chemical resistance to the steam and carbon-rich atmospheres found in petrochemical processing applications. As these AFA alloy systems are relatively new, detailed studies comparing the performance of CFA and AFA materials are needed to support the wider adoption of the new AFA materials in petrochemical processing systems.

AFA and CFA materials were obtained from an industrial scale production and not fabricated in the lab. Oxidation performance of AFA materials was examined in the temperature range of 700 ~ 1100°C with a focus on oxidation kinetics, observation of microstructural degradation and the analysis of oxide scale formation. Results are compared to the traditional CFA material, HP. Parabolic rate constants are determined by high temperature studies at 800°C, 850°C, and 900°C in steam and air-steam environments and are used to calculate kinetic activation energies. Furthermore, additional data such as diffusion profiles of specific elements can be determined.

This will provide conclusive data on the performance of AFAs and contribute to the first thorough study of its oxidation kinetics in steam atmospheres. Initial results show AFA samples have smaller mass gains compared to CFA which indicates superior oxidation performance. Furthermore, AFA samples containing roughly 3~4 wt% Al were shown to form uniform alumina scales when oxidized. The microstructural integrity of AFA materials near the surface had less corrosion damage compared to CFA alloys. Additionally, activation energy of AFA in steam is higher than CFA which indicates the AFAs are more stable over longer periods. Longer oxidation tests and variation of air to steam environments were performed to simulate petrochemical oxidation conditions and comprehensive comparison to CFA. These oxidation kinetics results provide a foundation that can be used to predict the material's lifetime usage. Furthermore, the comparison of the AFA to CFA is crucial in convincing a wider adoption of the application of AFA alloys in industrial use. The research study will help bring multiple stake holders in the investment of petrochemical/ethylene production industries, metal foundries, and academic research.

© Copyright by Kao Zoua Yang, 2023
All Rights Reserved

TABLE OF CONTENTS

CHAPTER

I. Introduction ……..1

1.1 Background ……...……1

1.2 Motivation ……3

1.3 Novelty ……..4

II. Literature Review ……4

2.1 Oxidation of Metals ……..4

2.2 Diffusion of Oxygen ……5

2.3 Cation and Anion Diffusion ……..6

2.4 Kinetics of Oxidation ……8

2.5 Parabolic Rate Law ……...8

2.6 Linear Rate Law ……9

2.7 Logarithmic Rate Law ……10

2.8 Parabolic Rate Constants and Activation Energy ……...11

2.9 Wagner Theory of Oxidation ……..16

2.10 Chromium Oxide and Current Applications ……17

2.11 Aluminum Oxide ……..21

2.12 Alumina in Petrochemical Industries ……22

III. Activation Energy and Oxide Performance Study of Alumina Forming Alloys ……25

3.1 Introduction ……26

3.2 Theory ……27

3.3 Methodology ……...28

3.4 Microstructural Analysis ……29

3.5 Oxidation Experiments ……...32

3.6 Mass Change Measurements ……...34

3.7 Parabolic Rate Constant of AFA – 2.6% and Other Alloys ……37

3.8 Activation Energy of AFA ……..39

3.9 Oxide Scale Thickness Prediction ……..44

3.10 SEM Analysis of Oxide Scale ……...46

3.11 XRD Analysis on the Oxide Scale ……....49

3.12 Summary ……...53

IV. Oxidation of AFA in Air-Steam Ratios ……..54

4.1 Introduction ……54

4.2 Methodology ……...55

4.3 Mass Change and Determination of Oxidation Kinetics Rate ……56

4.4 Steam Oxidation Comparison to Air-Steam Oxidation ……..…65

4.5 SEM Analysis of Air-Steam Oxidation ……...67

4.6 Summary ……..…73

V. Tracking of Aluminum in Long-Term Oxidation ……...75

5.1 Introduction ……..…75

5.2 Methodology ……...76

5.3 Mass Change and Composition Check ……...78

5.4 Microstructure of HP and AFA – 2.6% ……..80

5.5 Line Scans and Box Scans of HP and AFA – 2.6% ……....82

5.6 Summary …….93

VI. Oxide Performance on Welded Surface …….94

6.1 Introduction ……94

6.2 Methodology ……...95

6.3 Microstructure Analysis ……..…96

6.4 Line Scan of Non-weld and Welded Regions ……...100

6.5 Mass Change Analysis ……..102

6.6 Summary ……...103

VII. Conclusion ……104

7.1 Application of AFA ……..…105

7.2 Future Work ……..……106

7.3 Acknowledgements ……...106

LIST OF FIGURES

Figure 1. Ethane Consumption in U.S. [] ……..…..2
Figure 2. Oxidation kinetics and transitions of different regimes (Talekar et al.) [] …….14
Figure 3. Oxide growth of Iron in water vapor and oxygen environments (Grosvenor et al.) [] ..15
Figure 4. Table summary of linear rate constants for different gas environments (Abuluwefa et al.) [] …….16
Figure 5. Parabolic and linear behavior of ferritic stainless steels (Cheng et al.) [] ……..…..18
Figure 6. XRD analysis of the oxidized iron sample [] ……..19
Figure 7. Metal recession rates from chromia (Tedmon, Jr.) [] ……20
Figure 8. The schematic drawing of volatilization of chromia in wet oxidation environment (Tommy Sand) [] ……..…….20
Figure 9. Spallation tracking of alumina and chromia formers (Jönsson et al.) [] ……....22
Figure 10. Pore formation in the chromia scale (a) 1100°C with Cr line-scan, (b) 1200°C (Jönsson et al.) [] ……..…..22
Figure 11. Mass change comparison of AFA and CFA for oxide performance (Muralidharan et al.) [] ……..…24
Figure 12. Alumina scale formation of an AFA (Muralidharan et al.) [] ……..25
Figure 13. Ellingham Diagram [] ……...28
Figure 14. Etching setup for alumina formers ……..30
Figure 15. AFA – 2.6% microstructure, left) x100 magnification right) x50 magnification …...31
Figure 16. AFA microstructure left) x50 magnification right) x100 magnification …….31
Figure 17. AFA microstructure left) x50 magnification right) x100 magnification …….32
Figure 18. Complete steam furnace setup ……33
Figure 19. Surface area setup for trapezoidal shape ……34
Figure 20. Average mass change measurements of the alloys at 800°C ……...35
Figure 21. Average mass change measurements of the alloys at 850°C ……...36
Figure 22. Average mass change measurements of the alloys at 900°C ……...36
Figure 23. Regression data for the steam oxidized alloys under three different temperatures oxidized at 100 hours ……..38
Figure 24. Mass change per area in squared version for each temperature on the AFA and HP alloys. Linear trend setting was performed to obtain equation of the line ……..40
Figure 25. Arrhenius plots for AFA and HP alloys for activation energy calculations ……42
Figure 26. Oxide scale growth of alloy AFA – 2.6% ……...45
Figure 27. Oxide scale growth of alloy AFA – 3.9% ……...45
Figure 28. Oxide scale growth of alloy AFA – 3.8% ……...46
Figure 29. Oxide scale growth of alloy AFA – 4.7% ……...46
Figure 30. SEM image comparison of HP and AFA – 2.6% ……47
Figure 31. SEM line scan comparison of HP and AFA – 2.6% ……49
Figure 32. Spectrum of HP at the tested temperatures ……..50
Figure 33. Spectrum of AFA – 2.6% at the tested temperatures ……..51

Figure 34. Glancing incidence angles scan of AFA – 2.6% ……..52
Figure 35. Rocking curve of AFA – 2.6% at the oxide peak ……53
Figure 36. The average mass change of the alloys exposed to 100 hours of oxidation in 1:100 air-steam ratio ……...……57
Figure 37. The average mass change of the alloys exposed to 100 hours of oxidation in 1:10 air-steam ratio ……...…58
Figure 38. Regression data for the 1:100 air-steam oxidized alloys under three different temperatures oxidized at 100 hours ……...….59
Figure 39. Mass change per area in squared version for each temperature on the AFA and HP alloys for the 1:100 air-steam oxidation. Linear trend setting was performed to obtain equation of the line ……..……60
Figure 40. Regression data for the 1:10 air-steam oxidized alloys under three different temperatures oxidized at 100 hours ……61
Figure 41. Mass change per area in squared version for each temperature on the AFA and HP alloys for the 1:100 air-steam oxidation. Linear trend setting was performed to obtain equation of the line ……62
Figure 42. Plots of the percent aluminum against the activation energy for all oxidizing experiments used ……..…64
Figure 43. Steam oxidation comparison to air-steam ratios at 800°C ……..65
Figure 44. Steam oxidation comparison to air-steam ratios at 850°C ……..66
Figure 45. Steam oxidation comparison to air-steam ratios at 900°C ……..67
Figure 46. SEM image comparison of HP and AFA – 2.6% in the 1:100 air-steam ratio ……....68
Figure 47. SEM image comparison of HP and AFA – 2.6% in the 1:10 air-steam ratio ……..69
Figure 48. Line scan of AFA – 2.6%. Line starts from the cross-sectioned and into the sample past the oxide layer. Above where the line starts is the Bakelite mount material …..70
Figure 49. Line scans of AFA – 2.6% and HP at the 1:100 air-steam ratio ……71
Figure 50. Line scans of AFA – 2.6% and HP at the 1:10 air-steam ratio ……...72
Figure 51. Arbitrarily locations of HP alloy near the center with SEM-EDS composition taken at x100. The average composition is given in the bottom table ……79
Figure 52. Arbitrarily locations of AFA – 2.6% alloy near the center with SEM-EDS composition taken at x100. The average composition is given in the bottom table ...79
Figure 53. SEM images of microstructure of AFA and HP alloy at 0 hours, 100 hours, and 1000 hours ……81
Figure 54. Tabulated values of the bulk scans of AFA – 2.6% and HP alloy at 100 hours and 1000 hours ……...82
Figure 55. Example line scan that was performed on the long-term oxidized sample. The line scan graphs were then converted to tabulated values for post plotting ……...83
Figure 56. Nickel content of AFA – 2.6% and HP alloy for 0 hours and 1000 hours at 900°C ...83
Figure 57. Chromium content of AFA – 2.6% and HP alloy for 0 hours and 1000 hours at 900°C ……..84

Figure 58. Aluminum content of AFA – 2.6% for 0 hours and 1000 hours at 900°C ……..84
Figure 59. Box area scans for HP alloy at 900°C for 1000 hours ……85
Figure 60. HP alloy scans for chromium content (left) and nickel content (right) for 1000 hours at 900°C ……..86
Figure 61. HP alloy scans of both nickel and chromium comparison for 1000 hours at 900°C ..87
Figure 62. Box area scans for AFA – 2.6% at 900°C for 1000 hours ……...88
Figure 63. Box area scans for AFA – 2.6% at 900°C for 1000 hours ……...89
Figure 64. Average nickel content for AFA – 2.6% done at 900°C for 1000 hours ……90
Figure 65. Average chromium content for AFA – 2.6% done at 900°C for 1000 hours ……...91
Figure 66. AFA – 2.6% aluminum profiles for location 1 and location 2 done at 900°C for 1000 hours ……92
Figure 67. AFA – 2.6% element profiles for location 2 done at 900°C for 1000 hours ……....92
Figure 68. Schematic drawing of location of welds on samples before oxidation ……...95
Figure 69. AFA – 2.6% non-welded versus welded microstructure ……96
Figure 70. AFA – 2.6% microstructure of the welded regions across the tested temperatures …97
Figure 71. SEM images of non-welded regions and welded regions of AFA – 2.6% and HP alloy in pure steam ……...98
Figure 72. SEM images of non-welded regions and welded regions of AFA – 2.6% and HP alloy in pure steam ……...99
Figure 73. SEM images of non-welded regions and welded regions of AFA – 2.6% and HP alloy in pure steam ……100
Figure 74. AFA – 2.6% line scan of welded and non-welded region showing chromium rich phase ……101
Figure 75. The average mass change of AFA – 2.6% of welded and non-welded samples …...102
Figure 76. The average mass change of HP of welded and non-welded samples ……..103

LIST OF TABLES

Table 1. Nominal compositions of alloys used in oxidation experiments (wt. %) ……...29
Table 2. Average surface areas of alloys tested in various temperatures ……34
Table 3. Rake constant (k_p) and time exponent of rate law (n) for HP and AFA alloys at 800°C, 850°C, and 900°C ……..41
Table 4. Calculated Activation Energy of HP and AFA alloys ……43
Table 5. Summary of Activation Energy (calculated) for FeO and Chromia ……...44
Table 6. Rate constant (k) and time exponent of the rate law (n) for 1:100 and 1:10 air-steam ratios ……...63
Table 7. Calculated Activation Energy of HP and AFA alloys in Air-Steam Ratio ……63
Table 8. Mass change of HP and AFA – 2.6% for each oxidation period ……78
Table 9. Box Area scans for chromium content in HP alloy oxidized for 1000 hours at 900°C ..86
Table 10. Box Area scans for nickel content in HP alloy oxidized for 1000 hours at 900°C …..86
Table 11. Box area scans of AFA – 2.6% with tabulated aluminum values below based on distance from the top layer of oxide. Oxidation is done at 900°C for 1000 hour.....88
Table 12. Box area scans of AFA – 2.6% with tabulated aluminum values below based on distance from the top layer of oxide. Oxidation is done at 900°C for 1000 hours ...…89
Table 13. Box area scans of AFA – 2.6% with tabulated chromium values below based on distance from the top layer of the oxide. Oxidation is done at 900°C for 1000 hours .90
Table 14. Box area scans of AFA – 2.6% with the tabulated Nickel values below based on distance from the top layer of oxide. Oxidation is done at 900°C for 1000 hours …...91

LIST OF ABBREVIATIONS

AFA = Alumina Forming Alloy

CFA = Chromia Forming Alloy

EDS = Energy Dispersive Spectroscopy

HDPE = High Density Polyethylene

HSLA = High Strength Low Alloy

PEG = Polyethylene Glycol

PET = Polyethylene Terephthalate

PVC = Polyvinyl Chloride

RE = Reactive Elements

RO = Reverse Osmosis

SEM = Scanning Electron Microscopy

TGA = Thermogravimetric Analysis

UHV = Ultra High Vacuum

XRD = X-ray Diffractometer

ACKNOWLEDGEMENTS

First and foremost, I want to thank my advisor, Benjamin Church, for supporting my research and academic journey throughout my time at UWM. Additionally, his mentorship has given me many opportunities to challenge myself and gain skills that have garnered me success. I thank my wife, Chee Lee, for also her support of my final few years of my program here. She has given love and support that has boosted my morale, which was crucial in these final hours of hardship. I also thank my family as well. I want to thank my parents, May Choua Yang and Sai Mor Yang for giving me continual support throughout my life. Their prayers and love were what brought me up to this point and given me the strength to finish. I want to thank my siblings Sunny, Rebekah, Alida, Tou, and Padao along with their spouses Kai, Timmothy, and Kyu as well. My siblings and their spouse are what makes me who I am, and their support has given me strength as well to finish my degree. I also wanted to thank my niece and nephews Ezekiel Tshaj Lij, Esther Kaj Siab, Zecheriah Tshwj Xeeb and Arlo Nuj Sis Lis. They have become one of my lights in my journey and joy. They have given me the much-needed de-stress from the intense work of research and academic life. Many thanks to my close friends, Nou Kue, Touger, Mackenson, Anthony, Seanyen, Alan, TJ, Choua, Junior, and Patrick who I have become close with throughout my years. Elmer and Lizeth who are my peers in the Ph.D. program. They have given me strength and a reason to keep moving forward.

I also want to thank the Division of Diversity, Equity and Inclusion at UWM. This stems from my supervisor Dr. Sonya Martin and colleague Anique Ruiz. They have supported my journey and my academic professional career in many ways that I could not have done myself. I want to thank the multicultural office and staff who were welcoming and supportive as well. I want to thank Dr. Chia Vang who has served as a mentor and friend to me as well. Her support in my journey was instrumental to where I am now. Lastly, I want to thank the TRIO programs, from the Upward Bound Program, Student Support Services, and Ronald E. McNair Post-Baccalaureate Achievement Program as well. TRIO has served me well and given me the success I needed to complete my Ph.D. today. I also want to thank my committee members Dr. Pradeep Rohatgi, Dr. Steven Hardcastle, Dr. Xiaoli Ma, and Dr. Hamid Seifoddini for their support and advice in my dissertation committee. Finally, I want to thank God for giving me the structure and people who are in my life.

Chapter I

Introduction

1.1 Background

Every day, petrochemical industries produce over 14.33 million barrels of petroleum products a day. It has been estimated by the year 2023; petroleum product sales will exceed a trillion dollars. Petroleum is the number one used fuel source and as such a large contributor in the world economy. Petroleum as a raw material is used to produce a wide range of petrochemical products such as fuel products which includes ethylene. Ethylene is important as it is the raw chemical precursor used in the polymer market. Ethylene is created in the process of cracking ethane and other hydrocarbons in steel reactors. The cracking process is done at high temperature and potentially oxidizing conditions. Ethane is used primarily due to its higher efficiency yield of ethylene compared to other hydrocarbons. In part of preferred use of ethane, the consumption of ethane for ethylene production has been increasing since 2011 as seen in figure 1. As mentioned before, ethylene is the raw chemical precursor to create polymers.

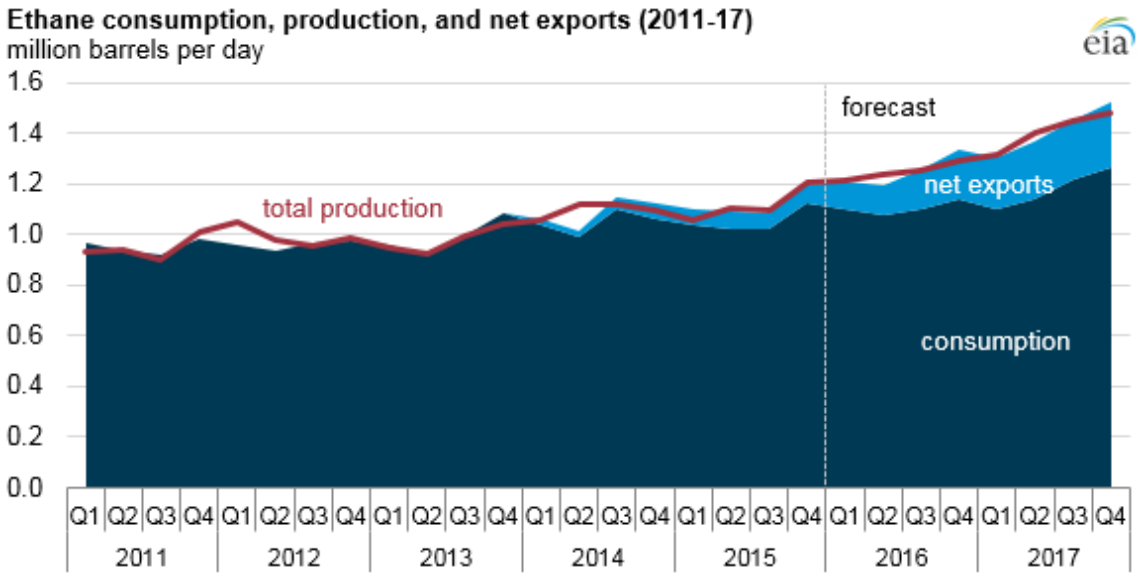

Figure 1. Ethane consumption in U.S. [1]

Some of the common polymers formed from ethylene are low-density polyethylene (LDPE), high-density polyethylene (HDPE), poly-ethylene glycol (PEG), poly-vinyl chloride (PVC) and poly-ethylene terephthalate (PET). Due to the high demand and use of ethane, ethane is used daily in the steam cracking process which leads to issues.

In addition to ethylene, the cracking process produces a range of other byproducts such as detrimental solid carbon, called coke. Coke is formed on the inner walls of the ethylene cracking reactor. The coke coats the reactor which results in reduction of efficiency in the process. Furthermore, coke can also attack the steel reactor material through many forms of degradation mechanisms which include carburization, metal dusting, and/or related carbon-based attack. The prevent the efficiency and degradation mechanisms, petrochemical processors periodically stop the cracking process to “de-coke” the reactor by flowing a mixture of high-temperature steam and air to remove the coke deposits. High temperatures of ~850°C are typically used to de-coke the steel reactors. However, with repeated cycling between cooking and de-coking atmospheres, it also leads to problems due to the oxidizing atmosphere de-coking creates. Oxidizing

atmospheres can reduce the lifetime of the steel reactors over the long term and incur additional costs for the petrochemical producers.

1.2 Motivation

The de-coking process is necessary however it ends up costing the petrochemical industries over 1.3 billion dollars a year due to downtime. As with all businesses, generating revenue and reducing costs is critical to their success. To reduce or remove downtime from corrosion related issues boosts revenue with more uptime to produce ethylene and reduces maintenance costs. With the cost reduced from reduction of downtime, money can be invested in other areas to improve marketing, product development, company outreach etc....

Ethylene production reactors have traditionally used cast heat resistant austenitic stainless-steel alloys such as High-Performance (HP) alloys. These HP alloys form chromium oxide scales during exposure to oxidizing conditions and are classified as chromia-forming alloys (CFAs). Chromium is used primarily for its easy formation of a passive layer and therefore good corrosion resistance. However, CFAs have been shown to have poor chemical resistance to steam conditions in high temperatures and are vulnerable to carbon and Sulphur containing environments. At temperatures above 900°C in steam conditions, chromium oxide begins to degrade and volatize [2,3,4].

One promising option to combat the problems is using a modified class of heat-resistant austenitic steel that is designed to form aluminum oxide scales upon exposure to oxidizing conditions. This alumina forming austenitic (AFA) alloys are intended to offer better chemical resistance to the steam and carbon-rich atmosphere found in petrochemical processing

applications. Aluminum oxide does not volatilize in the same condition as chromium and therefore serves as a promising choice in materials selection for the steel reactors.

1.3 Novelty

As AFA alloy systems are relatively new, detailed studies comparing the performance of CFA and AFA materials are needed to support the wider adoption of the new AFA materials in petrochemical processing systems. There have been some oxidation studies of the AFA however the conditions are not varied. This research will contribute to the first thorough study of oxidation kinetics in steam atmospheres. Oxidation performance of AFA materials has been examined in the temperature range of 700~1100°C with a focus on oxidation kinetics, observation of microstructural degradation and the analysis of oxide scale formation. Furthermore, additional data such as diffusion profiles of specific elements can be determined too.

Chapter II

Literature Review

2.1 Oxidation of Metals

Oxidation is described as the chemical reaction between metal and oxygen where oxygen bonds to the metal atom forming an oxide. The most observed example of oxidation is rust which is found in cars and metal structures. The formula below is the general oxidation reaction between a metal ion and oxygen ion where a and b are stoichiometric values.

Equation 1

$$aM + \frac{b}{2}O_2 \rightarrow M_aO_b$$

When the metal surface is exposed to oxygen, is then dissolved, or diffused into the surface of the metal. Oxygen is diffused through the lattice that includes defects found within the metal's surface. Diffusion of oxygen allows the reaction and formation of oxides which changes mechanical, electrical, and chemical properties of the material. Oxidation of the metals can be affected by the orientation of the surface, crystal defects, surface preparation and impurities. These variables lead to how the oxide is formed on the metal surface.

2.2 Diffusion of Oxygen

The amount of oxygen passing through the metal layer can be defined as the flux of oxygen. The flux of oxygen is described by Fick's law of diffusions. Fick's first law is a description of material flux through concentration. As the flux of material passes through the concentration, there is a concentration gradient which can be related back to diffusion rate. Fick's first law is given below where $\frac{\partial c}{\partial x}$ is given as the concentration gradient and D is the diffusion coefficient. However, Fick's first law of diffusion can only be applied to steady state situations and therefore limited.

Equation 2

$$J = -D(\frac{\partial c}{\partial x})_t$$

For more realistic and non-steady state situations, a more complicated description of diffusion is needed. This leads to Fick's second law of diffusion. Fick's second law describes diffusion as the concentration gradient changing with respect to time. Fick's second law is more useful and practical as in real life situations we encounter such a phenomenon where the

concentration profile of the material diffusing is changing. Fick's second law is given below where $\frac{d^2c}{dx^2}$ is the second order differential equation of the concentration gradient and $\frac{\partial c}{\partial t}$ is the accumulation or depletion of the concentration as time changes.

Equation 3

$$\frac{\partial c}{\partial t} = D\frac{d^2c}{dx^2}$$

Fick's second law is given an initial condition and two boundary conditions, a solution to the formula can be obtained. Different solutions have been obtained and applied to applicable world conditions. Mejlbro et al. looked at solutions to Fick's second law on applications with time-dependent diffusion coefficients and surface concentrations [5]. Another application using Fick's second law looks at porous medias such as membranes. A study by Conti et al. applied Fick's second law for an application of a non-steady state diffusion of the membrane potential in ion exchangers with fixed sites [6].

As mentioned in Fick's first law of diffusion there is a diffusion coefficient, D, that is associated with the formulation of flux. The diffusion coefficient is given experimentally by the formula below where D_0 is the "temperature independent" pre-exponential, R is the gas constant, T is temperature and Q is the activation energy. The unit is expressed in centimeter square per second (cm2/s) and is a physical constant depending on atom size.

Equation 4

$$D = D_0 \exp\left(-\frac{Q}{RT}\right)$$

The diffusion coefficient is also dependent on temperature too where higher temperatures give higher diffusion. Later the activation energy will be discussed on its usefulness in oxidation kinetics.

2.3 Cation and Anion Diffusion

Diffusion can be further explained into different types, cation, and anion diffusion. Diffusion mechanisms that occur primarily in oxides are found in lattice sites. Vacancy and interstitial defects provide a pathway that would allow diffusion to occur. It is more common and easier for diffusion to occur through vacancies rather than interstitials. This is due to the energy costs of having atoms push through interstitial sites is much higher than open vacancy sites. With cation and anion diffusion, there are also the associated cation and anion defects. Cation defects come with two possibilities, deficit, or excess of the metal. In metal deficiencies, the metal oxide is made up mostly of metal ion vacancies thus leading to a deficit of metal. In oxides with excess amount of metal, the metal ions are in interstitial sites. Many of these cation defects will cause the stoichiometric oxygen to metal to be shifted and become nonstoichiometric. The cation defect can be expressed in terms of Kroger Vink notation in the form below where V_M^x is the metal vacancy, MO is the metal oxide and K_3 is the equilibrium constant.

Equation 5

$$\frac{1}{2}O_2 \overset{K_3}{\leftrightarrow} V_M^x + \mathbf{MO}$$

Whereas cation defects had a deficit or excess amount of metal, anion defects have a deficit or excess amount of oxygen. In oxygen deficient oxides, there are a larger amount of oxygen vacancies that are formed. In oxides that have excess oxygen, they are similarly located in interstitial sites. These excess and deficit amounts of oxygen will again shift the stoichiometry of the composition to a nonstoichiometric. The Kroger Vink notation below expresses the anion defects in the oxide where V_O^x is the vacancy of oxygen, $\frac{1}{2}O_2^{(g)}$ is the oxygen not bounded to the composition and K_1 is the equilibrium constant. Cation diffusion occurs when the diffusion coefficient of the cation is greater than the diffusion coefficient of the oxygen and anion diffusion

occurs when the diffusion coefficient of the oxygen is greater than the diffusion coefficient of the cation.

Equation 6

$$O_O \overset{K_1}{\leftrightarrow} V_O^x + \frac{1}{2}O_2^{(g)}$$

2.4 Kinetics of Oxidation

With oxidation occurring in metals, it is important to not only understand the defects but to quantify the reaction rates. Quantifying the rates allows the better understanding of performance of the materials and understanding of conditions in which reactions form and quantification of energy costs. Reaction rates for oxidation depend on temperature, oxygen pressure, reaction time, surface preparation and any prior pretreatment of material. As the metal oxidizes, rate equations are fitted into three classical equations. These equations fall under different rate equation laws; logarithmic, parabolic, and linear.

Experimentally, kinetics of oxidation can be calculated from mass change measurements. During experiments, mass changes are tracked and considered from different time intervals. This allows the plotting of mass changes in respect to time. This is important as the slopes from these graphs allow the extraction of kinetics information known as the rate constants. The rate constant is typically denoted as k_p. Rate constants or specifically reaction rate constants are used often in kinetic studies and used to quantify the speeds of which reactions form.

2.5 Parabolic Rate Law

Parabolic behavior is often observed at high temperatures and is common to many metals. Although higher temperature is often subjective to the user, this implies temperatures in the range of 600°C and higher. In parabolic rate behavior, the thermal diffusion process is the rate-

determining variable. The parabolic rate equation is represented by the differential equation below. Where $\frac{dx}{dt}$ is the change in thickness over time, k'_p is the parabolic rate constant and x is the thickness.

Equation 7

$$\frac{dx}{dt} = \frac{k'_p}{x}$$

Solving the formula for x and integration, the thickness can be obtained in the new formula below. Due to integration, the thickness, x is now squared and where t is time and c_p is the integration constant.

Equation 8

$$x^2 = k_p t + c_p$$

In experimental practicality, measuring the thickness of the oxide during oxidation growth can be challenging. Too account for this challenge, in the formula, x^2 can also be represented with Δm^2 instead. Here Δm^2 represents the change in mass squared. This is more ideal and advantageous for experimental work as measuring the difference in weight changes due to oxidation is much simpler than the latter. Parabolic rate oxidation typically entails a uniform diffusion with both oxygen and metal ions through a growing oxide scale. This mechanism of oxidation can also be related back to the famous Wagner theory of oxidation which will be discussed later.

2.6 Linear Rate Law

Linear rate law is observed in steady state conditions as the rate of reaction is constant with time. With linear relationship, the rate determining factor is the surface where the oxidation reaction occurs. As a steady-state situation, the reaction is typically restricted to the amount of oxygen available at the surface which determines the reaction of oxidation. Linear rate formula is expressed below where $\frac{dx}{dt}$ is the change in thickness over time and k_l is the parabolic rate constant.

Equation 9

$$\frac{dx}{dt} = k_l$$

If we set the formula to solve for thickness and integrate it, we obtain the formula below where x is the thickness, k_l is the linear rate constant, t is time and c_i is the integration constant.

Equation 10

$$x = k_l t + c_i$$

2.7 Logarithmic Rate Law

At lower temperatures, most metals observe the logarithmic rate law. This temperature range is typically around 400°C and below. The logarithmic rate law is used because in this temperature range, most metals oxidize quickly in the early process to a maximum then with the oxidation reaction rate dropping off to negligible values. In logarithmic rate law behavior, it can be described in two different rate equations. They are categorized into direct and inverse logarithmic rate equations. These equations are listed below.

Equation 11

Direct: $$x = k_{log} \log(t + t_0) + A$$

Equation 12

Inverse: $\frac{1}{x} = \boldsymbol{B - k_{il} log t}$

With the listed equations above x is the thickness, k_{log}/k_{il} are the logarithmic rate constants, t is the time and $A/\ B$ are constants.

2.8 Parabolic Rate Constants and Activation Energy

Due to the nature of the experiments that will be performed at high temperatures, parabolic rate law is the most ideal rate law that will be considered. As discussed earlier, rate constants are obtained from the slopes of the mass change and time graphs. When parabolic rate law is observed the curve of the graph is as the name implies parabolic in shape. A common way to determine if the experimental data follows parabolic law is to linearize the graph.

Linearizing a parabolic graph is done by taking the logarithmic of both the mass changes and time axis. The experimental data should show a linearized line compared to the parabolic line that was previously shown. Furthermore, the slope of the linearized graph can be taken. This theory is applied from the formula below where x is the thickness, t is the time, c' is the constant and m is the determining factor for type of rate law.

Equation 13

$$\boldsymbol{\log x = \frac{1}{m} \log t + c'}$$

In this formula, $\frac{1}{m}$ is given by the slope of the linearized graph. If the slope has a value of 0.5 or values close to it, it can be suggested that the linearized data follows parabolic rate law. Similarly, if the value of the slope is close to or one, it follows linear rate law and if the value of the slope is close to or 0.33, it follows logarithmic rate law.

Using equation 8, we can solve for the thickness by taking the square root of each side. Relating that to the graphing component, we can plot the thickness or in this case, the mass change with

respect to the square root of time. As mentioned before, the slope of this graph is related back to the parabolic rate constant. Because of this, it is implied that the parabolic rate constantly changes at different temperatures as the weight changes are dependent on the temperature. If parabolic rate constants are obtained at various temperatures, derivation of the activation energy can be done.

Monceau et al. looked at mass-gain curves for various alloys and was able to determine parabolic rate constants from the oxide growth data [7]. They investigated oxidation of pure nickel, single-crystal Ni-based super alloy and Nb-Ti-Al alloy. The standard parabolic model equation was fitted but found to not be as accurate. They proposed a more general formula to use which allowed for pure diffusion control, mixed diffusion control and calculation of instantaneous values of parabolic rate constants.

Activation energy is given by the formula where k is the parabolic rate constant, k_0 is the pre-exponential factor, R is the gas constant, T is the temperature and Q is the activation energy.

Equation 14

$$\boldsymbol{k = k_0 \exp\left(-\frac{Q}{RT}\right)}$$

Manipulating equation 14, we can solve for Q by applying the natural log on both sides. Plotting the data of the natural log values of the parabolic rate constants at various temperatures with respect to the inverse temperature gives the slope as $\frac{-Q}{R}$. Taking the slope value and the product of the gas constant, we can obtain the activation energy for the oxidation of the alloy. Activation energy is important in kinetics due to the information it entails. Activation energy is the barrier or cost of energy the reaction needs to overcome for the reaction to proceed. In the case of oxidation, it is the energy required to form an oxide on the surface. Activation energy is

typically measured in joules or kilojoules per mole. Determining the activation energies of each oxide from metals allows the classification of oxide performance in terms of relative ease of forming, stability, and application use.

The activation energies of commercial based stainless steels have been extensively studied. Langevoort et al. has investigated the kinetics of oxidation of austenitic stainless steels [8]. They performed oxidation tests in ultra-high vacuum (UHV) system on AISI 304 and Incoloy 800H alloys at 300K-720K range. Due to the nature of the UHV system, the oxygen pressure can be varied to study its effect with temperature. Langevoort et al. also found that at low temperatures both alloys experienced logarithmic rate behavior and at high temperatures above 470K, both alloys experienced parabolic rate behavior. The overall low temperature oxidation activation energy was determined from the slope of the change in ellipsometry parameter per change in time versus the inverse temperature at a value of ~100 kJ/mol.

In addition to commercial based alloys, high strength low alloy (HSLA) steels have been studied at high temperatures too. Talekar et al. studied two HSLA steels (Mn 24 and SS46) using thermogravimetric analysis (TGA) to oxidize at 600 to 900°C [9]. In this study, two different oxidation kinetics were observed, and they were oxidized for 100 hours. The first oxidation kinetics the HSLA alloys experienced was a linear regime where eventually it transitions into a parabolic regime. Figure 2 depicts the transitioning of the different oxidation kinetics during oxidation. Talekar et al. was able to obtain activation energies for the HSLA where it was found to be ~82 kJ/mol for Mn24 and ~ 102 kJ/mol for SS46 which reflects well with other literature.

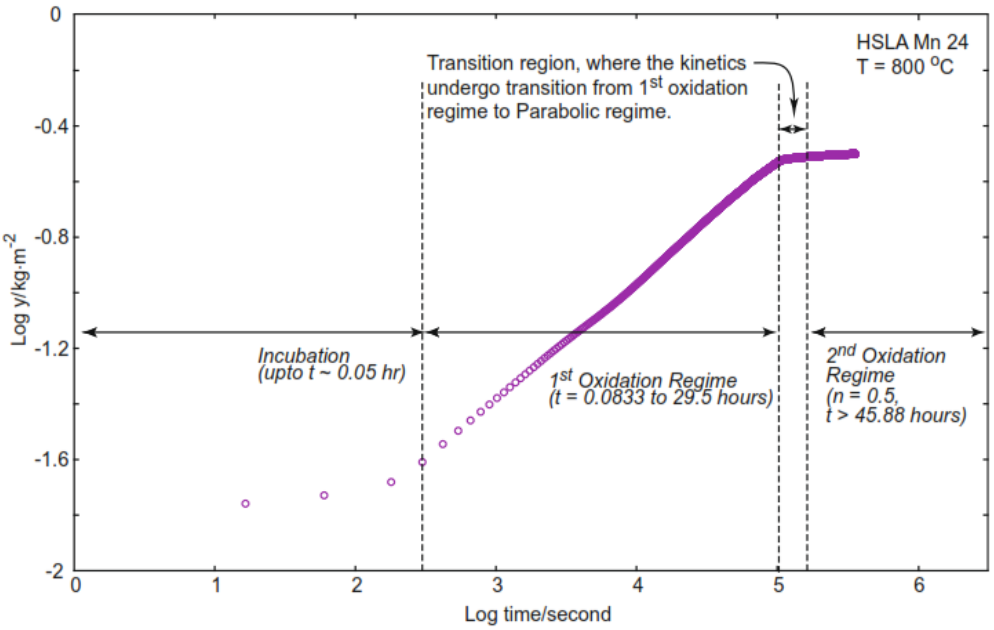

Figure 2. Oxidation kinetics and transition of different regimes (Talekar et al.) [9]

Furthermore, Grosvenor et al. investigated determining activation energies for oxidation of pure iron in oxygen and water vapor conditions [10]. The thickness of the oxide formed in these environments was recorded and displayed parabolic rate conditions as seen in figure 3. Their study also investigated identification of the rate-determining step for the reactions. Grosvenor et al. concluded that in the studies between water vapor and oxygen environments, the activations energies were calculated to be the same values within range of standard deviation. This further concluded that the rate-determining step is suggested to be by place exchange.

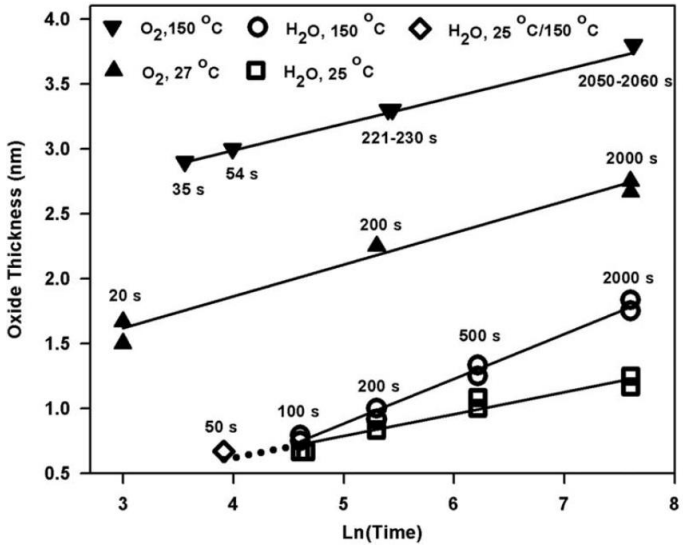

Figure 3. Oxide growth of Iron in water vapor and oxygen environments (Grosvenor et al.) [10]

In a different class of metals, low carbon steel has also been studied with varying atmospheres compared to the typical steam. Abuluwefa et al. work on oxidation of low carbon steels in multicomponent gases was used to obtain activation energies in different gas environments and observation of different oxidation kinetics [11]. The low carbon steel content for the oxidation study was measured at 0.04 wt. % and was tested over a range of 800 to 1150°C for 60 minutes. The gas systems comprised of binary and ternary gases in which at each temperature the linear rate constants were obtained. Figure 4 depicts the summary table of the data that was collected. Abuluwefa et al. concluded with binary gas systems, oxidation kinetics followed linear rate laws and ternary gas systems followed linear rate laws with later transitions into parabolic rate laws. Additionally, activation energies for CO_2 and H_2O were obtained at ~274 kJ/mol and ~264 kJ/mol respectively in their study. This work was consistent with what previous studies found in other types of alloys where linear rates are always observed first with parabolic rates at the latter. Carbon steel is typically harder to oxidize than other systems which are due to the higher activation energy. A review study by Chen et al. has been performed to compare most of the iron and carbon steels in air and oxygen environments [12].

Table II. Linear Rate Constants for Oxidation of Low Carbon Steel in Binary Gases of O_2-N_2, CO_2-N_2, and H_2O-N_2 at Various Temperatures*

	6 Pct O_2-94 Pct N_2			10 Pct CO_2-90 Pct N_2		10 Pct H_2O-N_2	
T (°C)	k_{l,O_2} (m)	k_{l,O_2} (c)	ΔT_{max}	k_{l,CO_2} (m)	K_{CO_2} (c)	k_{l,H_2O} (m)	K_{H_2O} (c)
1150	7.52	8.30	48	0.890	1.56×10^{-6}	0.970	3.57×10^{-6}
1100	7.50	7.28	51	0.350	6.93×10^{-7}	0.872	3.21×10^{-6}
1050	7.70	7.25	57	0.112	2.21×10^{-7}	0.553	1.56×10^{-6}
1000	7.95	6.58	66	0.018	3.63×10^{-8}	0.018	5.19×10^{-7}
900	6.85	6.42	62			0.004	9.82×10^{-8}

*k_l = (g/cm² s) × 10^5; and K = (g/cm² s atm).
m: measured; and c: calculated.

Table III. Linear Rate Constants for Oxidation of Low Carbon Steel in Ternary Gases of O_2-CO_2-N_2 and O_2-H_2O-N_2 at Various Temperatures*

	6 Pct O_2-6 Pct CO_2-N_2			6 Pct O_2-10 Pct CO_2-N_2			6 Pct O_2- 3 Pct H_2O-N_2			6 Pct O_2- 6 Pct H_2O-N_2		
T (°C)	$k_{l,t}$ (m)	$k_{l,t}$ (c)	ΔT_{max}	$k_{l,t}$ (m)	$k_{l,t}$ (c)	ΔT_{max}	$k_{l,t}$ (m)	$k_{l,t}$ (c)	ΔT_{max}	$k_{l,t}$ (m)	$k_{l,t}$ (c)	ΔT_{max}
1150	8.80	9.45	52	9.77	9.52	59	8.98	8.15	50	12.83	8.57	52
1100	7.60	9.25	59	9.40	9.25	61	8.20	7.87	52	7.67	8.05	51
1050	7.98	9.15	61	8.12	9.15	62	8.15	7.72	55	8.17	7.82	52
1000	8.53	8.98	65	7.78	8.98	65	7.33	7.52	58	7.87	7.57	56
950	6.75	8.90	60	7.43	8.90	66	6.78	7.43	58	5.72	7.45	43
900	5.86	8.75	55	6.32	8.73	56	5.43	7.28	60	6.12	7.30	51

*$k_{l,t}$ = (g/cm² s) × 10^5.
Subscript t: total; m: measured; and c: calculated.

Figure 4. Table summary of linear rate constants for different gas environments (Abuluwefa et al.) [11]

It is also important to note the importance and accuracy of the reported values for the reaction rate constants that are used in the activation energy calculation. The reliability of the data and calculations is crucial and should be discussed. In typical settings error bars are used for statistical analysis to determine the variation of the obtained data. For most experimental work, this is required to see any variations. However, with kinetic studies, it has been a standard practice from 40+ years to not report graphs with error bars in the kinetic studies. For example, the weight gain or mass change graphs have been historically and recently reported to not have error bars. Studies published by Adomako et al. (2017) [13], Abuluwefa et al. (1997) [11], Fujii et al. (1964) [14], and Bittel et al. (1969) [15] all report mass change data without error bars. Furthermore, these studies also use the reaction rate constants for each temperature data point to determine activation energies. However, again the authors do not use error bars in the graphs. What is common instead is to linearize the data and apply a linear trend set. To determine the reliability of your data, the R^2 value of your trendline is then used.

2.9 Wagner Theory of Oxidation

Wagner theory of oxidation is used to describe high temperature oxidation which applies to the parabolic rate law. In this theory, it assumes several assumptions that need to be made. The assumptions are as follows: 1) The oxide is compact and uniform throughout 2) Through a cross-sectional area, the transport of ions and electrons through the oxide scale is the rate-determining process 3) Between the non-metal and scale at gas/scale interface and between metal and scale at the interface exists a local equilibrium 4) In the oxide scale, there also exists a local equilibrium between neutral species, ions, defects, and electrons 5) In the oxide scale, there is a local electrical neutrality 6) Finally, the oxide is in quasi-steady-state flux.

With the formation of the compact scale, the oxide becomes a barrier and separates the metal from the oxygen gas. Wagner oxidation theory provides a good basis of fundamental understanding of parabolic oxidation with metals at high temperature. It also describes how partial pressures of oxygen affect the formation of the oxide scale along with creating defects within the scale. This allows the explanation of creating and exploiting the oxide scales for many different applications uses. Current example uses of oxides are chromium oxide, aluminum oxide and titanium oxide. Studies have shown to apply Wagner's theory to oxide formation that contains various kinds of lattice defects such as work done by Gesmundo et al. [16].

2.10 Chromium Oxide and Current Applications

Chromium oxide or also known as chromia, is when chromium reacts with oxygen and forms Cr_2O_3. Metals that have formation of chromia are known as chromia forming alloys (CFA). Chromia is very important in stainless steel. Chromia allows for the generation of the passive layer which protects the metal from further oxidation damage. Stainless steel has many uses which range from household appliances, construction materials, car parts, and jewelry. Stainless steel usually comes in two phases, austenitic and ferritic. Ferritic steels are magnetic in nature

whereas austenitic is not. Ferritic steels tend to be more ductile than austenitic steels and is characterized by their body-centered cubic structure whereas austenitic is face-centered cubic structure. Due to chromia's oxidation resistance, it is highly useful for many applications in environments where oxidation is an issue.

Ferritic steels have also been researched in oxidation studies too. A study by Cheng et al. investigated oxidation and degradation of ferritic stainless steels at 1200°C using TGA [17]. In the study, three different ferritic steels were selected and oxidized. While two of the three steels experienced parabolic rate behavior, and one experienced linear rate behavior as seen in figure 5.

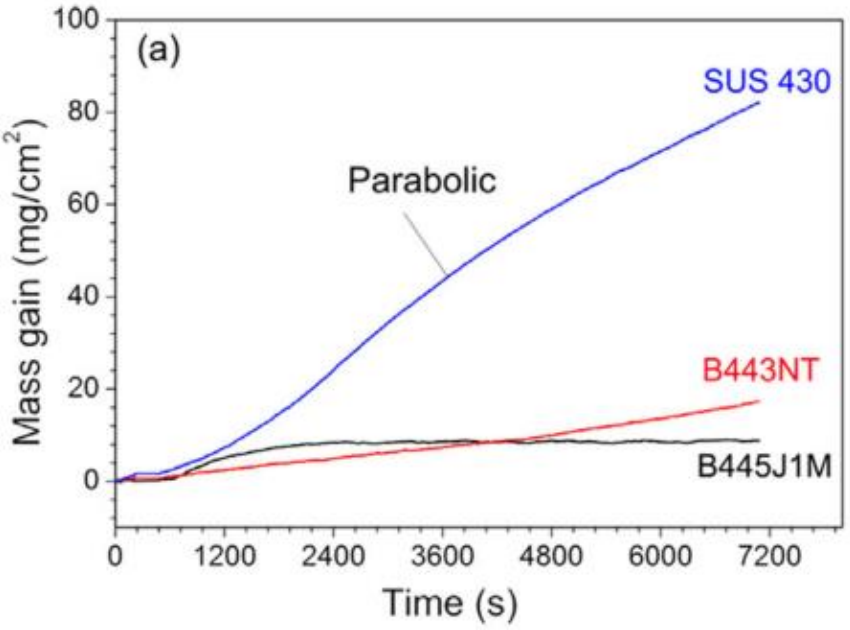

Figure 5. Parabolic and linear behavior of ferritic stainless steels (Cheng et al.) [17]

Cheng et al. also obtained parabolic and linear rate constants for the oxidation at 1200°C. Furthermore, characterization of the iron oxide that was formed was confirmed with x-ray diffraction (XRD), showing success in formation of the different iron oxide as seen in figure 6. Cheng et al. compared the chromium content between the stainless steels.

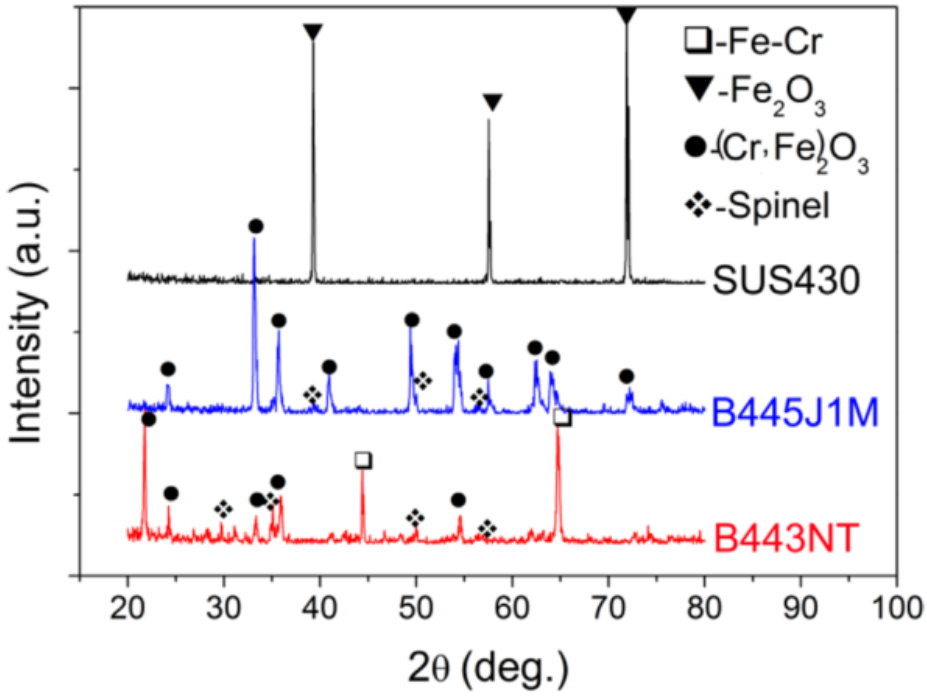

Figure 6. XRD analysis of the oxidized iron sample [17]

Moreover, an industry use of chromia is with the petroleum industries. Current industry standard employs the use of austenitic chromia forming alloys for cracking ethane. Although chromia is currently used, it presents some issues. Chromia although resistant to oxidization, does not perform well at temperatures above 900°C and volatile to steam conditions [2,3,4]. This has led to further study of a different oxide that performs better in certain environments.

The volatilization of chromia has been investigated in a prior study. An examination of the volatilization effects and scale growth of chromia was looked at by Tedmon, Jr. [18]. In this case, the growth of oxide scale followed a parabolic to linear oxidation kinetics. Tedmon, Jr. also looked at the metal recession rates from volatilization of chromium from the oxide. As the temperature of oxidation increases, the metal recession of the oxide was higher. Figure 7 shows the metal recession rates with respect to the different temperatures of oxidation. Additionally, a

study on chromia and alumina forming alloys by Sand discussed the volatilization of chromia in water vapor [19]. Figure 8 is obtained from the dissertation and depicts a detailed schematic of the process of chromia volatizing.

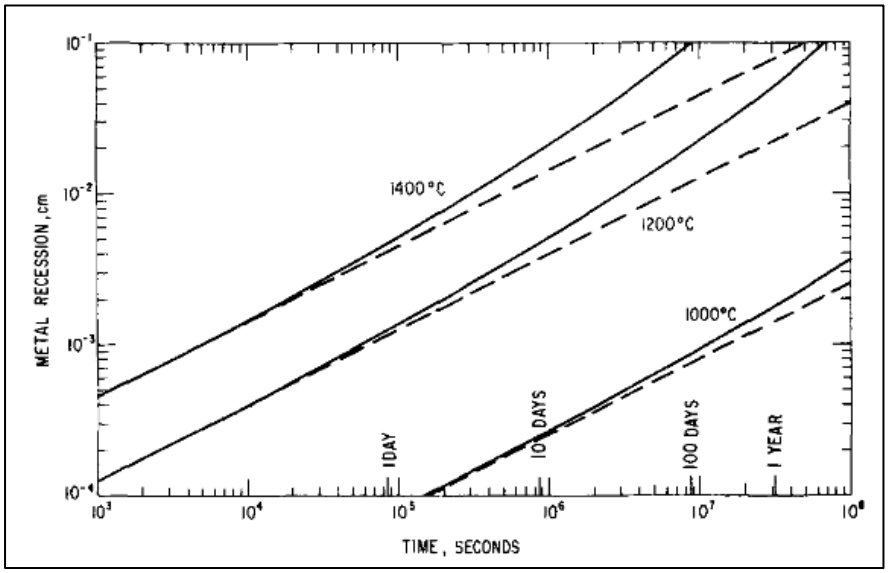

Figure 7. Metal recession rates from chromia (Tedmon, Jr.) [18]

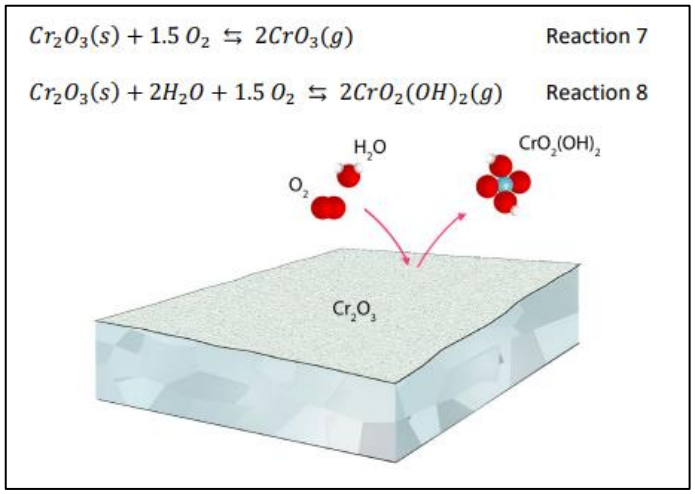

Figure 8. The schematic drawing of volatilization of chromia in wet oxidation environment (Tommy Sand) [19].

2.11 Aluminum Oxide

Aluminum oxide or also known as alumina, is quite common and naturally occurring in nature as a mineral. Alumina is formed when oxygen and aluminum react together to form aluminum oxide with the compound Al_2O_3 being the most common form. According to the Ellingham diagram, alumina is lower on the Gibbs free energy scale which states that it is more stable than chromia. Due to higher stability, aluminum oxide is preferred over chromia in many applications.

In Fe-Cr-Al alloys reactive elements (RE) are added to help aid in forming alumina scales. Fe-Cr-Al alloys are studied due to their use in car catalyst carriers and gas burners. Quadakkers et al. has investigated Fe-Cr-Al alloys that have RE elements incorporated in their composition for growth rates of alumina [20]. RE such as hafnium, zirconium and yttrium were doped into the Fe-Cr-Al alloys. Quaddakkers et al. found rather than a straight parabolic growth rate of alumina, there is a transient-oxide formation first which then was followed by a parabolic rate growth of α-alumina. They also found that the growth rate was more sub-parabolic to near-cubic growth rates due to scale cracking from thermal cycling and internal oxidation from RE.

Some studies such as looking into alumina and chromia spallation and structural defects. Jönsson et al. performed experiments on various chromia and alumina forming alloys at 1100 and 1200°C and up to 1000 hours [21]. At these higher aggressive temperatures, the oxides can start to spall off and it greatly affects oxidation. Jönsson et al. in addition to standard measurements of mass-weight changes, they also tracked the spallation of the various alloys. Figure 9 shows the tracking of spallation at 1200°C oxidation experiment of the alloys. In addition to spallation studies, Jönsson et al. characterized the voids that were present in the oxides from 1000-hour exposure. The chromia formers consumed chromium at the surface with

outward diffusion of the metal cations and allowed the inward diffusion of oxygen or vacancies to occur. The results of this are given to the pores that were seen in figure 10. Jönsson et al. concluded that out of the various alloys' alumina was the better protective oxide.

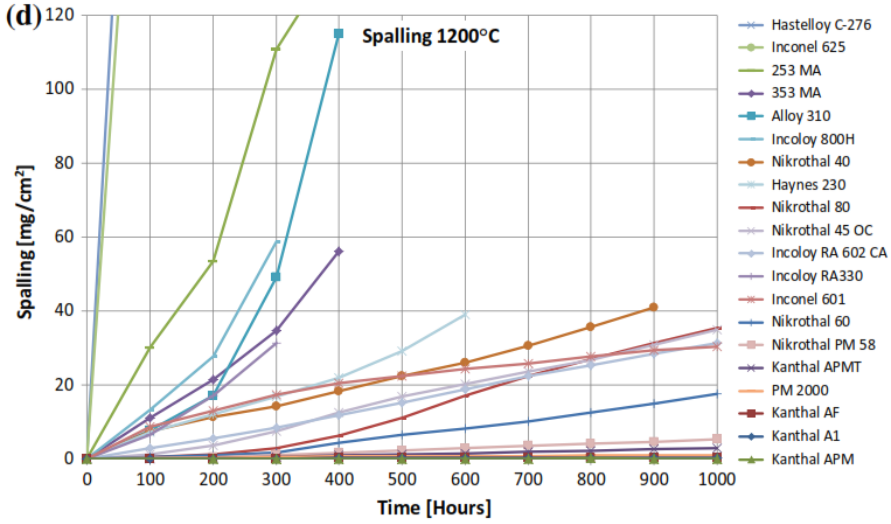

Figure 9. Spallation tracking of alumina and chromia formers (Jönsson et al.)[21]

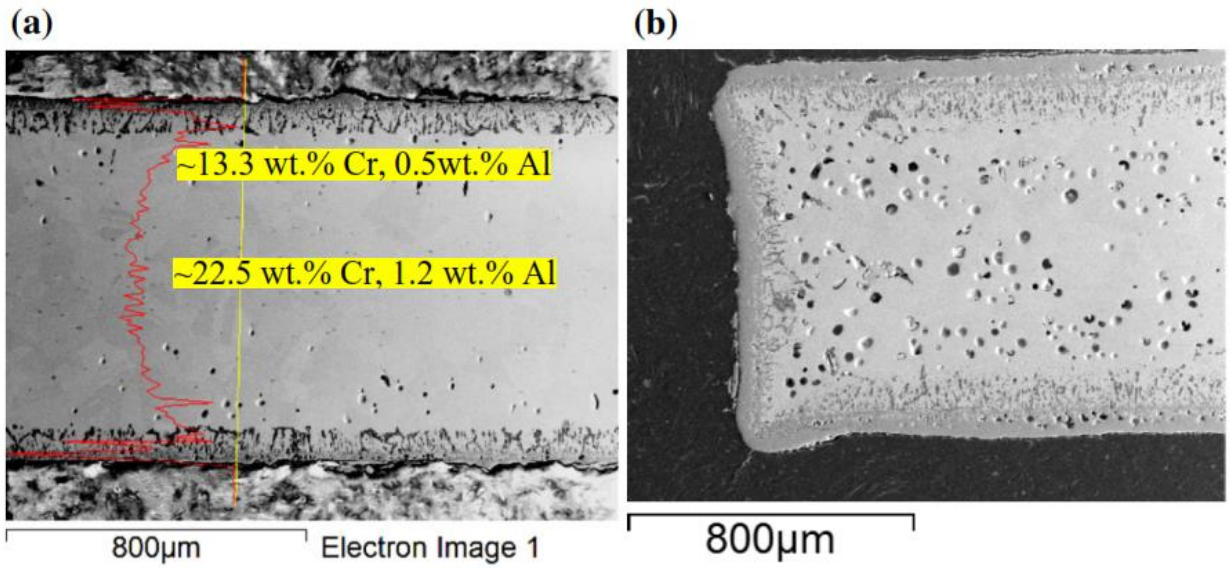

Figure 10. Pore formation in the chromia scale. a 1100°C with Cr line scan, b 1200°C (Jönsson et al.)[21]

2.12 Alumina in Petrochemical Industries

In comparison to CFA, alumina forming alloys (AFA) have better resistance to steam environments at high temperatures. A study by Muralidharan et al. looks at the cast alumina

forming steels for petrochemical industries and determined its applications for the petrochemical industries [22,23]. The alumina that is formed is thought of as a protective layer that is formed at the surface during the pre-oxidizing process as opposed to chromia. Although theory suggests this and to some extent experimental data also shows, there needs to be furthermore testing to prove the superiority of alumina. Due to the insulating properties of alumina, electrical properties are not usually explored. Mechanical and chemical properties are studied more.

Mechanical properties of AFA have been investigated. Research done by Yamamoto et al. has investigated high-temperature creep, tensile properties, and oxidation resistance properties of AFA [24]. Yamamoto et al. looked at three nickel-niobium based alloys with varying degrees of aluminum in the composition. They summarized the ultimate tensile strength, yield strength and elongation of the alloys before and after aging at 1023K at 500 or 2000 hours. After aging, the alloys showed higher strength with lower percentage of elongation. Additionally, they compared the alumina scale formation in dry air conditions and 10% water vapor conditions with varying niobium and aluminum content. With the water vapor conditions, the changes in niobium levels from the alloys had little effect on the alumina formation.

For alumina to be a viable use to the petrochemical industries, evidence is needed. The oxide layer needs to be uniform and present throughout the surface to function. Additionally, in alumina formers, alumina needs to form over the chromia. Initial work of producing a uniform layer of alumina in AFA has been done by the Oakridge National Laboratory research. Muralidharan et al. studied centrifugally casted AFA that are intended for the petrochemical industries [22,23]. The AFA was oxidized and characterized for the formation of alumina at the interface. Because the AFA here are centrifugally cast, the high interest area was the inner

diameter side. They compared the oxide performance with CFA with indication of the mass change differences as seen in figure 11.

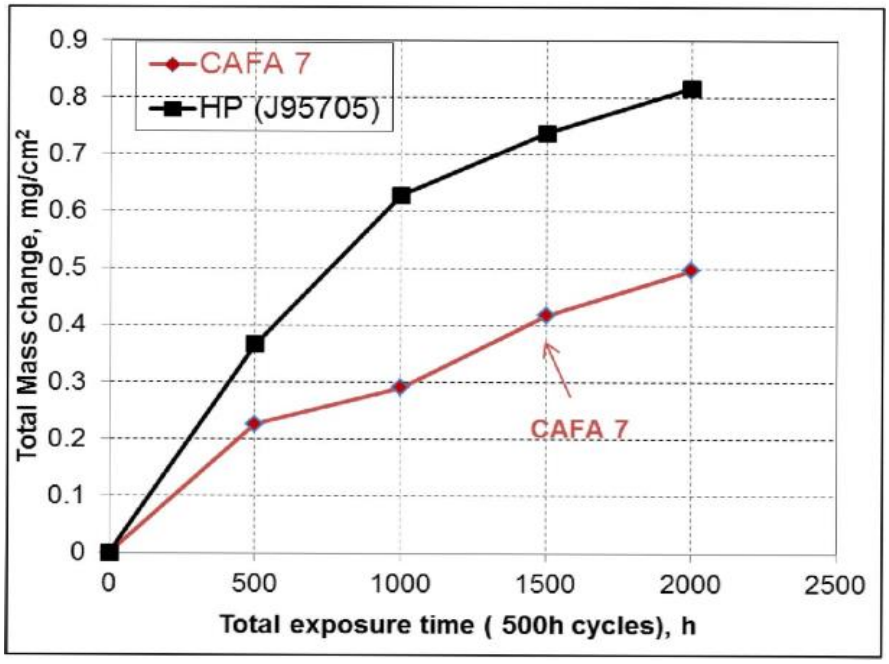

Figure 11. Mass change comparison of AFA and CFA for oxide performance (Muralidharan et al.) [22]

Muralidharan et al. also analyzed the oxide scale in the scanning electron microscope (SEM) for uniform formation and elemental analysis of oxide. Samples were coated with copper for edge retention and image results show a clear oxide scale over the surface of the AFA. Figure 12 depicts a SEM image showing the contrast difference of the alumina and the AFA base metal. Another study done by Elmer A. Prenzlow looked specifically at the steam oxidation of AFA as well [25]. These initial results allow for a standard for testing AFA alloys for petrochemical industry environments.

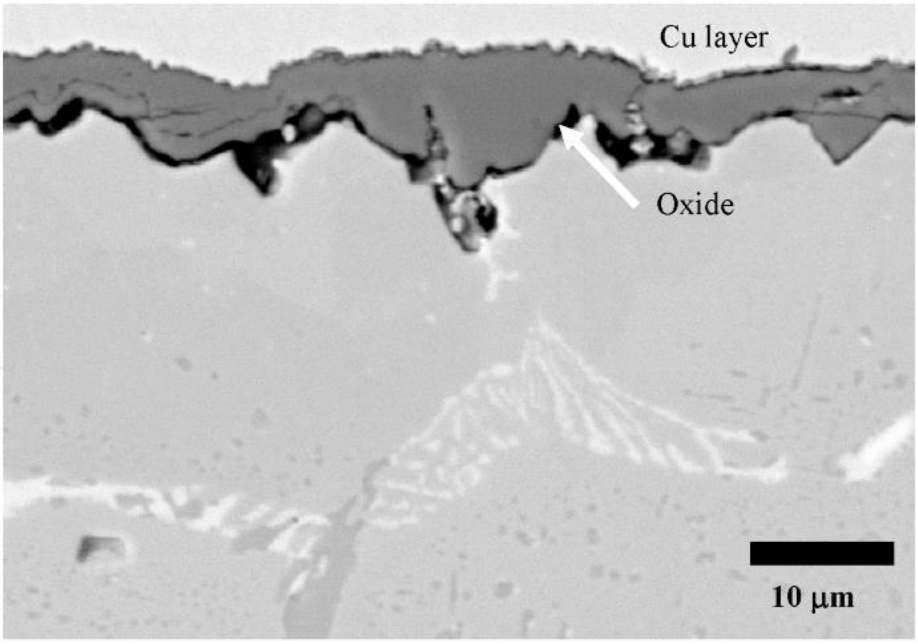

Figure 12. Alumina scale formation of an AFA (Muralidharan et al.) [22]

Although it is important to show alumina scale formation and relative performance comparison of AFA's and CFA's, more thorough understanding parameters such as parabolic rate constants, activation energies and different environmental conditions need to be performed.

Chapter 3

Activation Energy and Oxide Performance Study of Alumina Forming Steel

The goal of this chapter is to provide a baseline understanding on how oxidation works on the alumina forming and chromia forming alloys under pure steam environments. Four different alumina forming alloys were used with different aluminum content and one chromia former. The chromia former has a standard composition you will find in steal reactors that are used in petrochemical industries. Compared to chromia formers, alumina formers are chemically more resistant to steam and higher temperatures. This is critical as in the petrochemical industries; these two components are fundamentally at play. For the alloy to perform, it needs to be pre-oxidized. However, through cyclic cleaning with steam, this also introduces oxidation damage. This study compared a chromia former (HP alloy) and an alumina former (AFA). Oxidation tests were performed at 800°C, 850°C, and 900°C in pure steam environments for 100 hours each. Characterization of the two alloys used scanning electron microscopy (SEM) and x-ray diffraction (XRD). SEM was used to perform elemental analysis and imaging of oxide layers. XRD was used to determine and identify the presence of oxide. Additional data of mass changes will be presented to compare and obtain K_p values for kinetics study. Initial results show that alumina forming alloy had better performance in weight changes which allows for better resistance to oxidation damage.

3.1 Introduction

Steel reactors are made from a class of stainless steel labeled as High-Performance (HP) alloys. HP alloys are useful as they work well at high temperatures greater than 800 degrees. The petrochemical industries used centrifugally cast austenitic steel reactors that hold the cracking process of hydrocarbons. In this process, there is a pre-oxidizing step of the steel reactors followed by the cracking. Steel reactors are pre-oxidized through air and steam at temperature ranges of 900°C - 1200°C. The purpose of this process is to create an oxidation layer that serves

two functions. The first function is to create a relatively inert surface to prevent chemical reactions on the surface of the steel vessel and gas species. The second function is to provide a corrosion resistance layer to inhibit or slow the process of corrosion damage over time. Traditionally in the past, CFA has been used as the selected material for the steel reactors. Chromia is formed in the pre-oxidation treatment as the oxide layer.

CFA has been extensively studied with their performance in oxidation environments due to their oxidation resistance in relative high temperatures [3]. CFA's performance in such described environments during cracking has been proven effective in dry air conditions. However, in industry practice, pure air environments are not common and higher temperatures are used. With the introduction of steam and higher temperatures, this presents problems with CFA. Volatilization of chromia is observed in temperatures that exceed 1000°C [26]. The thermodynamic stability of chromia becomes less stable where growth of chromia is grown at a faster rate that is susceptible to volatilization. This led to an exploration of finding a different oxide scale that performs where chromia fails.

Aluminum in austenitic steels have benefits with respect to the petrochemical industries [22]. In comparison to CFA, alumina forming alloys (AFA) are thought to have better resistance to steam environments at high temperatures. The alumina that is formed is thought of as a protective layer that is formed at the surface during the pre-oxidizing process as opposed to chromia. Although previous studies have shown the mechanical properties aspect of alumina, the chemical and properties are still under investigation. For alumina to be a viable use to the petrochemical industries, evidence is needed. The oxide layer needs to be uniform and present throughout the surface to function.

3.2 Theory

Oxidization of metals has been extensively studied and well understood and stems into alumina as well [27]. Using alumina coating as a protective barrier has many applications and uses. Applications where high corrosion resistance is needed often use alumina to coat metals [28,29]. Corrosion studies on alumina thickness and performance have been looked at and shown to provide better corrosion resistance [30]. Thermodynamically, alumina has

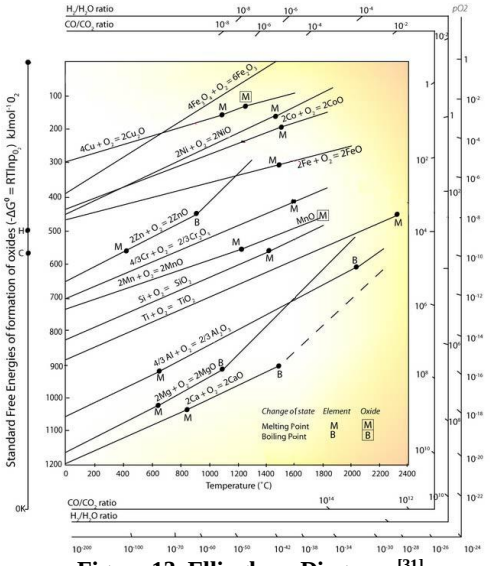

Figure 13. Ellingham Diagram [31]

been shown to be more stable than chromia and other metal oxides as seen in the Ellingham diagram in figure 13 [31]. In the diagram, the lower the oxide line, the more stable it is. In summary, alumina provides significant advantages in corrosion applications.

3.3 Methodology

Table 1 denotes each alloy's nominal composition. The first column is given by the alloy's heat number where 2535Z is the chromia former and G3607, G3610, MK11, and D11 are alumina formers. From this point on, the chromia former will be denoted as HP. Likewise, the alumina former G3607 will be denoted as AFA – 2.6%, G3610 as AFA – 3.9%, MK11 as AFA – 3.8%, and D11 as AFA – 4.7%. Prior to steam experiments, microstructural analysis and chemical characterization of the oxidized surface were observed. After steam experiments,

analysis for oxidation kinetics was also done and compared to literature values of activation energies. Data that is obtained in this section will be used for comparison and extension in subsequent sections.

Table 1. Nominal compositions of alloys used in oxidation experiments (wt. %).

Material	Al	Cr	Fe	Ni
HP	0	25	37	35
AFA - 2.6%	2.6	28	27	38
AFA - 3.9%	3.9	27	25	38
AFA - 3.8%	3.8	23	34	37
AFA - 4.7%	4.7	25	33	35

3.4 Microstructural Analysis

Microstructures of two alumina forming alloys were imaged with the optical microscope. This was done to gain insight on what microstructures are present beforehand in oxidation experiments. An etchant was used to etch the material before optical microscopy which was specific towards alumina forming austenitic steels. The setup is displayed in figure 14 where a process of electrolytic etching was performed.

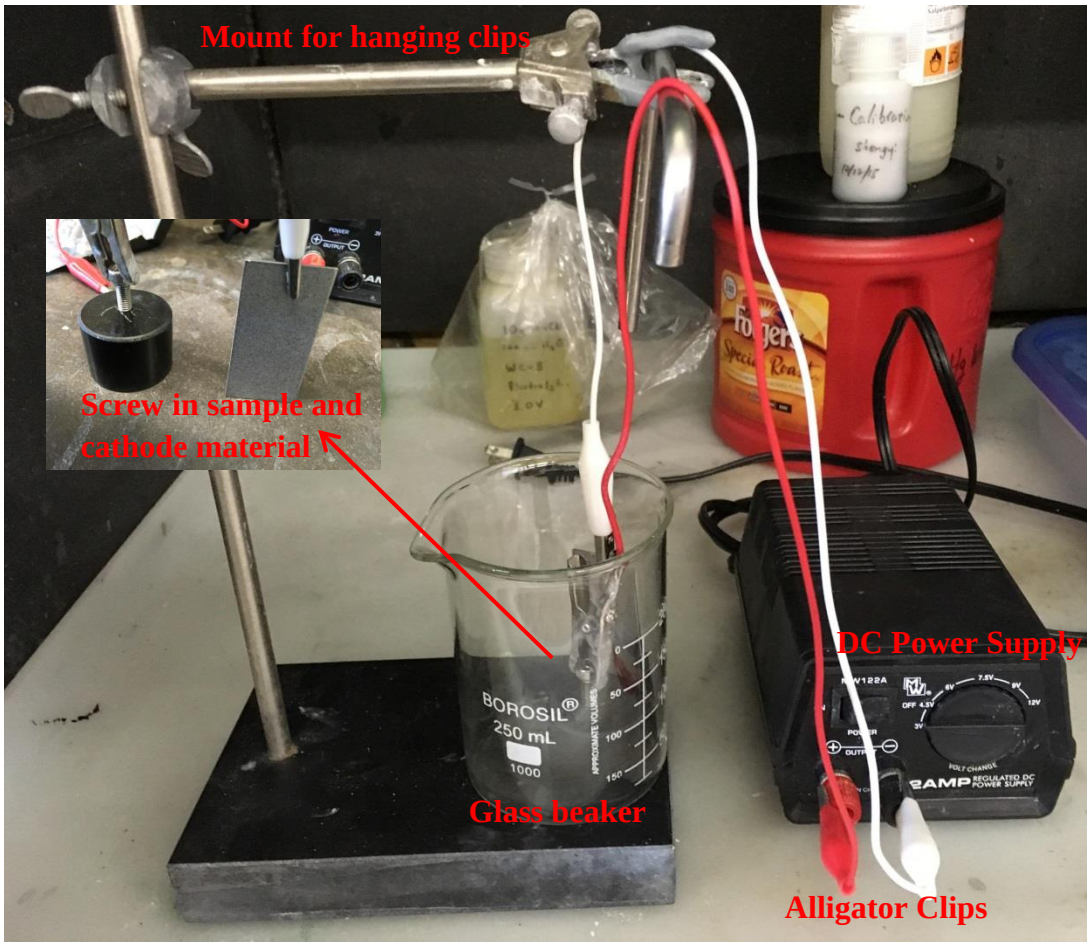

Figure 14. Etching setup for alumina formers.

The etchant solution was created with 10g of Sodium cyanide (NaCN) mixed into 100ml of distilled water. The selected voltage was at 3V and etched for five second intervals which optical microscopy check between intervals until microstructure is present. Etched samples were cleaned with reversed osmosis (RO) water.

A magnification of x50, x100, x200 and x500 was performed on each alumina forming alloy. Generally, each alloy that was etched and had microscopy performed, three possible phases were observed as seen in figure 15. There exists the dominant phase with a secondary phase containing dark markings. The dark markings are sometimes found to have a dendritic like structure and are present throughout the alloy. Lastly, the third possible observed phase was

identified to have small dark spots throughout the sample. Although similar in color to dark markings, the dark spots don't have long-stretched marks and are round in nature. It should be noted that figures 16 and 17 are not the AFA used in the steam experiments but are similar in composition and found to have similar microstructure.

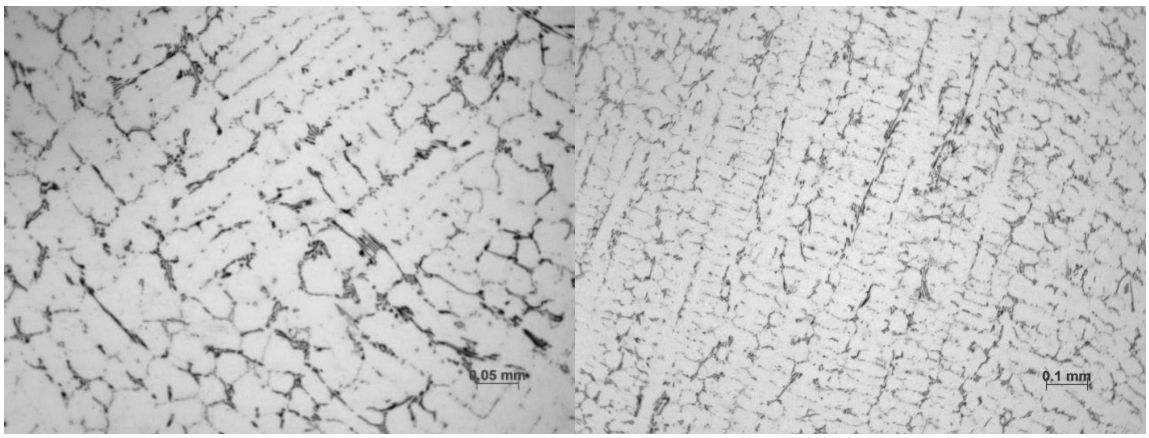

Figure 15. AFA – 2.6% microstructure, left) x100 magnification right) x50 magnification.

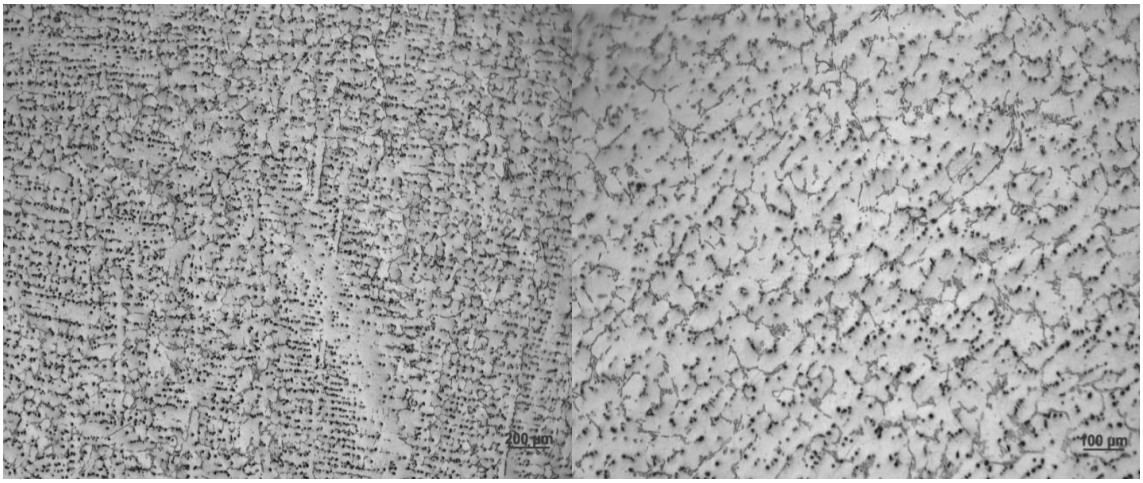

Figure 16. AFA microstructure left) x50 magnification right) x100 magnification.

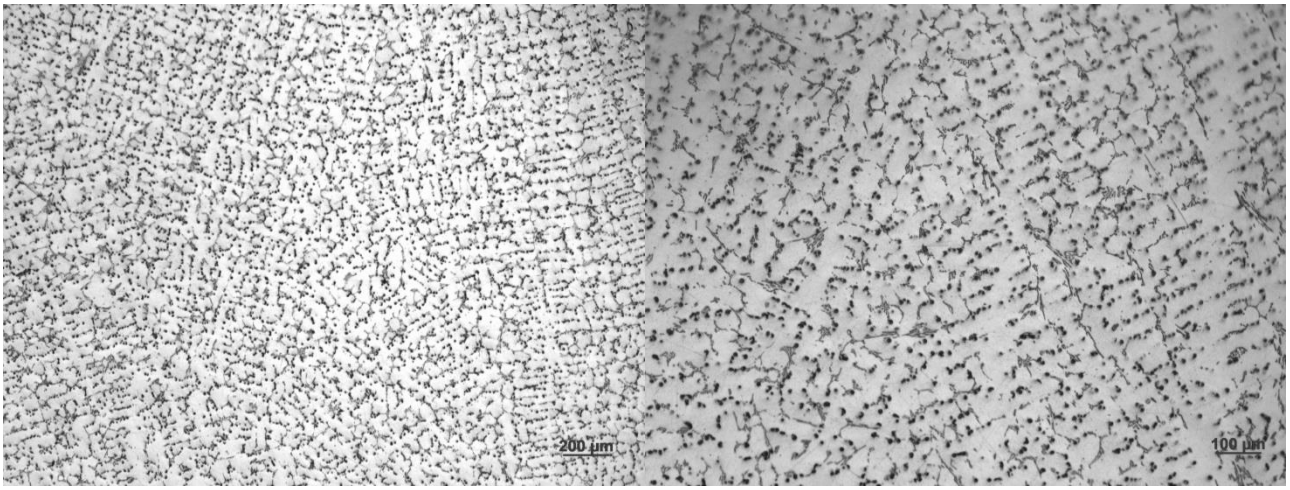

Figure 17. AFA microstructure left) x50 magnification right) x100 magnification.

3.5 Oxidation Experiments

Oxidation experiments were performed at various temperatures. The selected temperatures were 800, 850, 900 and 1000°C. The range of temperature tests allows for characterization of oxides at different temperatures and comparison of relative performance. This in turn also allows for the analysis of kinetics for reaction rate constants and activation energies. The standard for all oxidation experiments is to track the mass changes during oxidation. The oxidation experiments were performed for 100 hours with 10-hour intervals for mass change measurements. This allowed for ten data points for each tested sample.

Oxidation experiments were done with a tube furnace. The tube furnace contained an inlet with a custom-made water heater and an exhaust to expel steam. The water heater contained a helical water reservoir for boiling which was encased in heating coils and insulation. Water was transported to the reservoir via a peristaltic pump. The pump was set to push water at a rate of 0.5ml/min and a steam production rate of 480ml/min. From the water heater to the tube, a heating coil was placed with insulation so the steam transport would remain in vapor form. On the exhaust end, heating coils with insulation were also placed so that steam would continue to leave in vapor until it reaches the exhaust tip. Additionally, gas tubing was also mounted to the

inlet allowing the use of argon purging for cleaning out the tube furnace before oxidation. Figure 18 displays the tube furnace setup with the inlet and exhaust sides.

Figure 18. Complete steam furnace setup

Before every oxidation experiment, the furnaces are purged thoroughly with argon and the entire furnace setup is brought to temperature to remove water. In addition, the water supply to the pump is also aerated with argon to remove impurities of gases. The tube furnace contains three controllers in which it can be programed to control heating rates and holding times. Heating rates were always kept to 10°C/min and holding times were kept to 10 hours. As the experiments were done for 100 hours, this was repeated 10 times.

Sample preparation was required before oxidation experiments. Samples were cut to dimensions, grinded to 600+ grit, marked and weighed. Samples were centrifugally cast and as such when prepared, are trapezoidal in shape. Because of varying dimensions and weights of each sample, when portraying data for mass change, samples were given as a ratio of mass change per surface

area. Surface area was calculated out from formula 15 below where x, y, h and t t is represented by figure 19. The average surface areas of each sample were taken and tabulated below in table 2.

Equation 15

$$\boldsymbol{Surface\ Area = t\left[\left(x + y + 2\sqrt{h^2 + \frac{1}{4}(y - x)^2}\right) + (x + y)\right]}$$

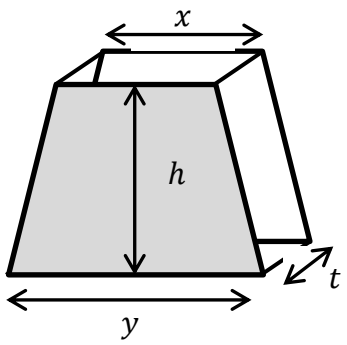

Figure 19. Surface area setup for trapezoidal shape

Table 2. Average surface areas of alloys tested in various temperatures.

	Average Alloy Surface Area (mm^2)				
Temperature	**HP**	**AFA – 2.6%**	**AFA – 3.9%**	**AFA – 3.8%**	**AFA – 4.7%**
800°C	**402.5**	**452.9**	**466.2**	**419.2**	**480.8**
850°C	**300.2**	**542.2**	**386.7**	**247.4**	**378.9**
900°C	**268.3**	**291.0**	**363.0**	**293.7**	**516.2**

3.6 Mass Change Measurements

Mass change measurements were performed to track the oxide growth of the alloy samples and to be used for obtaining kinetic information. Mass changes were measured with a microbalance with accuracy to five decimal places. This accuracy allows for small detections of the oxide growth within the samples. Using equation 8, we can solve for Δm^2 by taking the

square root of both sides of the formula. This allows us to plot our data points of change in mass versus the square root of time. Figures 20, 21, and 22 represent the average mass change measurements with respect to the square root of time in seconds for each temperature experiment.

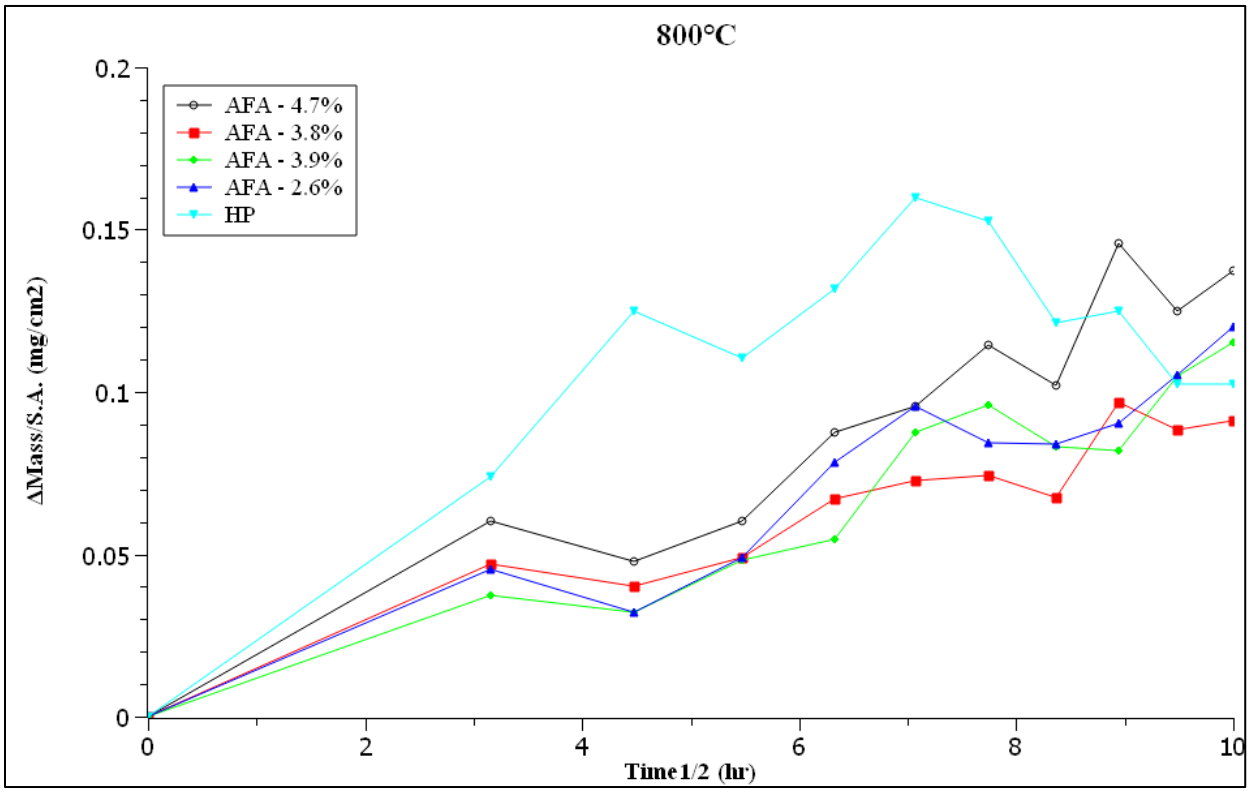

Figure 20. Average mass change measurements of the alloys at 800°C.

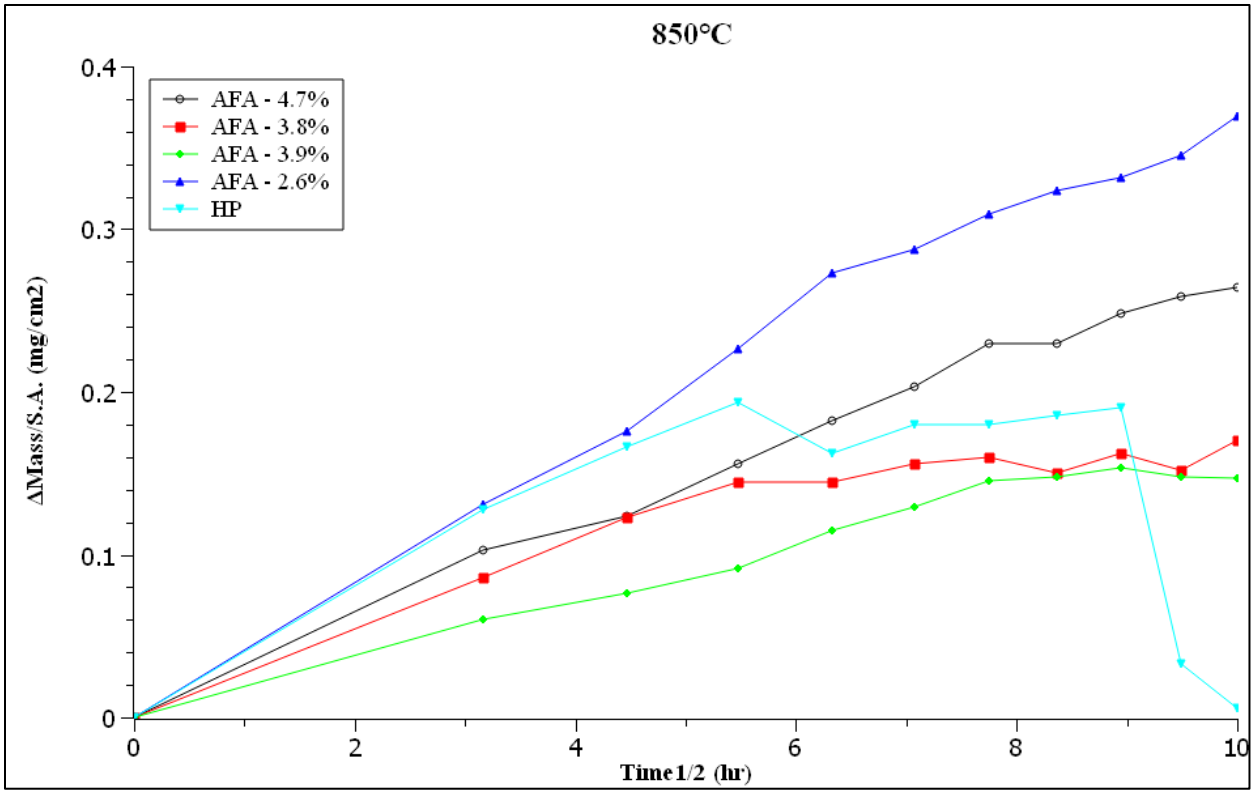

Figure 21. Average mass change measurements of the alloys at 850°C.

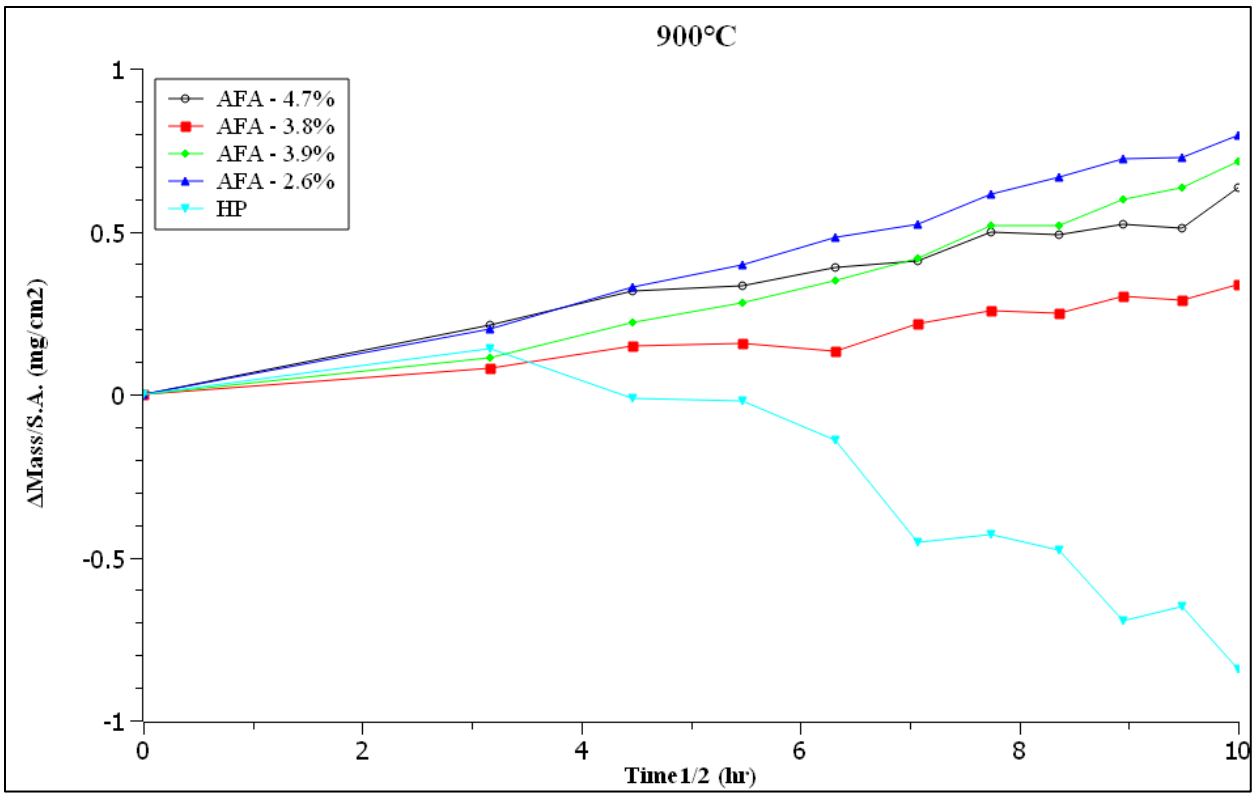

Figure 22. Average mass change measurements of the alloys at 900°C.

3.7 Parabolic Rate Constant of AFA – 2.6% and Other Alloys

Tracking of the change in mass in the steam experiments, it is possible to determine the type of rate law for each alloy and temperature. The rate law can be found in the given equation below.

Equation 16

$$\frac{\Delta m}{SA} = kt^n$$

Where Δm is the change in mass, SA is the surface area of the sample, k is the temperature dependent rate constant, and n is the time exponent of the rate law. By applying the function "log", the equation can be linearized to equation 17 below.

Equation 17

$$\log\left(\frac{\Delta m}{SA}\right) = \log(k) + \mathrm{nlog(t)}$$

This is crucial because graphically, n or the time exponent of the rate law can be determined as the slope of the linearized line. As mentioned in chapter 2.8, the value of the slope determines the type of the rate kinetics. With values that are close to 0.5, it can be considered a parabolic rate law. This is integral in the next steps as parabolic rate kinetics allows the derivation of activation energy of formation of the oxides. Figure 23 depicts the plotting of the alloys with respect to the log function.

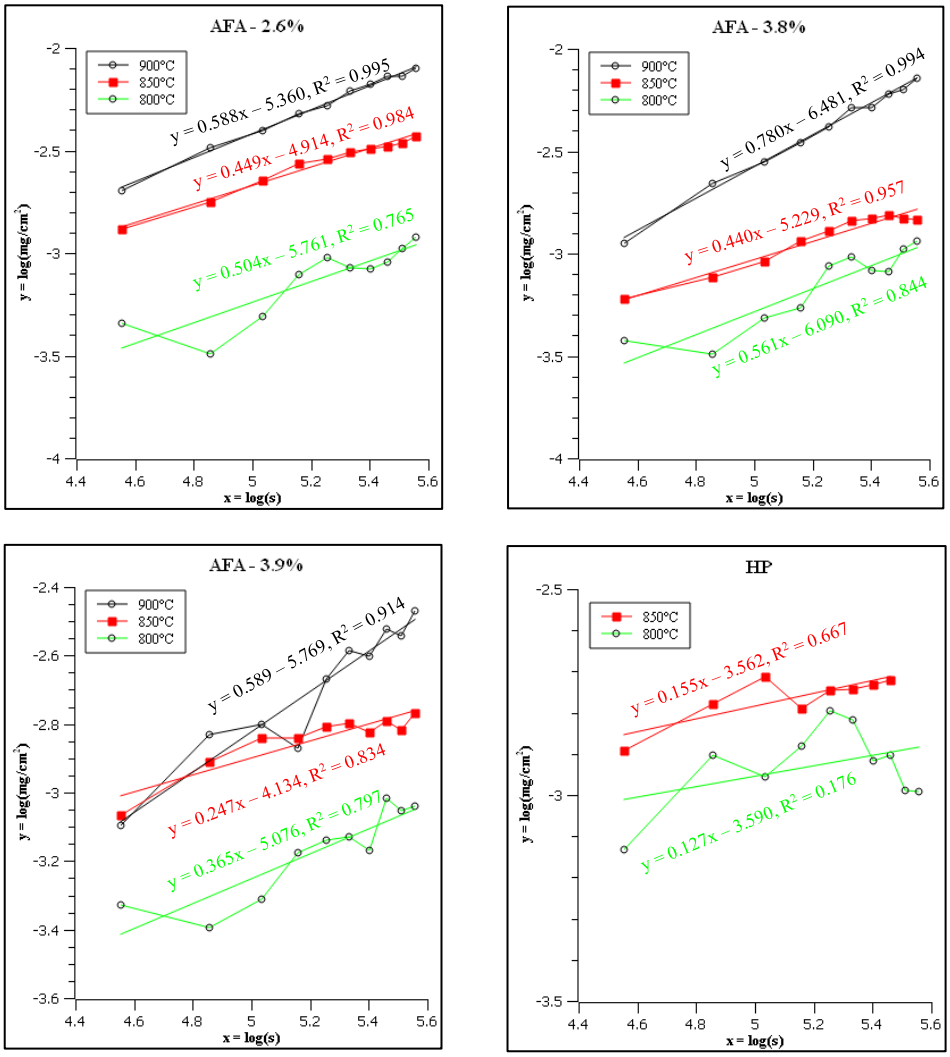

Figure 23. Regression data for the steam oxidized alloys under three different temperatures oxidized at 100 hours.

Once the plots were given, regression with linear trend setting was performed and an equation of the line was given. The significance of this process is to determine if the data follows a parabolic nature and follows typical oxidation kinetic behavior. If the data shows a different rate law, it will require a different analysis. In general, the experiments ran were parabolic in nature with exceptions to the HP and some of the AFA. HP at 900°C had significant mass loss

and as such did not display parabolic nature in mass change. AFA – 3.9% at 850°C and HP at 800°C and 850°C also had some irregular behavior with its data set. The n value deviates from the 0.5 value for parabolic nature and should be noted that this still allows the analysis and calculation of activation. It should also be noted that AFA – 4.7% was no longer used from there point on. Due to the limited resources of available samples, AFA – 4.7% was no longer viable. Additionally, the performance in terms of mass change for that sample set did not perform well compared to the other AFA's. Lastly, mass change data at 1000°C was not used for determination of activation energy. Data at 1000°C had the same issues as 900°C but more severe and as such removed from the calculation.

3.8 Activation Energy of AFA

The parabolic rate constants of the alloys at 800°C, 850°C and 900°C was used and plotted to determine the activation energy of the oxide formation. Using formula 8 we can substitute in formula 14 into k_p which gives the form of the formula below in equation 18. It is important to note that the version of k_p value used is kept in the squared root version. To obtain k_p graphically, equation 16 was used to apply to the data sets for mass change. Mass change was converted to the squared version and plotted again time in seconds. These plots are given in figure 24.

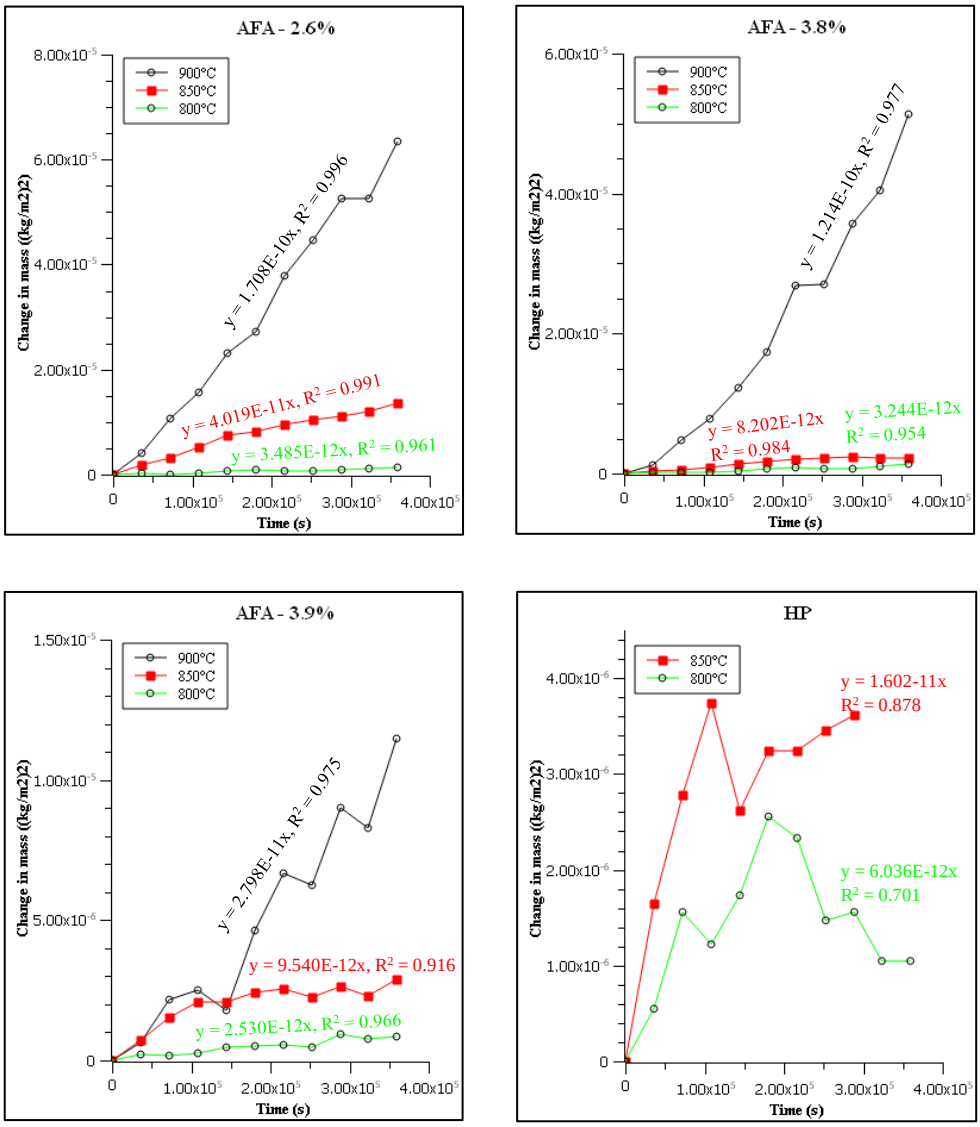

Figure 24. Mass change per area in squared version for each temperature on the AFA and HP alloys. Linear trend setting was performed to obtain equation of the line.

In the linear trend setting, the slope of the line is the $k_p$value. k_p values were obtained for each mass change data set for HP and AFA alloy at 800°C, 850°C, and 900°C. In table 3, the n and k_p values were tabulated based on the temperature and sample.

Table 3. Rate constant (k_p) and time exponent of rate law (n) for HP and AFA alloys at 800°C, 850°C, and 900°C.

Alloy	800°C		850°C		900°C	
	n	k_p	n	k_p	n	k_p
HP	0.13	6.04E-12	0.16	1.60E-11	CND	CND
AFA - 2.6%	0.50	3.49E-12	0.45	4.02E-11	0.59	1.71E-10
AFA - 3.8%	0.56	3.24E-12	0.44	8.20E-12	0.78	1.21E-10
AFA - 3.9 %	0.37	2.53E-12	0.25	9.54E-12	0.59	2.80E-11

Equation 18

$$\Delta \boldsymbol{m^2 = k_0 \exp\left(-\frac{Q}{RT}\right) t + c_p}$$

To continue the calculation for activation energy, formula 8 can be substituted in for k_p and is given by formula 19.

Equation 19

$$\boldsymbol{k_p = k_0 \exp\left(-\frac{Q}{RT}\right)}$$

Solving for activation energy Q, it is given by formula 20.

Equation 20

$$\boldsymbol{Q = \ln(k_p)\, RT}$$

The significance of equation 20 is that it allows for the ability to solve for activation energy graphically. Equation 20 can be broken down by the relationship where $\ln(k_p)$ is plotted versus the inverse of temperature. When plotted, the equation of the linear trend setting line is given as $\frac{-Q}{R}$.

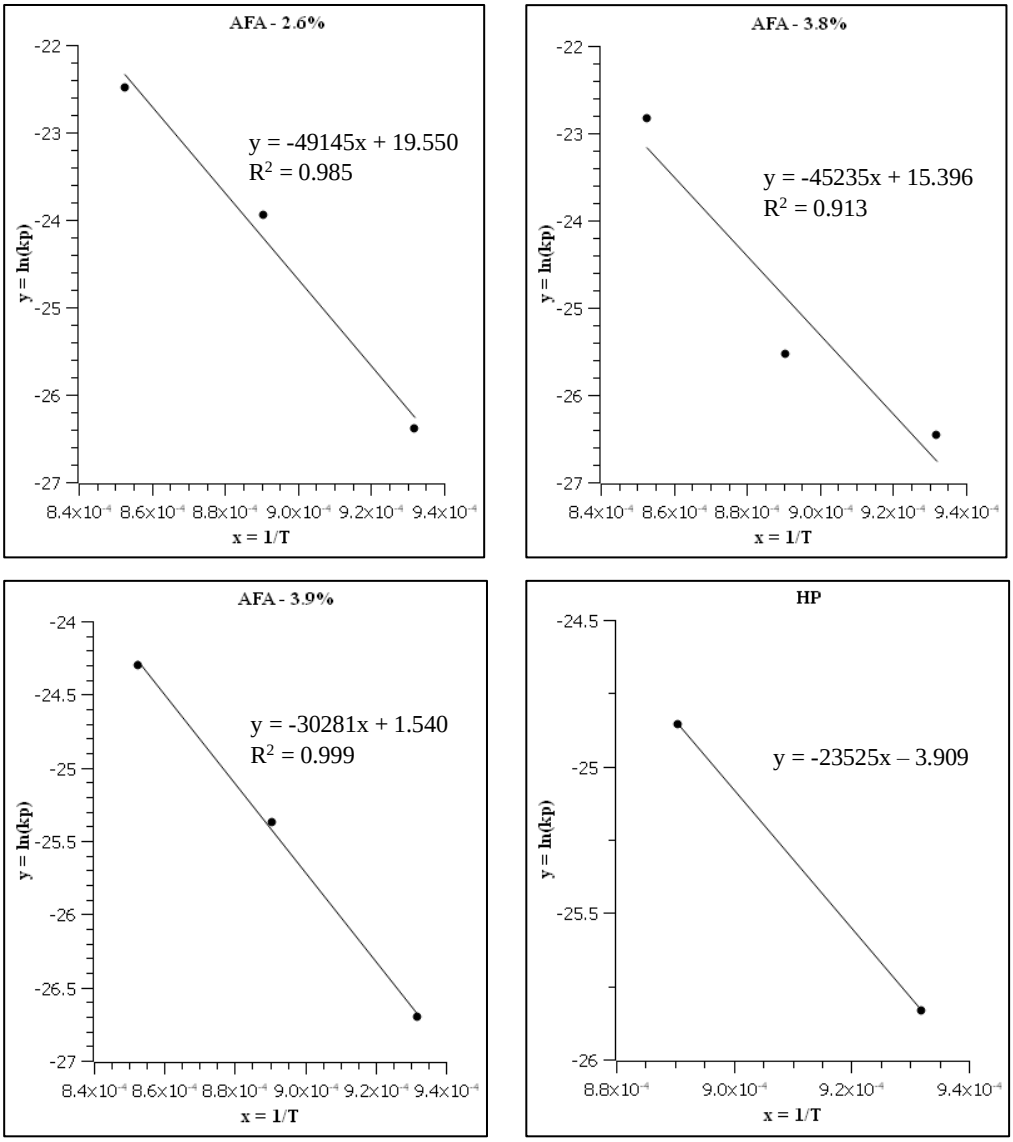

Figure 25. Arrhenius plots for AFA and HP alloys for activation energy calculations.

The Arrhenius plots for each AFA and HP alloy were performed in figure 25 with linear trend setting for the equation of the line. With the slopes given, activation energy was calculated out for each alloy. The activation energies were tabulated in table 4 below.

Table 4. Calculated Activation Energy of HP and AFA alloys

Alloy	Activation Energy (kJ/mol)
HP	195.6
AFA - 2.6%	408.6
AFA 3.8 %	376.1
AFA 3.9 %	251.8
AFA Average	345.5

It is important to note that with the HP alloy, there were only two data points in the calculation of the activation energy. This is due in part that the 900°C data set for HP was not viable for analysis with its continual mass loss. Further analysis and application of a different rate law would potentially give a more accurate calculation of the HP activation energy. With that said, the value obtained was 195.6 kJ/mol. This value is within the normal range of what chromia was found to form at. The study on chromia formation in pure chromium by Gulbransen et al. was analyzed [3]. With the same kinetic analysis procedure used for the HP and AFA alloys, the chromia formed in the study was found to have an activation energy of 222 kJ/mol. An analysis of various studies on chromia and iron oxide was summarized and reported in table 5 below for other studies.

Table 5. Summary of Activation Energies (calculated) for FeO and Chromia

Author(s)	Year	Oxide	Alloy/Metal	Gas	Activation Energy (kJ/mol)
C. T. Fujii et al. [14]	1964	FeO	Fe-Cr	Ar-H2O	92
X. Chen et al. [12]	2005	Cr2O3	430 SS	air	83.9
D. Caplan et al. [32]	1975	Cr2O3	Cr	O2 (1 atm)	243
E. A. Gulbransen et al. [3]	1957	Cr2O3	Cr	O2 (0.1 atm)	222
P. Kofstad et al. [4]	1980	Cr2O3	Cr	O2 (9.9 atm – 9.9e-7 atm)	315
A Talekar et al. [9]	2008	"First oxidation Regime"	HSLA Mn24 and SS46	O2	82.3 and 101.6

As calculated from various experimental data, chromia has a range in which it forms chromia. The average activation energy for the AFA alloys was found to be 345.5 kJ/mol. Alumina overall had higher activation energies than HP and from literature summarized.

3.9 Oxide Scale Thickness Prediction

Initial analysis on the attempt to model the oxidation growth was performed. Using assumptions and data from mass change measurements, oxide thickness profiles were obtained. The assumption taken was that the mass changes gained were a result of alumina. This meant that the formation of intermetallic and other oxides was disregarded. The density of alumina was also taken at the accepted value of 3.95 kg/mm^3. Relating the reaction rate constant to the density, a thickness factor can be calculated out. Using mathematical manipulation, we can take the thickness factor and remove the time component by multiplying it by each other giving thickness at that specific time. This allows the modeling of oxide scale thickness as a function of time. This early model prediction of oxide scale growth was performed on all alloys tested. The thickness versus time was plotted out and displayed in figures 26, 27, 28 and 29.

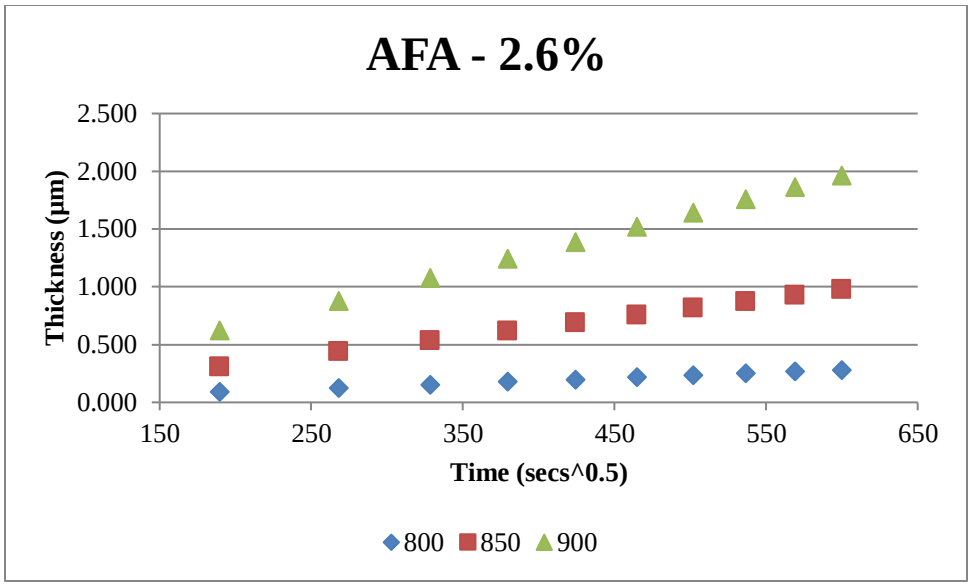

Figure 26. Oxide scale growth of alloy AFA - 2.6%

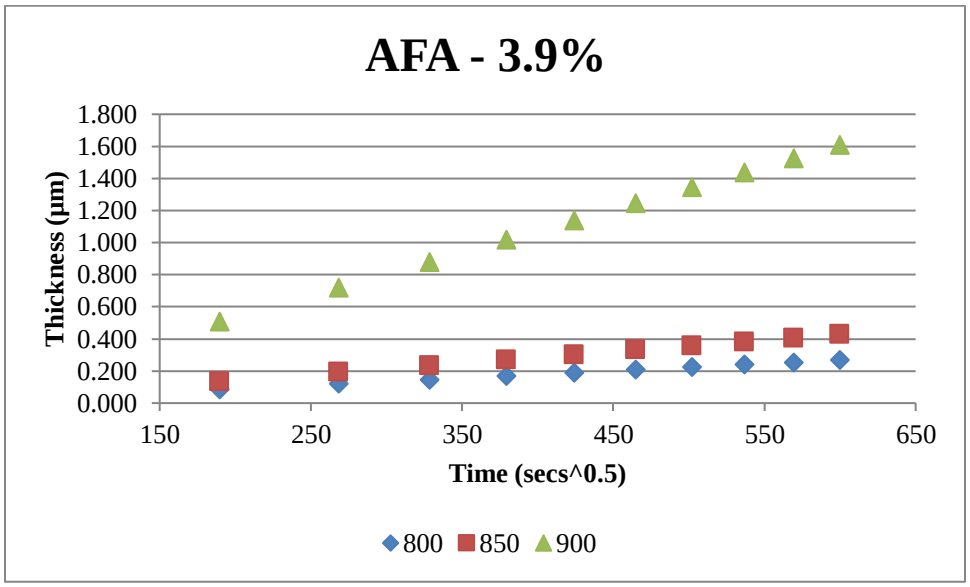

Figure 27. Oxide scale growth of alloy AFA – 3.9%

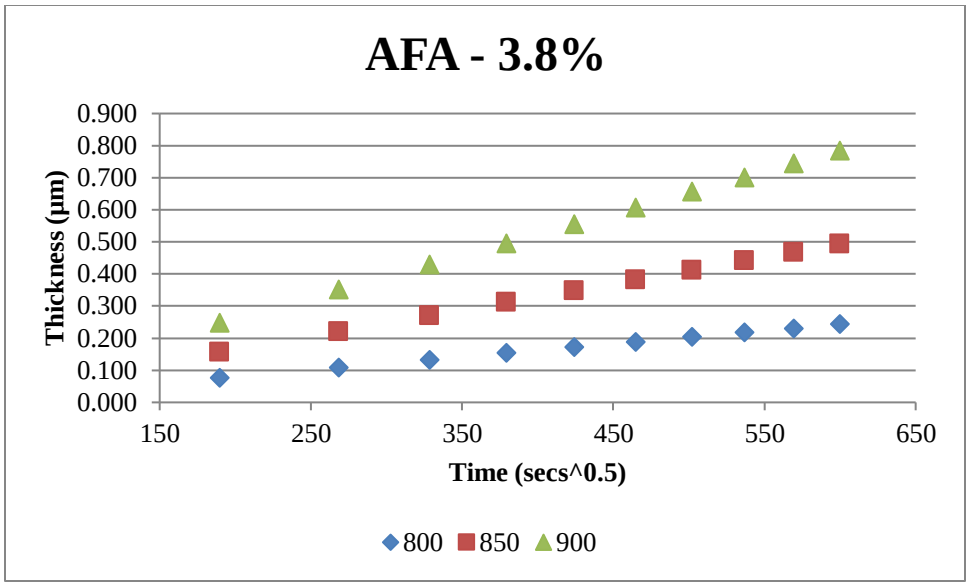

Figure 28. Oxide scale growth of alloy AFA – 3.8%

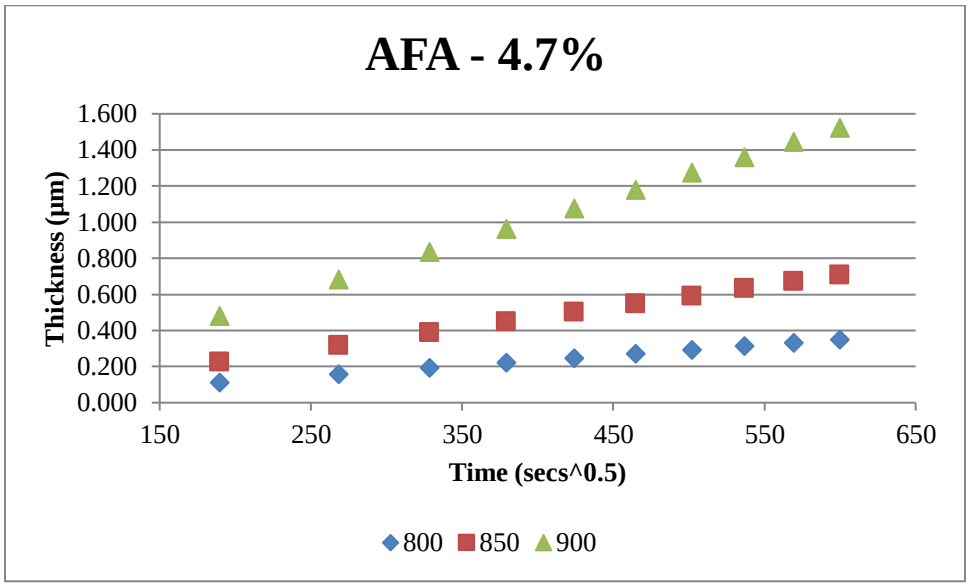

Figure 29. Oxide scale growth of alloy AFA – 4.7%

3.10 SEM Analysis of Oxide Scale

To determine the oxide scale and type of oxide of the tested samples, SEM was used. SEM is useful for imaging of the oxide scale for uniformity and internal damage. SEM was performed on the JEOL JSM-6460 LV with Energy Dispersive Spectroscopy (EDS). In the SEM analysis, the cross-sectional area in the inner diameter side was characterized. AFA alloys

performed similarly and as such AFA – 2.6% was used in comparison to HP. SEM parameters used for imaging and EDS was set to 12mm working distance with 15kV accelerating voltage with a tungsten filament. In figure 30, the comparisons of the 100-hour oxidized sample were done. Although HP did form a thicker oxide, the uniformity of the oxide form was not as good as the AFA – 2.6%. Additionally, the performance of the HP oxide at higher temperature was outperformed by the AFA – 2.6%.

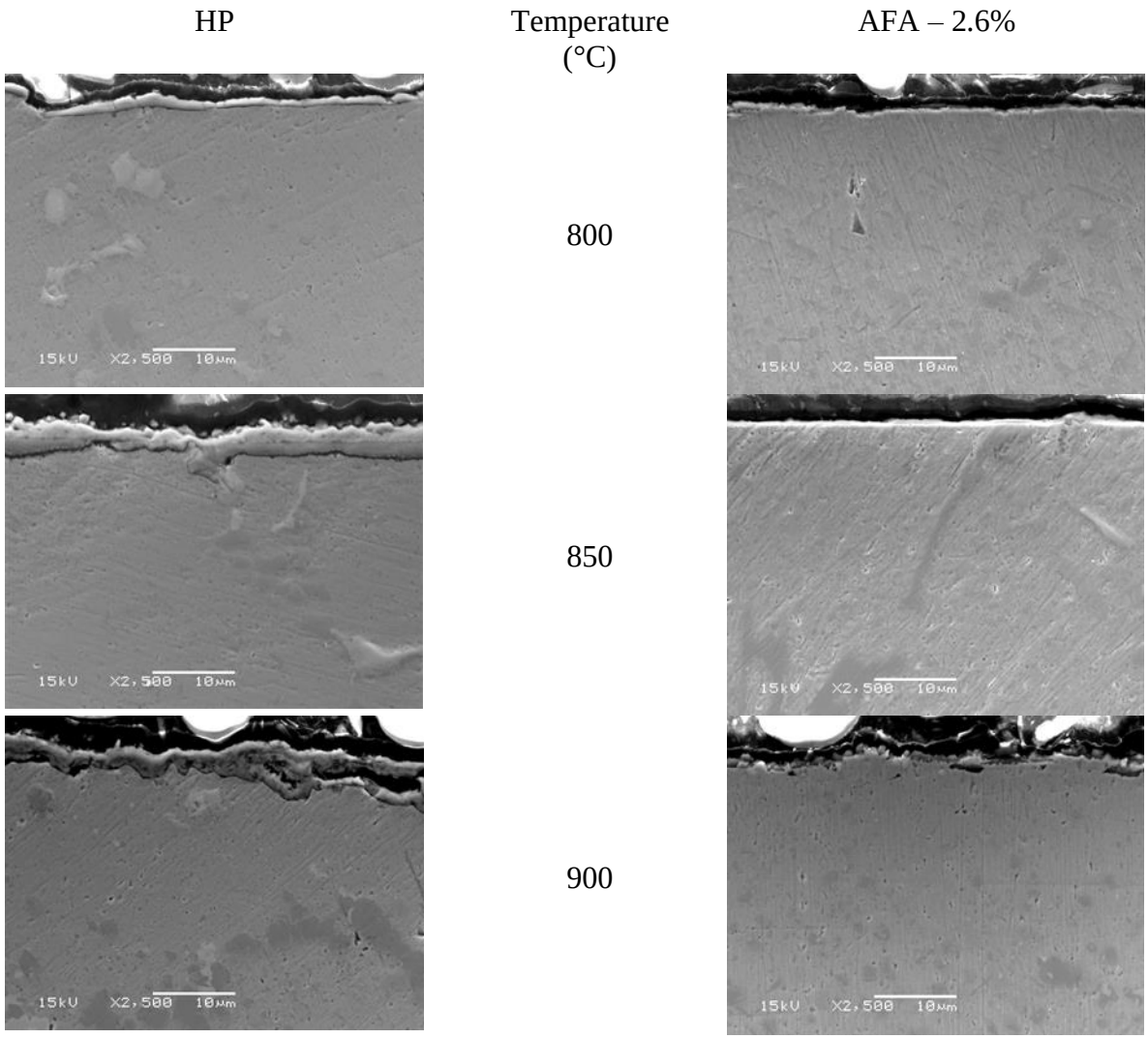

Figure 30. SEM image comparison of HP and AFA – 2.6%

Line scans of the HP and AFA – 2.6% were also performed. The line scans show the list of detected elements as it was scanned across the oxide scale into the base metal. The selected line scan was performed on an area that was an average representative of the general cross-sectional area of the alloy. Figure 31 compares the HP alloy to the AFA – 2.6% alloy. The black marker depicts the line scan at start of the oxide where the left side is the mount material, and the right begins the alloy line scan. HP depicted matching scans of chromium and oxygen leading to the identification of the chromia formed at the surface whereas the AFA – 2.6% depicts the matching scans of aluminum and oxygen leading to the identification of alumina. Line scan parameters were scanned for 300 seconds per line scan.

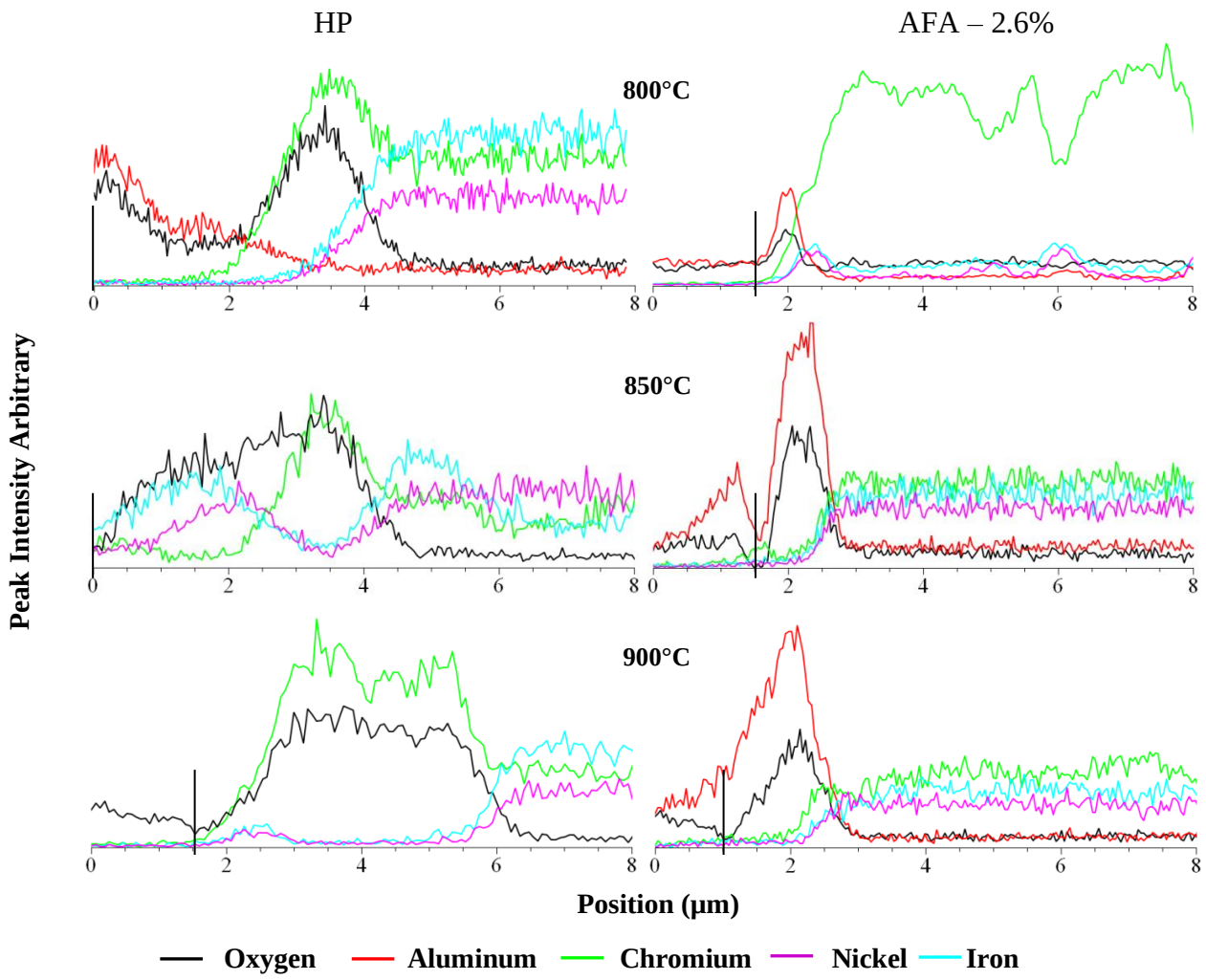

Figure 31. SEM line scan comparisons of HP and AFA - 2.6%

3.11 XRD Analysis on the Oxide Scale

To complement the SEM analysis and characterization of the HP and AFA – 2.6%, XRD was performed for identification of present phases and oxide of the samples. XRD analysis was performed on the Bruker D8 Discover with scanning parameters 10°-120° with rotations of 0.5° per minute. The selected step size for the scan was set to 0.020° with a total scan time of one hour. The spectrums obtained from XRD were then matched to the library database PDF files.

Figure 32 shows the spectra of the CFA alloy at the three tested temperatures. The spectra for CFA alloy were relatively simple as it shows mainly the Fe-Ni matrix and the oxide scale. This is in part due to the thicker oxide scale formed, the surface penetration depth of the XRD only allowed for the identification of the two phases. In figure 33, the spectrum shows the scans of the AFA -2.6% alloy at the three tested temperatures too. Due to the thinner oxide scale of the alumina, the penetration depth of the XRD exceeds the thickness, thus picking up additional phases found in the alloy.

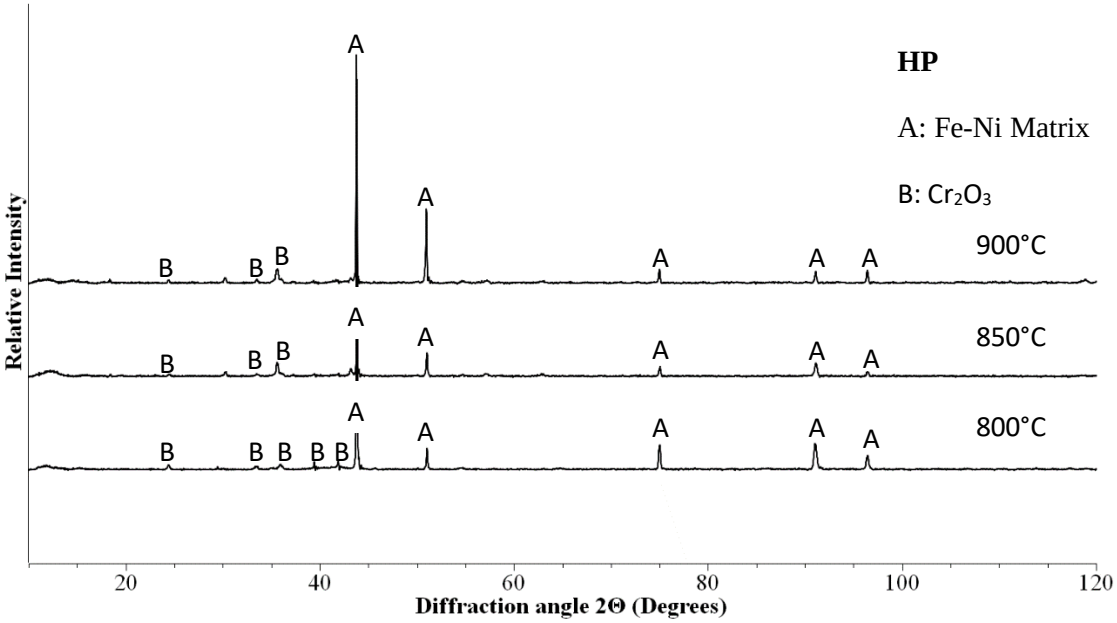

Figure 32. Spectrum of HP at the tested temperatures

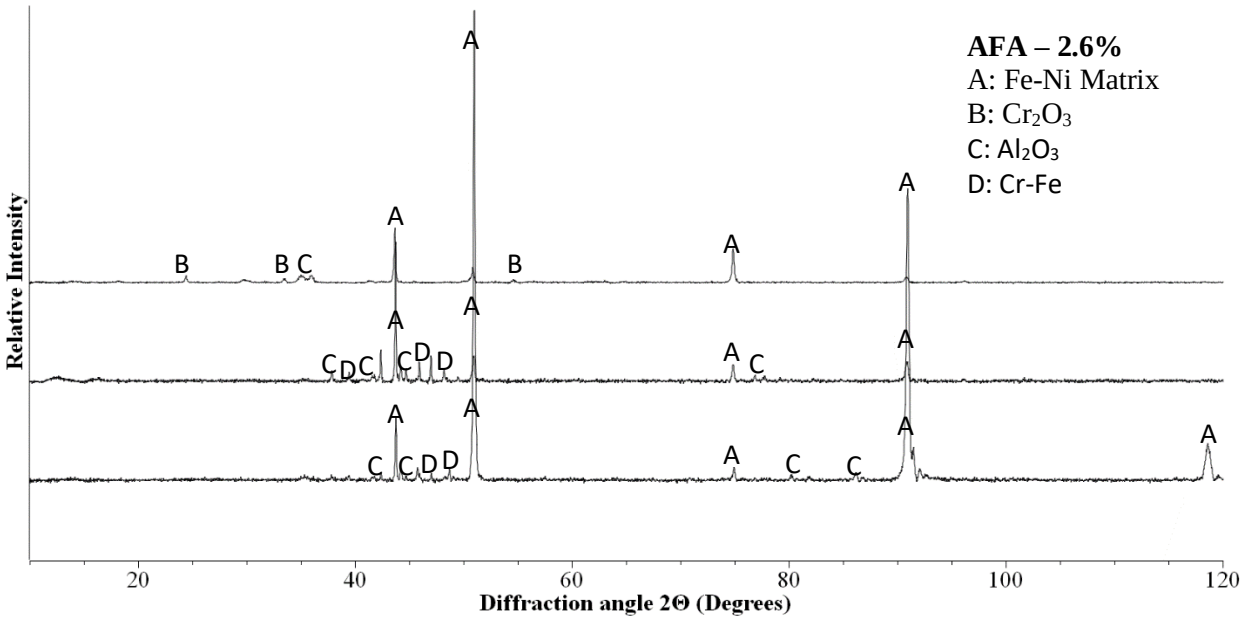

Figure 33. Spectrum of AFA – 2.6% at the tested temperatures

In addition to the standard characterization of the alloys in XRD, glancing incidence was also performed. Due to the low detection of the oxide scales, glancing incidence technique was used to assure the determination of the oxide is true. Glancing incidence determines if texturing or preferred orientation is a factor in the scan. At lower angle scans, the ratio of the main Fe-Ni peak to the alumina peak decreases. The selected glancing incidence angles were 5°, 7.5° and 10°. This can be seen in figure 34. A rocking curve was also obtained to determine if preferred orientation was detected. As seen in figure 35, the scan is relatively flat which leads to the alloy having a non-preferred orientation giving a strong indication it is a result of oxide scale and not a result of crystal orientation from the matrix metal.

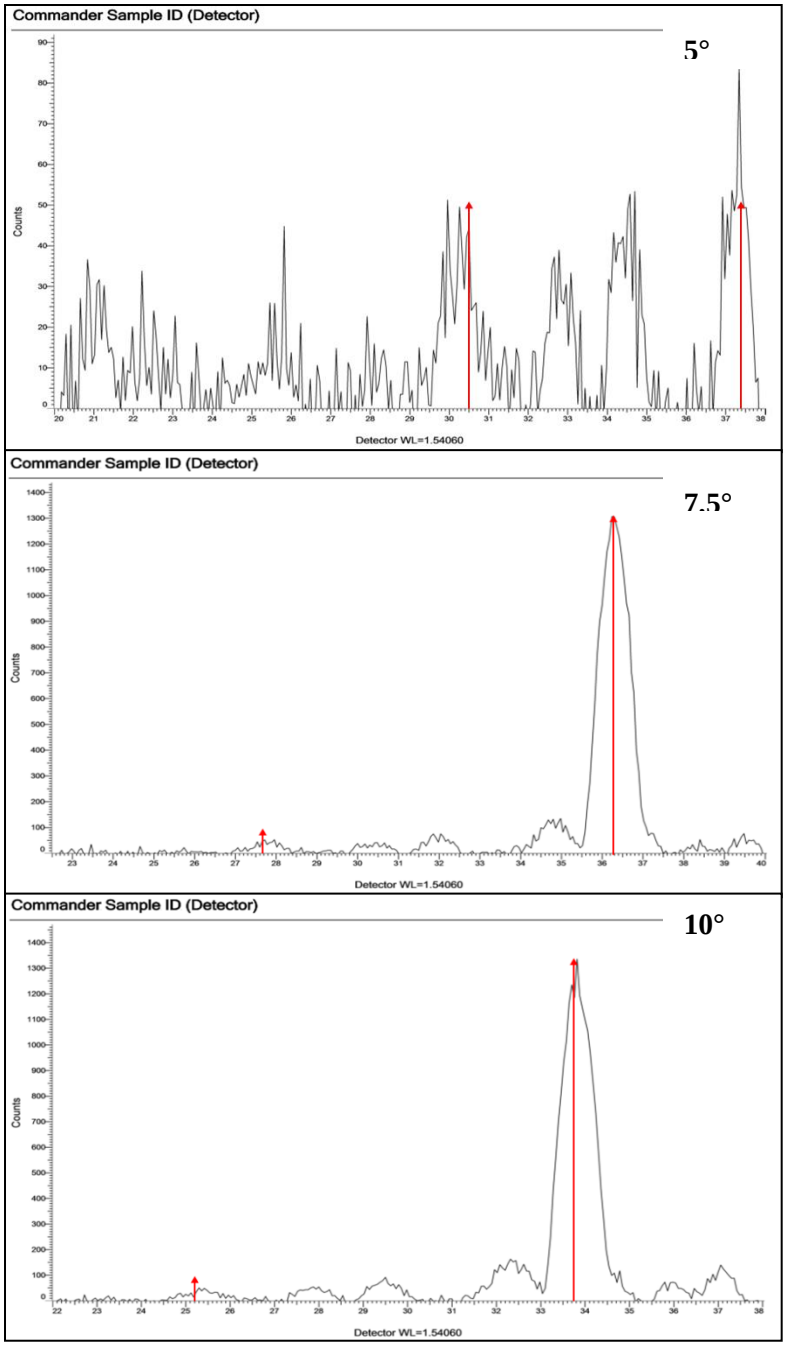

Figure 34. Glancing incidence angles scan of AFA – 2.6%

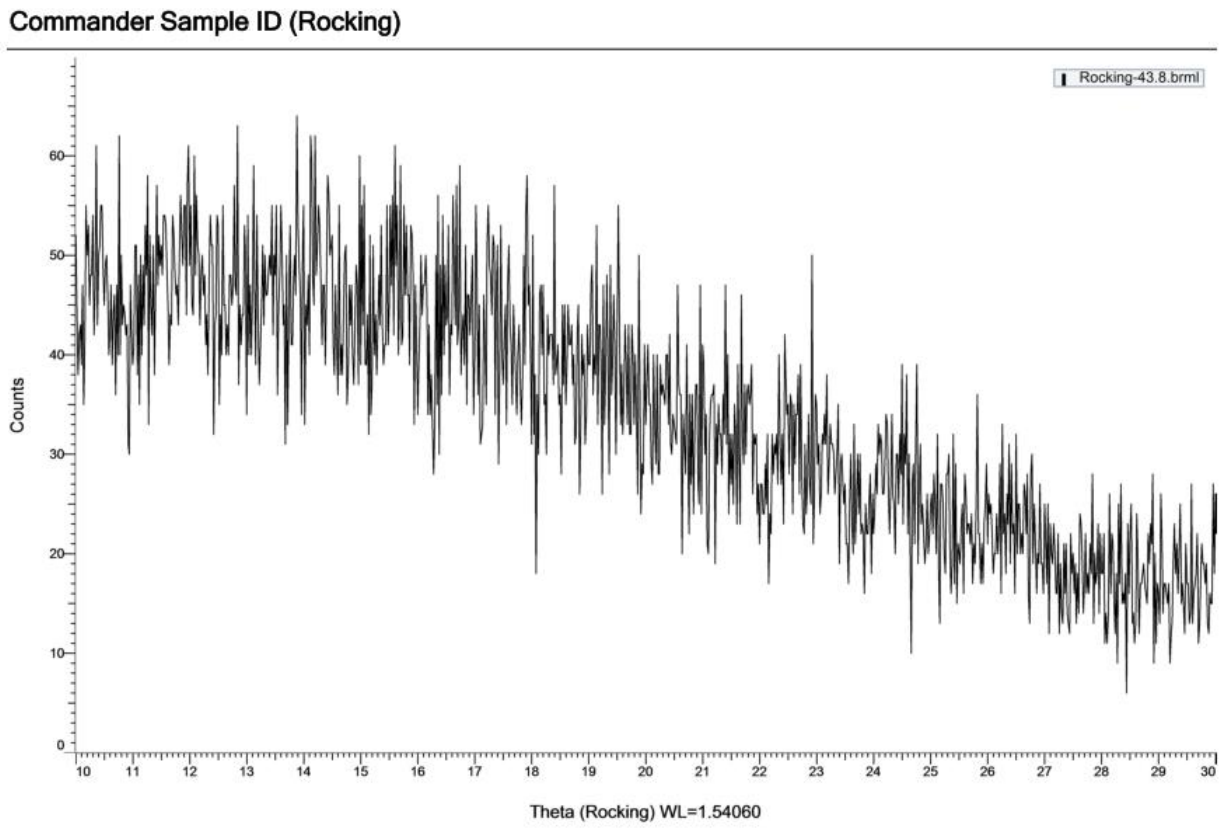

Figure 35. Rocking curve of AFA – 2.6% at the oxide peak

3.12 Summary

Oxidation experiments were performed on alloy HP, AFA – 2.6%, AFA – 3.8%, AFA – 3.9%, and AFA – 4.7% at 800°C, 850°C and 900°C for 100 hours each. HP showed to not exhibit a parabolic relationship and experienced loss mass at 900°C, therefore kinetics study only used at two data points. The AFA alloy series showed a parabolic relationship with mass changes and thus a kinetic study was possible. Average mass measurements were tracked and reported for both HP and AFA sets.

SEM-EDS characterization of HP alloy and AFA – 2.6% showed that both generated oxides during the oxidation experiment. HP showed the standard chromia and a general increase in oxide thickness at higher temperatures. AFA – 2.6% did also had formation of alumina and grew thicker as the temperature increased. It can also be generalized that the oxide layer was in

better shape at lower temperatures compared to the higher temperatures. XRD complimented the SEM-EDS data well with corresponding oxide peaks.

A Kinetics study of AFA was performed and had an average index rate law of 0.51 which indicates parabolic rate law kinetics. Parabolic rate constants were obtained from the square root time vs average mass change graphs. Parabolic rate constants of each temperature were then plotted to obtain activation energy. Average activation energy of alumina in the AFA sets was found to be ~ 345 kJ/mol. The value calculated here matches well the Ellingham diagram as a more stable oxide should have a higher activation energy.

Chapter 4

Oxidation of AFA in Air-Steam Ratios

The goal of this chapter is to present the results of HP and AFA sets in two different air-steam ratios. All other variables were kept the same and same procedures for sample prep and sample characterization. An analysis and calculation of activation energy was performed again with the introduction of different air-steam ratios. Lastly, SEM analysis was used to characterize the oxide formation at the surface.

4.1 Introduction

Petrochemical industries use various air/steam ratios to pre-oxidize/clean out the steel reactor before cooking processes. In the preliminary experiments, all tests were performed at

pure steam environments. In this chapter, introducing an air to steam ratio is done to mimic a realistic pre-oxidation cycle in industry. The study of using air and steam ratios has been done before for other alloys for different applications. For example, Bittel et al. study on 304L stainless steels was oxidized in air and steam environments from 1000°C-1375°C using TGA [15]. Bittel et al. found that air had less oxidation rates at the same temperatures. While both show parabolic rate laws, the steam experiment was easier to determine due to more detectable mass change measurements.

Other studies investigate the effects of air and steam oxidation on aluminum alloys as well. Rebak et al. looked at the oxidation characteristics of a FeCrAl alloy [33]. Rebak et al. determined that at lower temperatures, a two-layer oxide was formed and at higher temperature a single layer of alumina was formed. The significance of these results showed that the behavior of aluminum varies with its alloying elements and on temperature.

Chromia was also studied in steam and air oxidizing environments too. Study by Karthikeyan et al. looked at the air and steam oxidation of IN 617 alloys [34]. Karthikeyan et al. looked at the oxide formation of the alloy and determined it had a mixed-growth model. As exposure of oxidation time increased, spinel variations formed as opposed to just nickel oxide and chromia. Temperature and length of exposure here affects the formation of oxides in chromium alloys.

4.2 Methodology

The methodology followed for the long-term evaluation was described in the previous chapter 3 in the methodology section with a new addition to the experimental procedure and minor change to the availability of the samples. The changes are as followed below:

- Samples used for the experiment were HP, AFA – 2.62%, AFA – 3.9%, and AFA – 3.8%.

- The oxidizing environment was changed to two ratios of air and steam: 1:10 and 1:100. The flow rate of air for 1:100 was set to 4ml/min and the flow rate of 1:10 of air was set to 50ml/min.
- Flow rate of steam was calculated to be 480ml/min and kept the same flow rate as in Chapter 2.

4.3 Mass Change and Determination of Oxidation Kinetics Rate

AFA – 2.6%, AFA – 3.8%, and HP alloys were oxidized for a total of 100 hours in 1:100 and 1:10 air-steam ratios. The same procedures that were used in chapter 3 for kinetic rate determination and activation energy were also applied. Graphs of the mass changes and kinetics are represented below. Additionally, SEM imaging and EDS line scans were performed on the alloys to show the surface chemistry of the oxidized layer.

Mass change tracking was done at each 10-hour cycle for a total of 10 mass change measurements for each sample. Due to the nature of our temperature range selection of 800-900°C, the oxidation experiments exhibited a parabolic rate. Averages of each alloy for each temperature and air-steam ratio were plotted to a graph. Figure 36 summarizes the averages of the alloys for the 1:100 air-steam ratio and Figure 37 summarizes the averages of the alloys for the 1:10 air-steam ratio.

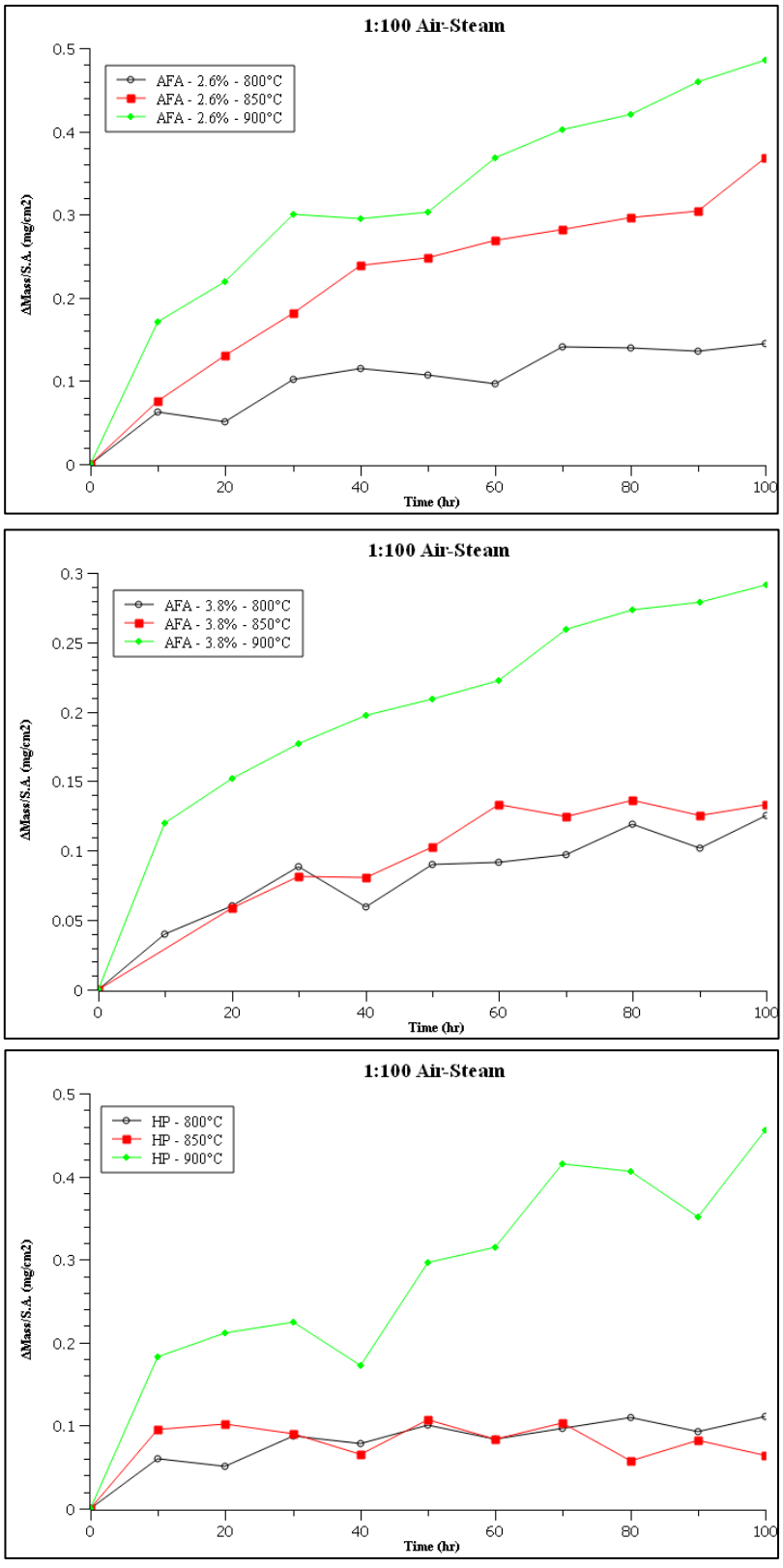

Figure 36. The average mass change of the alloys exposed to 100 hours of oxidation in 1:100 air-steam ratio.

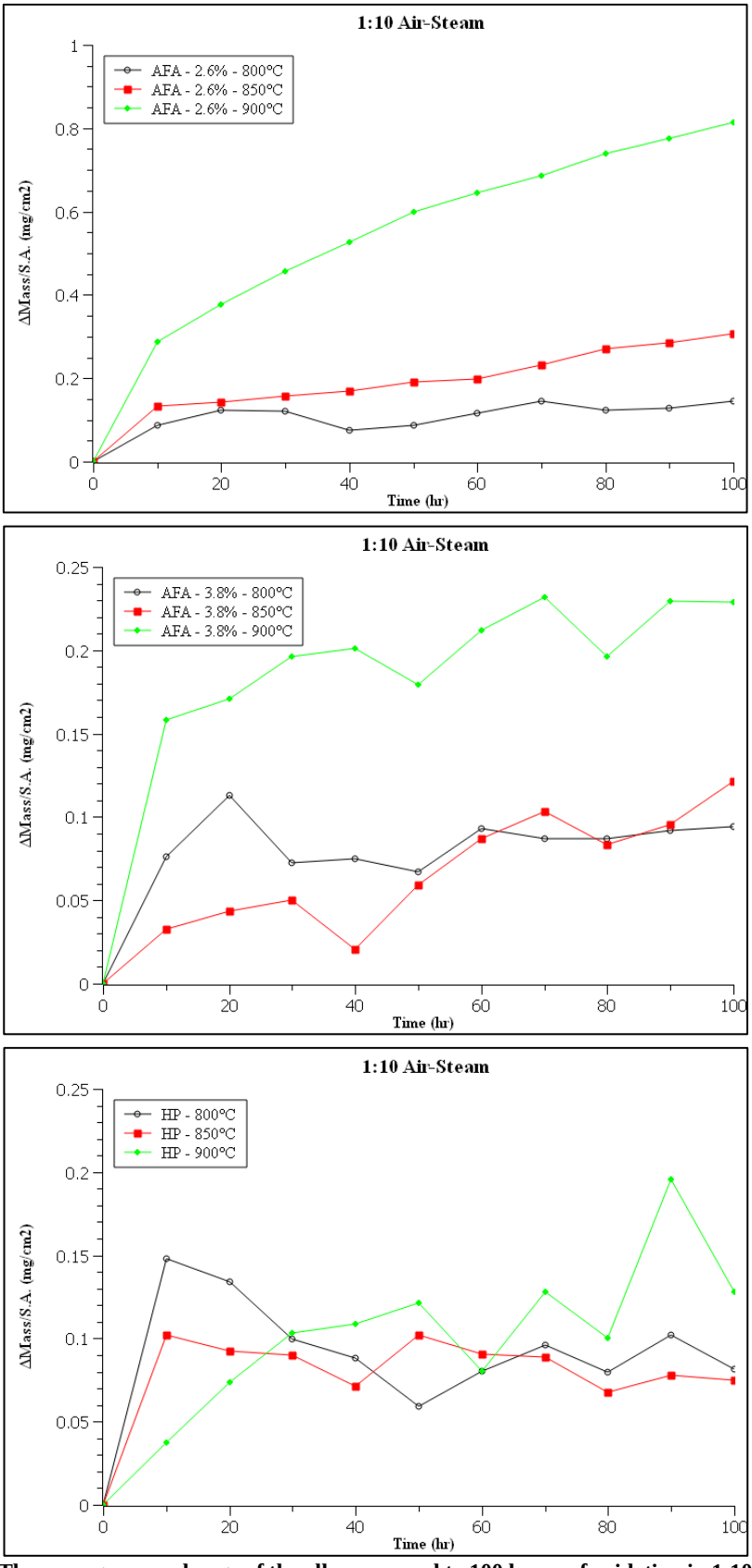

Figure 37. The average mass change of the alloys exposed to 100 hours of oxidation in 1:10 air-steam ratio.

Once the mass changes were plotted, the data was plotted by applying the log to both x and y axis to determine the time exponent rate law, n. The time exponent rate law is then given by the slope of the plotted graph. Figure 38 gives the plots of the alloys with the log function applied for the 1:100 air-steam ratio. It should be noted that some n values were not parabolic in nature and will be discussed later in the chapter.

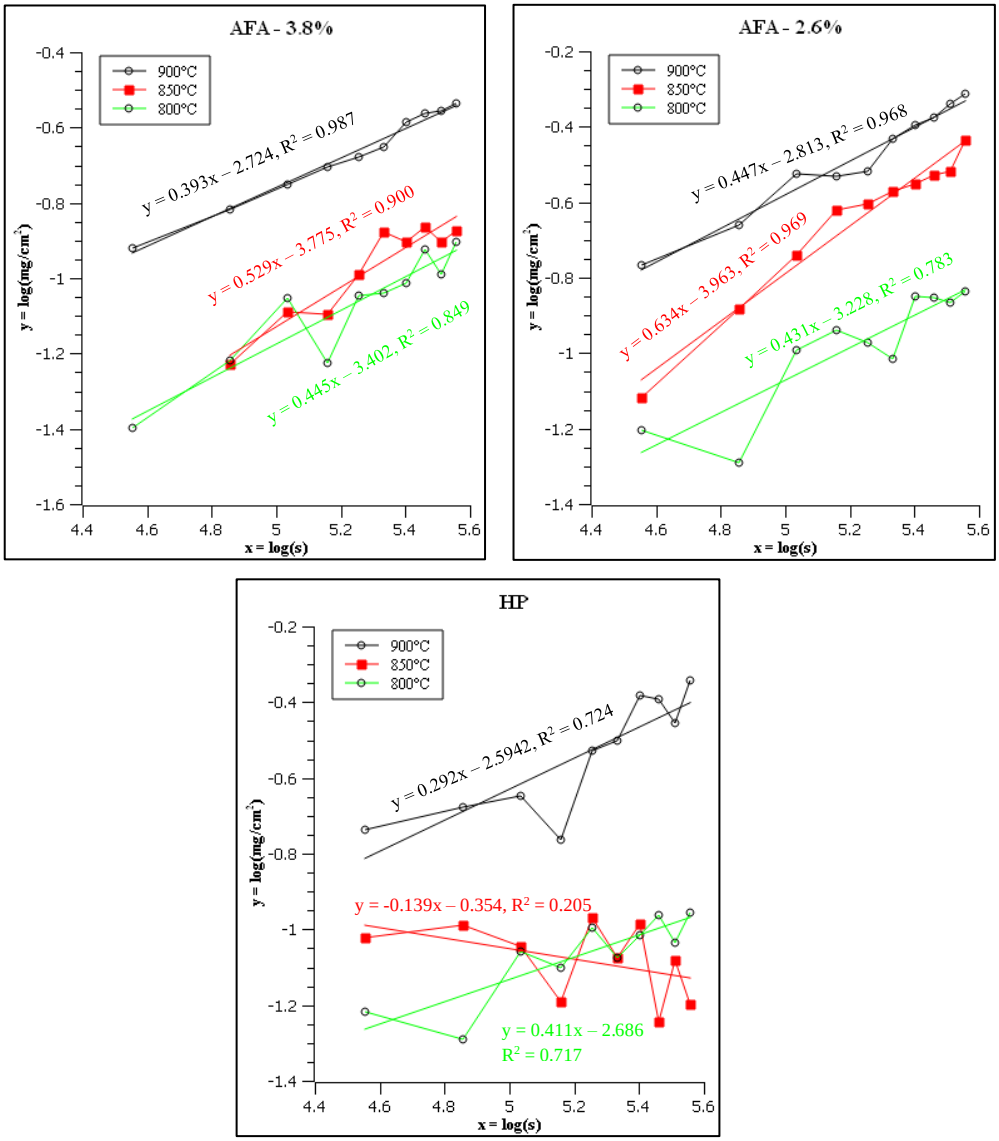

Figure 38. Regression data for the 1:100 air-steam oxidized alloys under three different temperatures oxidized at 100 hours.

To obtain the rate constants for activation energy calculations, mass change was plotted with the time. Where time is in seconds and the mass change is reported in $(kg/m^2)^2$. Figure 39 shows the plots of the alloys for determination of the rate constants for the 1:100 air-steam ratio. Rate constants here are given by the slope of the line when a linear trend is applied.

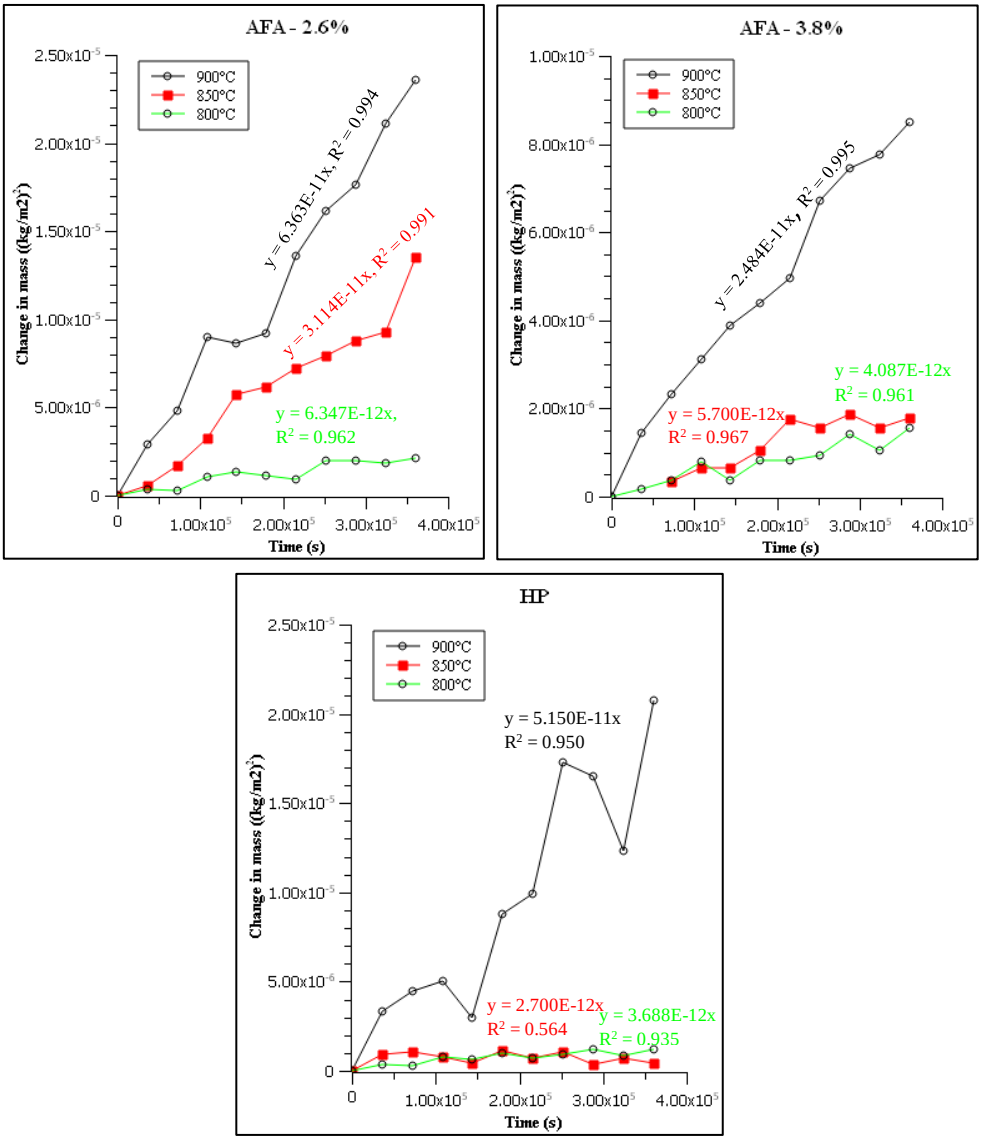

Figure 39. Mass change per area in squared version for each temperature on the AFA and HP alloys for the 1:100 air-steam oxidation. Linear trend setting was performed to obtain equation of the line.

For the 1:10 air steam ratio, the same procedure was applied. Figure 40 shows the plots of the with the log function applied for time exponent rate law determination. Figure 41 shows the plots of alloys for rate constant determination.

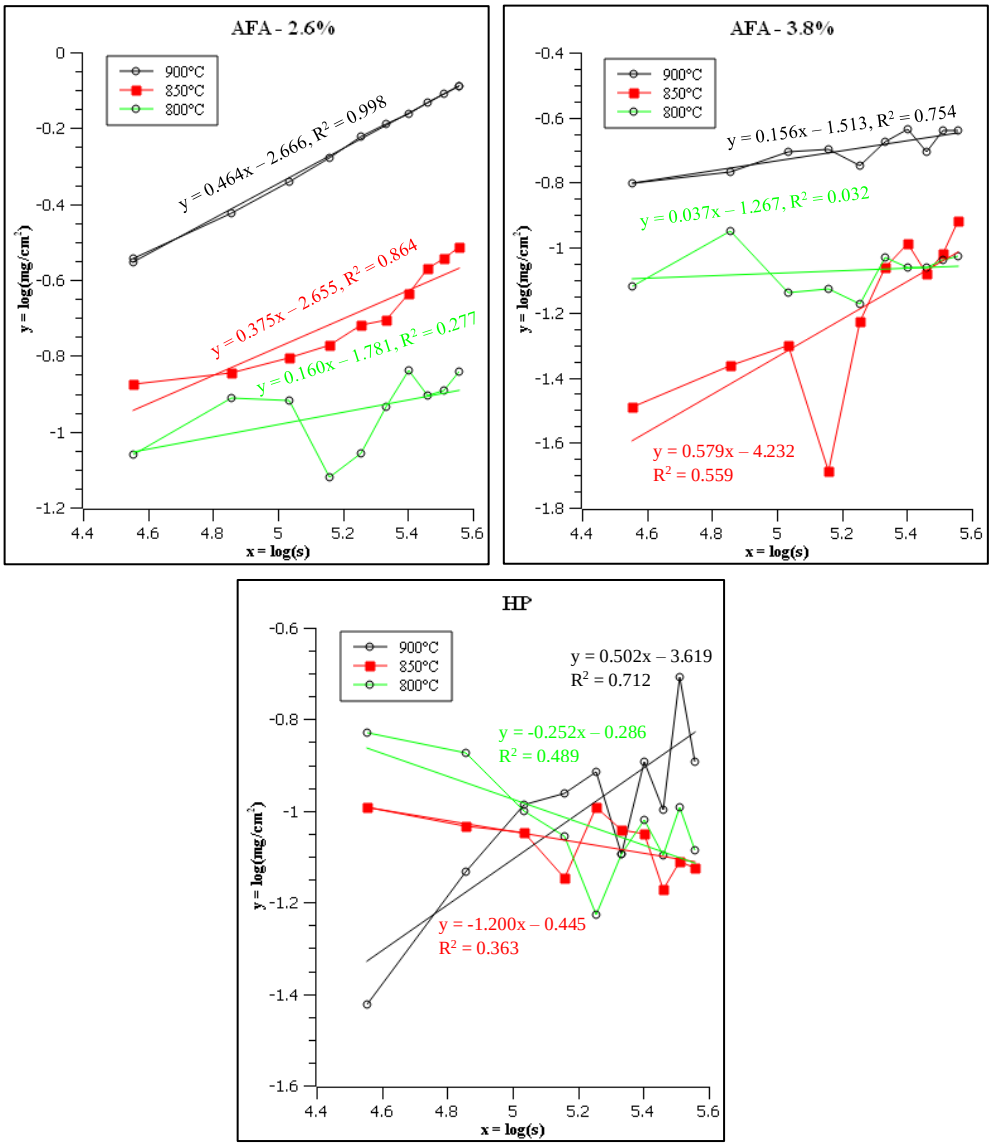

Figure 40. Regression data for the 1:10 air-steam oxidized alloys under three different temperatures oxidized at 100 hours.

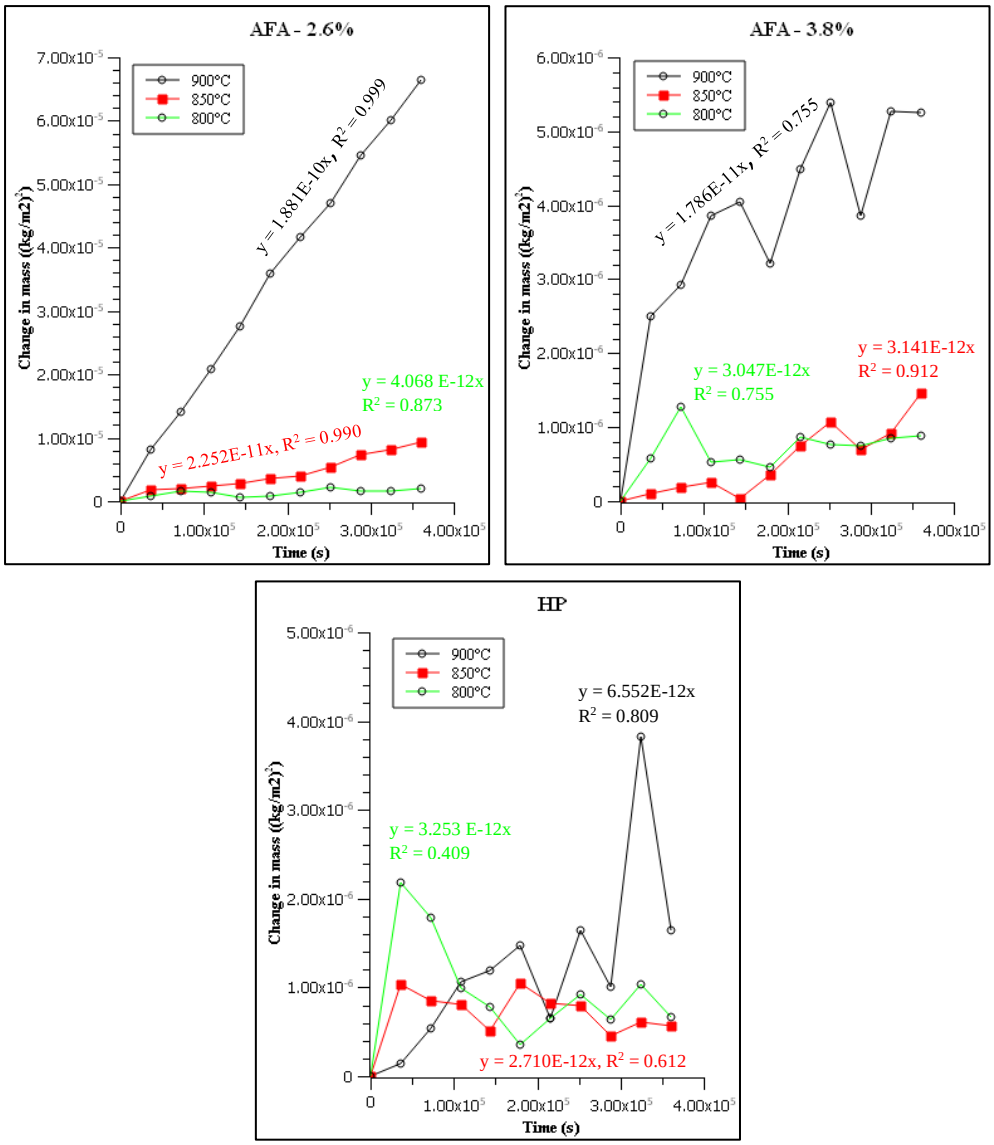

Figure 41. Mass change per area in squared version for each temperature on the AFA and HP alloys for the 1:100 air-steam oxidation. Linear trend setting was performed to obtain equation of the line.

A tabulated summary of the time exponent rate law and the rate constant for each 1:100 and 1:10 air-steam ratio experiment is given below in table 6. In the table, CND means “could not determine” due to the negative nature of the slope. It should also be noted that some experiments have significant deviance from a parabolic rate law.

Table 6. Rate constant (k_p) and time exponent of the rate law (n) for 1:100 and 1:10 air-steam ratios.

Alloy	Air-Steam Ratio	800°C		850°C		900°C	
		n	k_p	n	k_p	n	k_p
HP	1:100	0.41	3.69E-12	CND	2.70E-12	0.29	5.15E-11
AFA - 2.6%	1:100	0.43	6.35E-12	0.63	3.11E-11	0.45	6.36E-11
AFA - 3.8%	1:100	0.45	4.09E-12	0.53	5.70E-12	0.39	2.48E-11
HP	1:10	CND	3.25E-12	CND	2.71E-12	0.50	6.55E-12
AFA - 2.6%	1:10	0.16	6.13E-12	0.38	2.25E-11	0.46	1.88E-10
AFA - 3.8%	1:10	0.04	3.05E-12	0.58	3.14E-12	0.16	1.79E-11

Table 6 values were used in calculation for activation energy. The same procedure was used in chapter 3 where the inverse temperature in Kelvin was plotted with the rate constants with a natural log function applied. Table 7 below shows the calculated activation energies for the 1:100 and 1:10 air-steam ratios.

Table 7. Calculated Activation Energy of HP and AFA alloys in Air-Steam Ratios

Alloy		Activation Energy (Ea)
	Air-Steam Ratio	kJ/mol
HP	1:100	270.7
AFA - 2.6%	1:100	242.4
AFA 3.8 %	1:100	187.0
AFA Average	1:100	214.7
HP	1:10	71.6
AFA - 2.6%	1:10	400.5
AFA 3.8 %	1:10	182.3
AFA Average	1:10	291.4

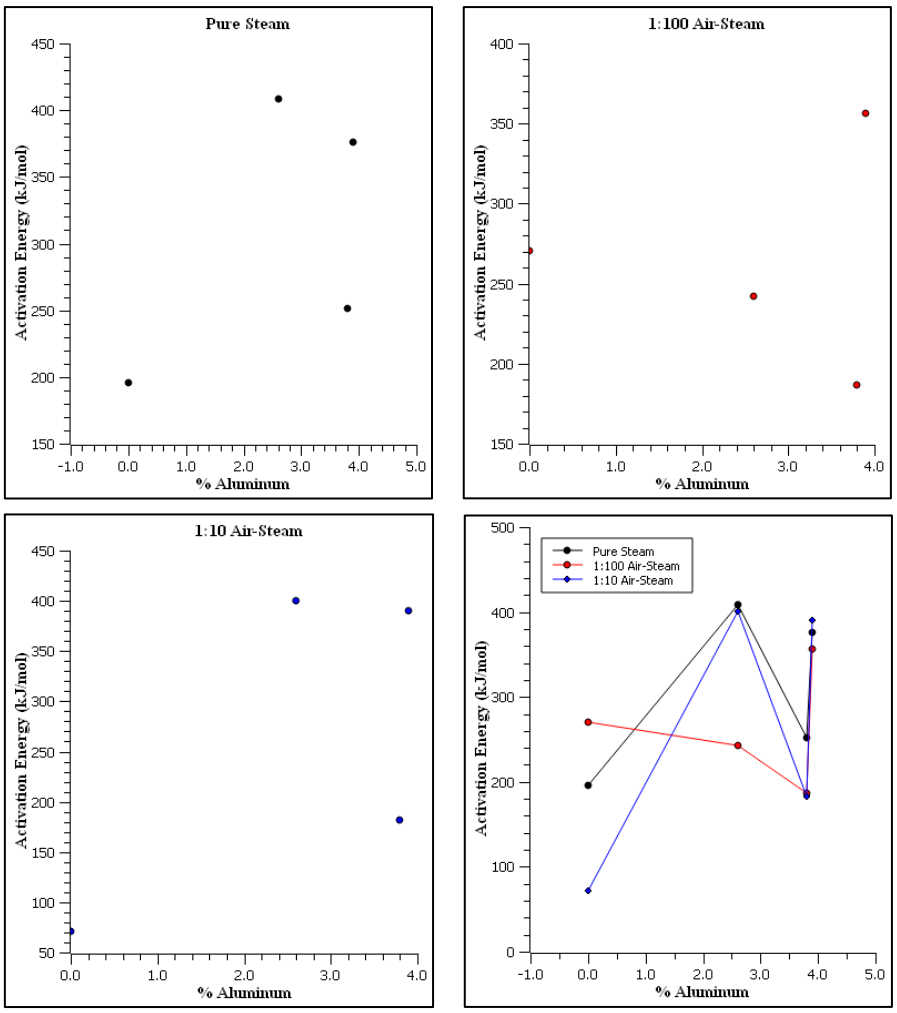

Figure 42. Plots of the percent aluminum against the activation energy for all oxidizing experiments used.

With the activation energies calculated, further analysis of the relationship between aluminum content and activation energy can be observed. The aluminum content of the AFA was plotted against the calculated activation energy. Figure 42 shows the plotted graphs of % aluminum versus the activation for each oxidizing environment that was used.

4.4 Steam Oxidation Comparison to Air-Steam Oxidation

The results of the air-steam oxidation experiments were compared to the pure steam experiments. This was done with the goal of seeing if the oxidation mass changes differ greatly from pure steam experiments. The purpose of this section is to see if there was any major difference in terms of mass change from the pure steam experiments. Figure 43 shows the plots of the comparisons at 800°C, figure 44shows the plots of the comparisons at 850°C, and figure 45 shows the plots of the comparisons at 900°C. For these sections, AFA 2.6% and HP were evaluated only due to sample limitation and that AFA – 2.6% performed generally better than other AFA.

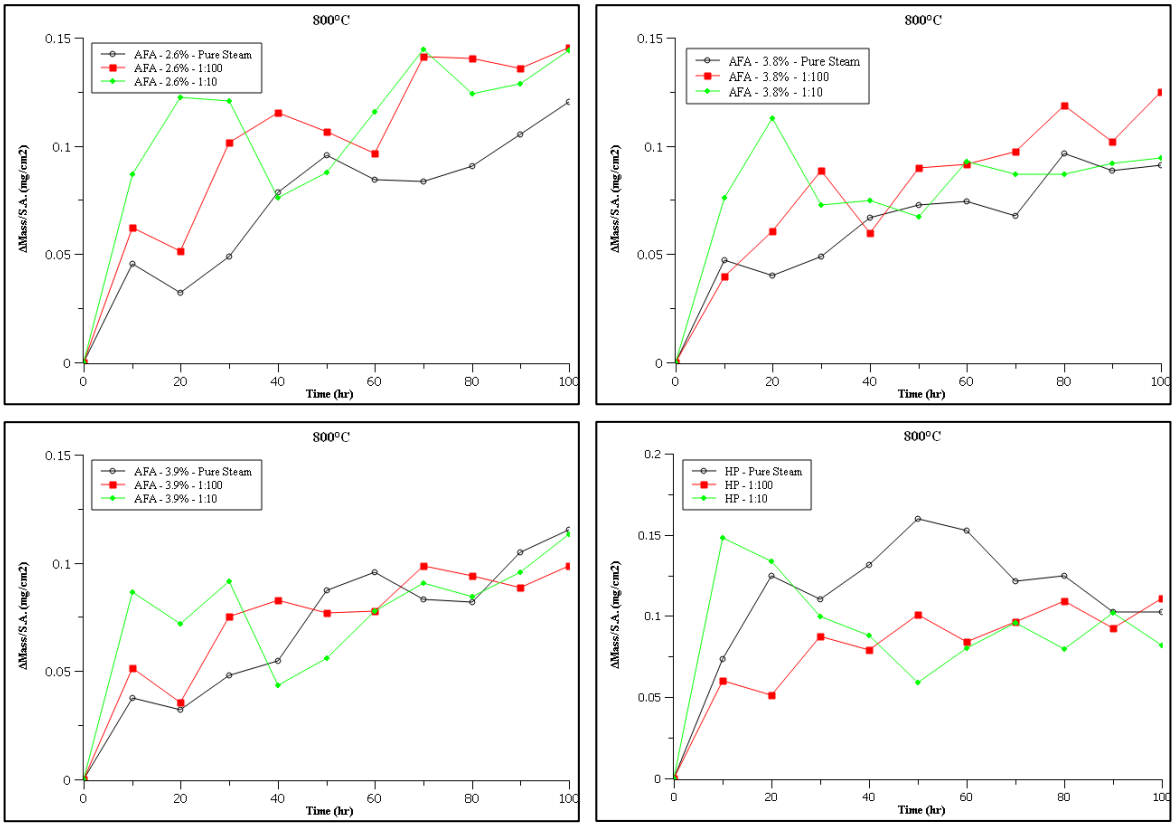

Figure 43. Steam oxidation comparison to air-steam ratios at 800°C.

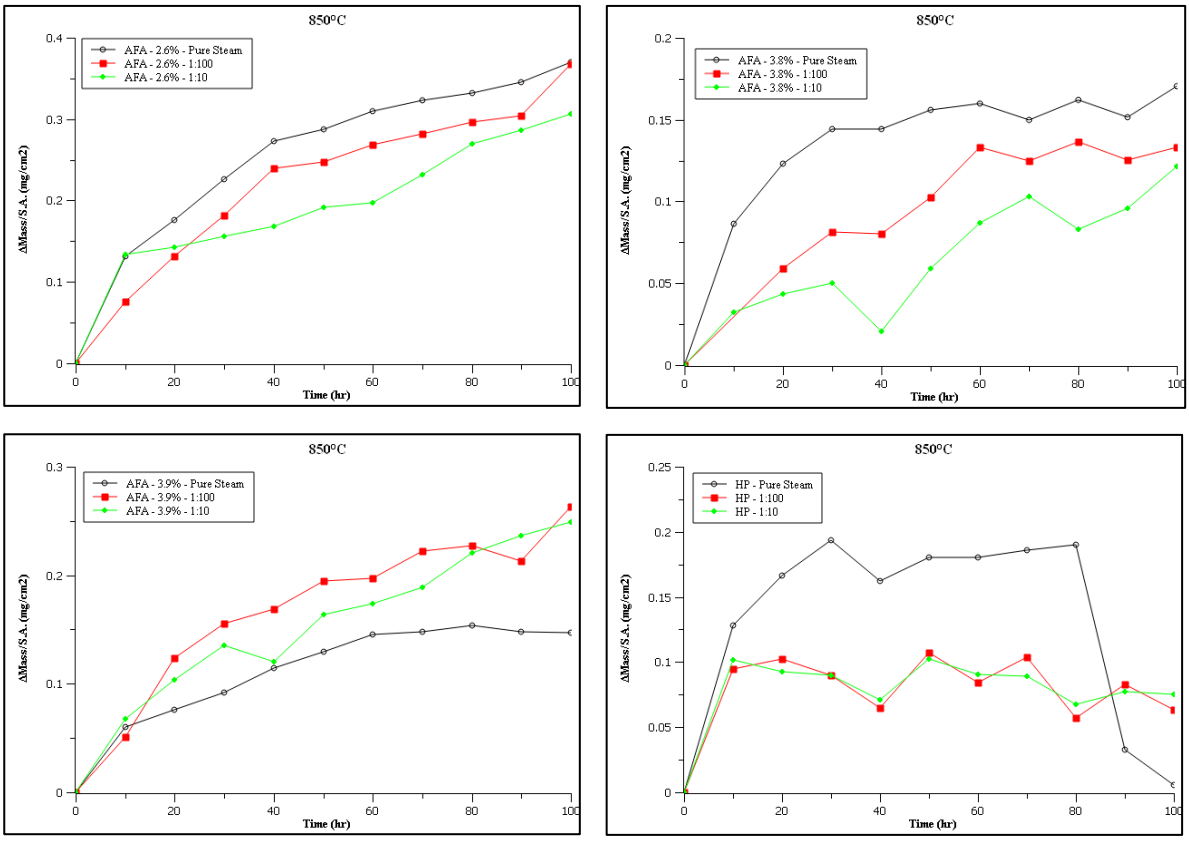

Figure 44. Steam oxidation comparison to air-steam ratios at 850°C.

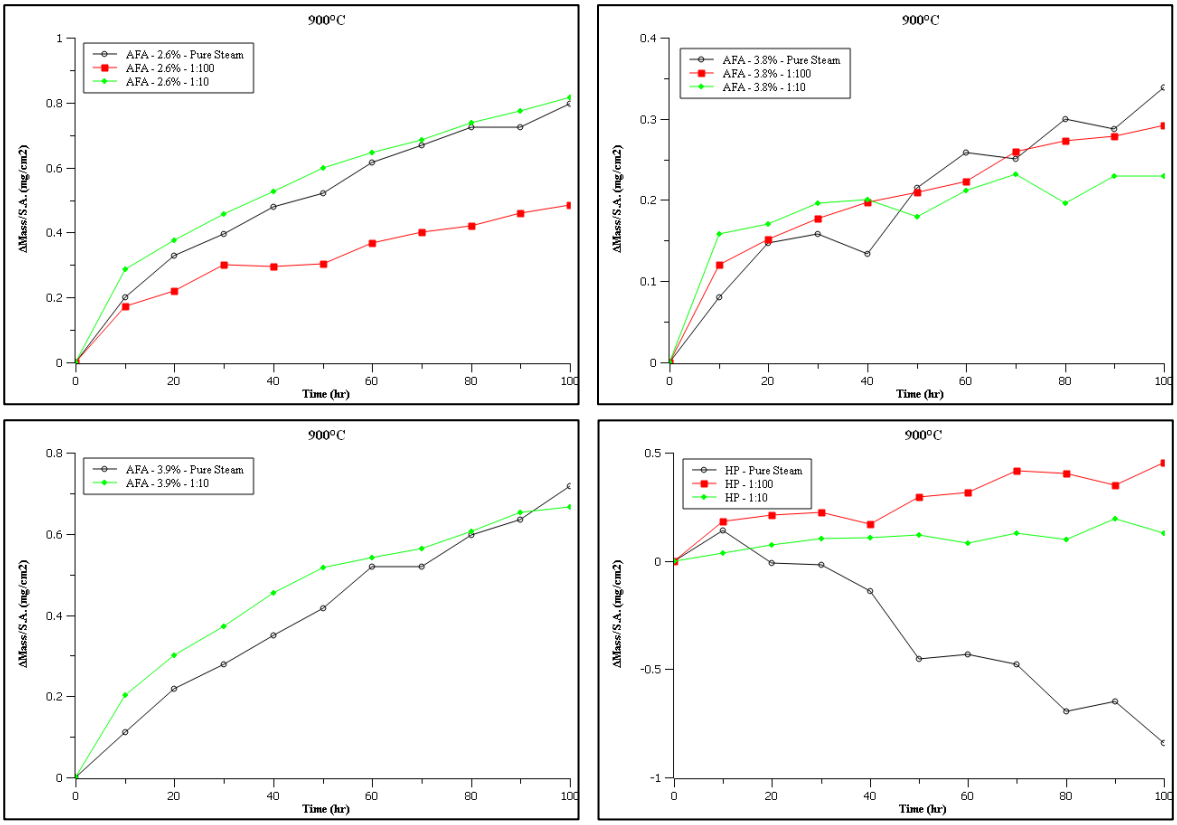

Figure 45. Steam oxidation comparison to air-steam ratios at 900°C.

4.5 SEM Analysis of Air-Steam Oxidation

In the air-steam oxidized experiments, SEM analysis was performed at the oxide scale for chemical analysis and imaging. The primary purpose of the chemical analysis was to perform a line scan from the top oxidized surface to past the oxidized layer. The analysis will indicate an average representation of the overall sample and to see if an oxide layer was formed or not. All SEM analysis and imaging was done with the same equipment in chapter 3 and same parameters

in accelerating voltage, magnification, and length of line scans. Figure 46 shows the images taken by SEM for the 1:100 air-steam ratio and figure 47 shows the images taken by SEM for the 1:10 air-steam ratio.

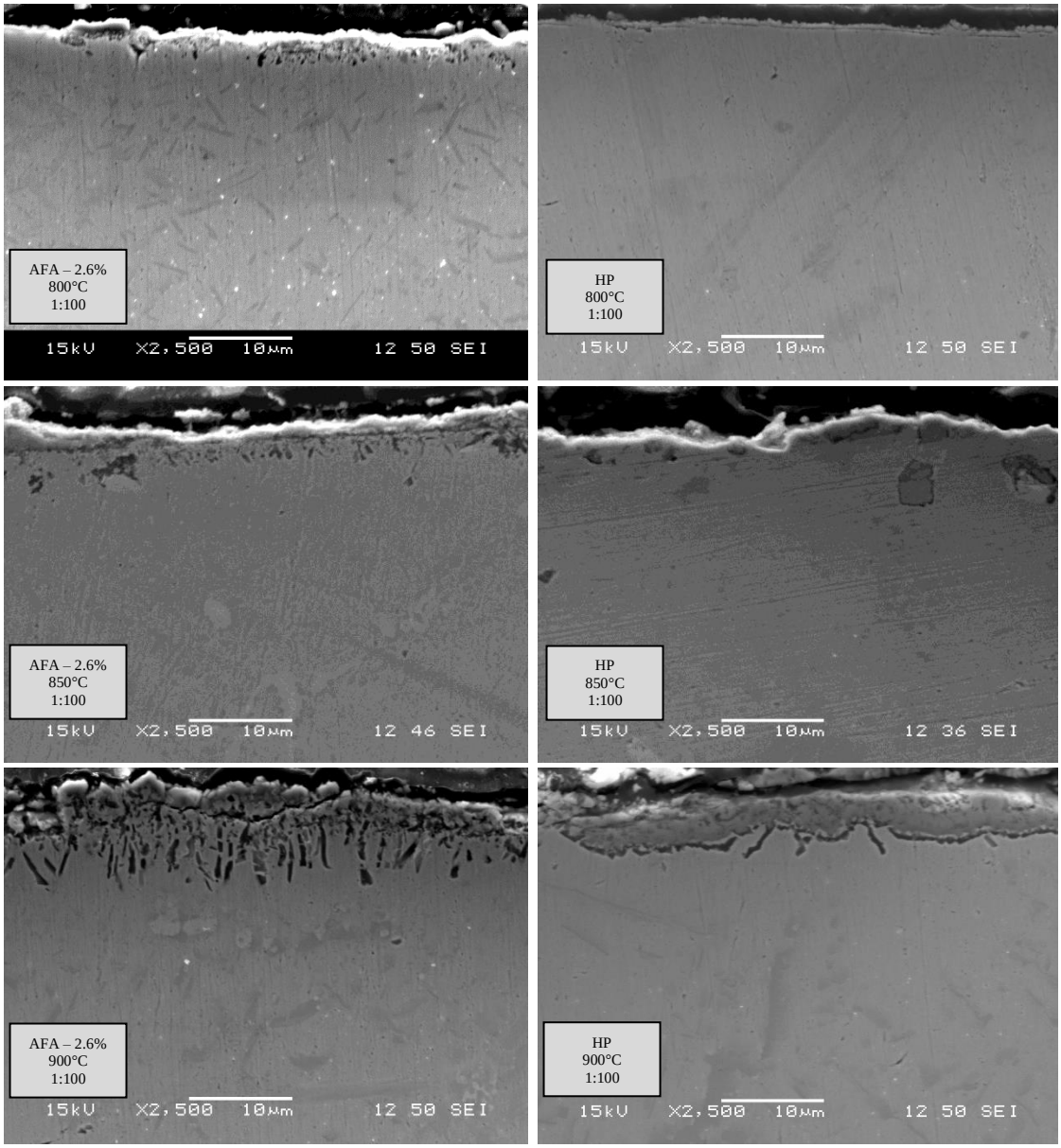

Figure 46. SEM image comparison of HP and AFA – 2.6% in the 1:100 air-steam ratio.

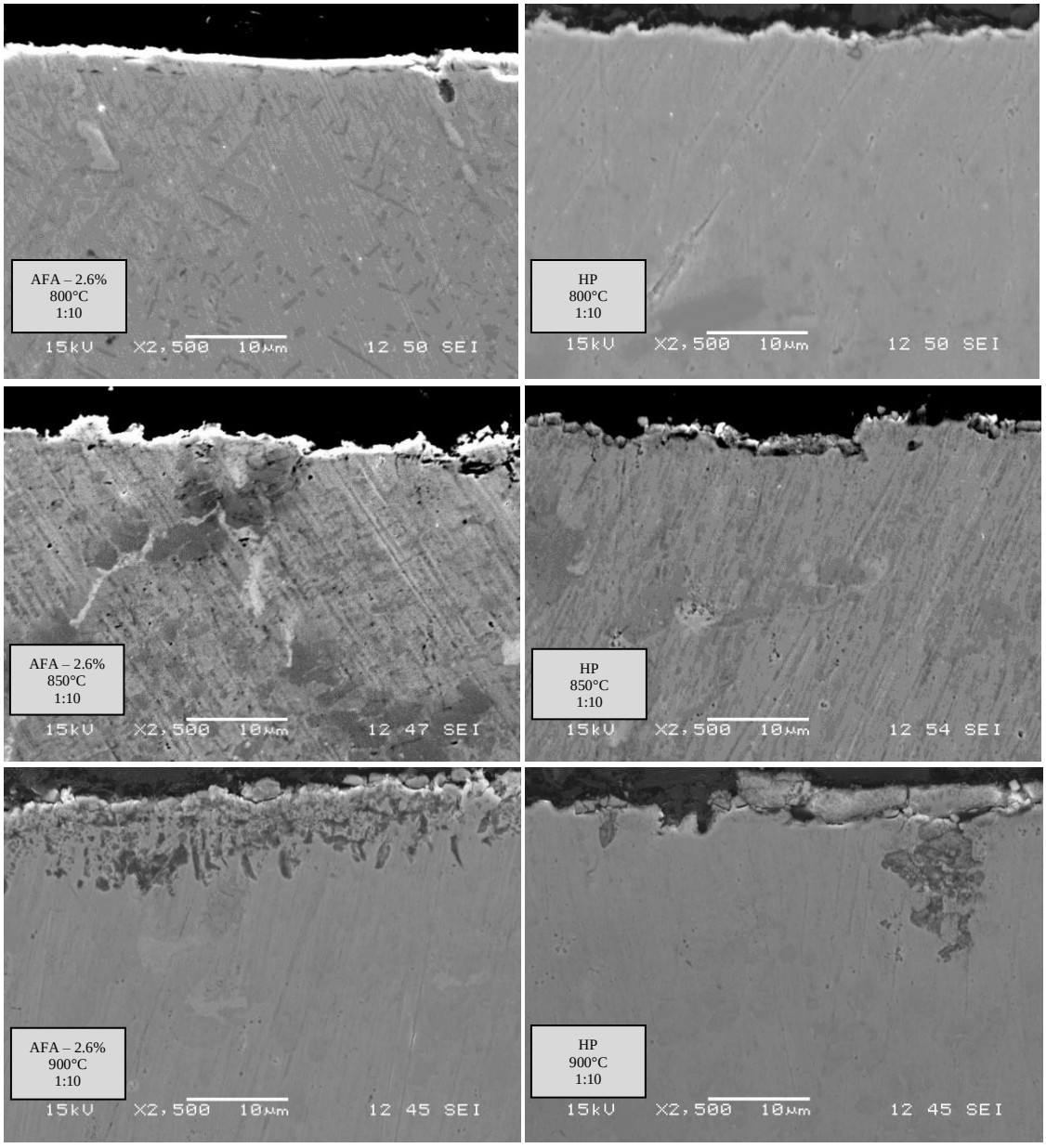

Figure 47. SEM image comparison of HP and AFA – 2.6% in the 1:10 air-steam ratio.

Additionally, line scans were performed on AFA – 2.6% and HP. Line scans were performed for 300 seconds from a the cross-sectioned area of the sample. The line scans started from the top of the cross-sectioned and runs through the oxidized layer. Line scan data was then retrieved and imported to excel to retrieve data points. With the data points, the software:

SciDAVis was used to generate the graphs. Figure 48 shows an image of how the line scans were done during the EDS scanning process.

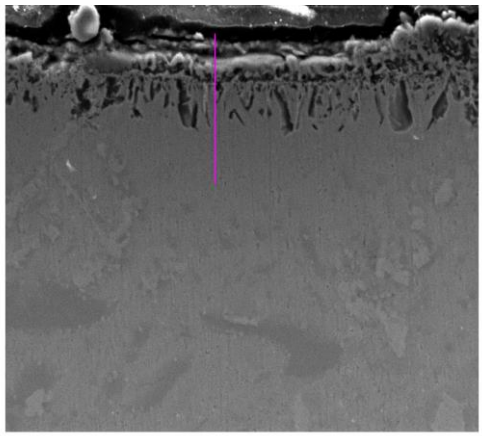

Figure 48. Line scan of AFA – 2.6%. Line starts from the cross-sectioned and into the sample past the oxide layer. Above where the line starts is the Bakelite mount material.

Figure 49 shows the line scan graphs of AFA – 2.6% and HP at the 1:100 air-steam ratio. Figure 50 shows the line scan graphs of AFA – 2.6% and HP at 1:10 air-steam ratio. Line scans were done for approximately 12μm. Each element in the line scans is coordinated with a specific color as per the table legend. The y-axis is labeled as “peak intensity arbitrary” where the SEM gives the value in counts per second (cps).

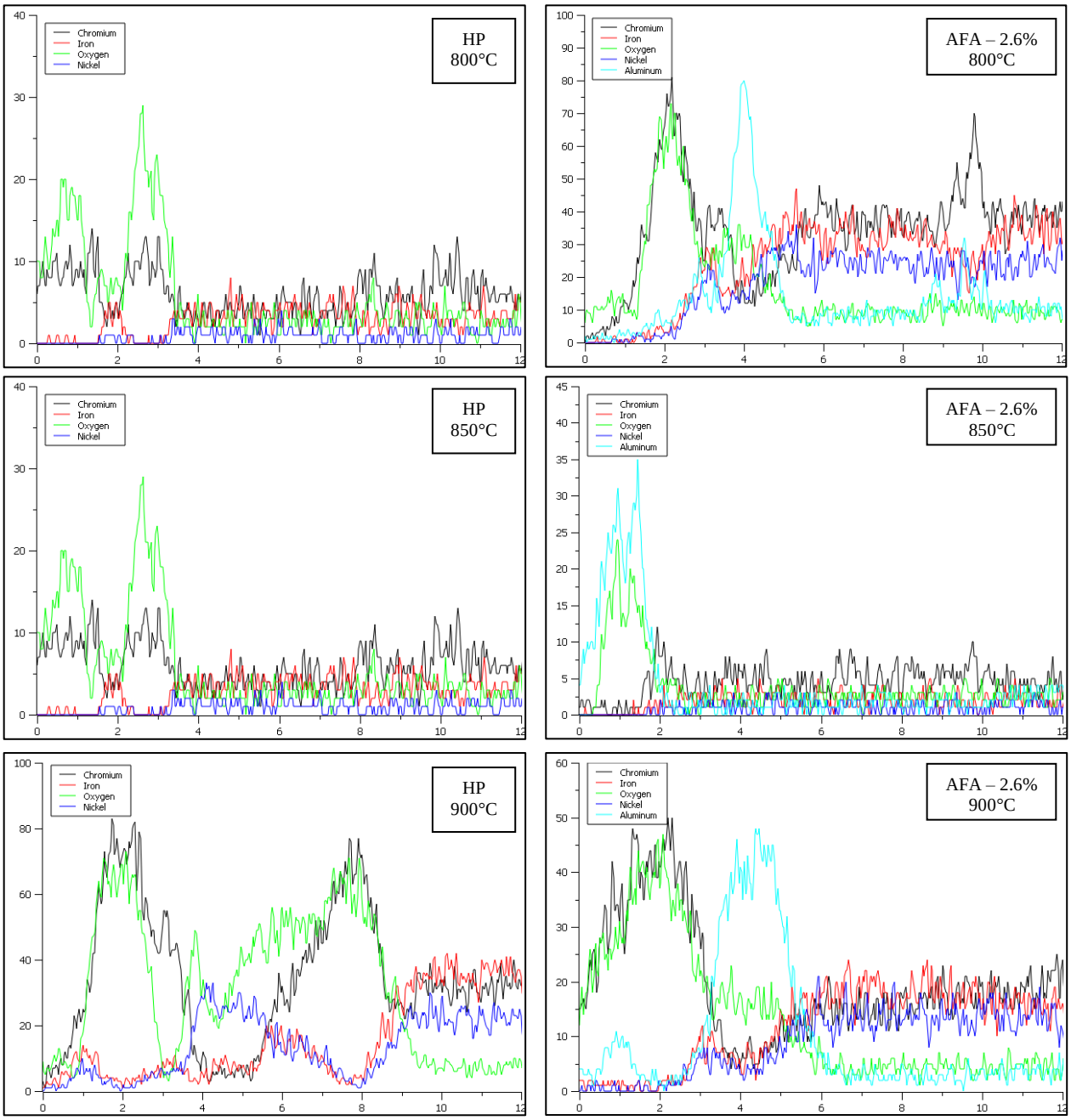

Figure 49. Line scans of AFA – 2.6% and HP at the 1:100 air-steam ratio.

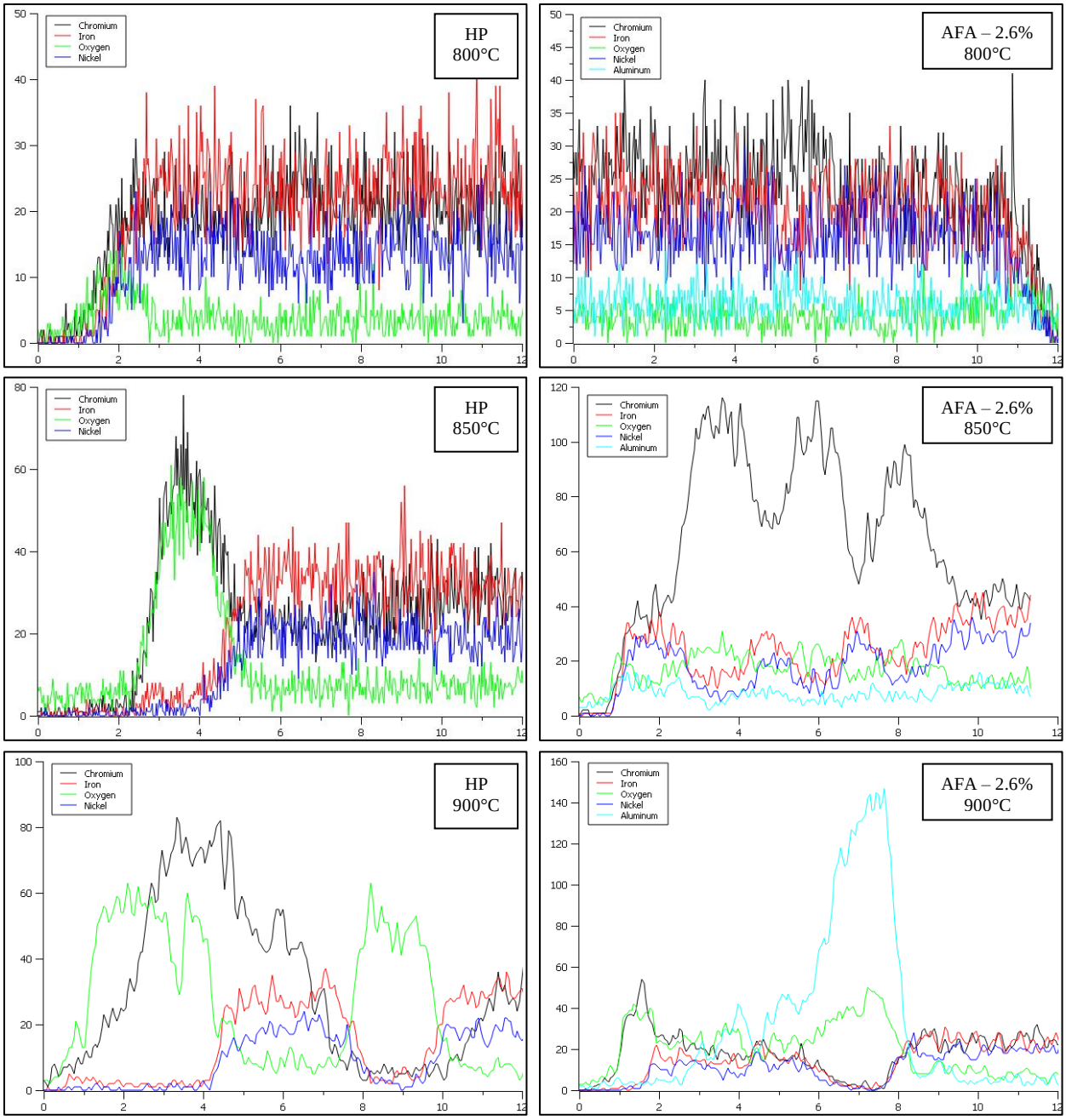

Figure 50. Line scans of AFA – 2.6% and HP at the 1:10 air-steam ratio.

4.6 Summary

Data of samples of AFA and HP were obtained from air-steam oxidation of 1:100 and 1:10 ratios. They were exposed to oxidizing temperatures of 800°C, 850°C, and 900°C degrees for 100 hours. An analysis of the mass change data generated kinetic data to calculate activation energies. Lastly, an analysis of the samples was done via SEM for line scans and imaging.

Based on the mass change data, it had very similar mass changes to the pure steam data where 900°C had the larger mass gains. HP experience mass loss in the 800°C and 850°C 1:10 air-steam ratios and in the 850°C 1:100 air-steam ratio. This meant that HP's data was only viable up to a certain amount of oxidation time due to the spallation of chromia. For the AFA, the kinetic data does perform similarly to the pure steam results. This indicated that in air-steam environments, AFA remains stable varying oxygen rich environments.

In the air-steam oxidizing experiments, the kinetic data is not as stable compared to pure steam experiments. The time exponent rate law was found, however not all samples at each temperature and air-steam ratio were found to be parabolic. It should be noted that in the 1:100 air-steam ratio, HP at 850°C's time exponent rate law was not determined and in the 1:10 air-steam ratio at 800°C and 850°C. This is due to a negative slope from mass loss in the experiment. Regardless of the calculated n values, the calculation for activation energy was performed to check values. The average activation energy was calculated by taking both AFA – 2.6% and AFA – 3.8% values. The average activation energy of the AFA was then found to be ~214.7 kJ/mol for the 1:100 ratio and ~291.4 kJ/mol for the 1:10 ratio. The calculated activation energy values still match well with the pure steam activation energy and literature discussed in earlier chapters. HP had an activation energy of ~270.6 kJ/mol for the 1:100 air-steam ratio and

~71.6 kJ/mol for the 1:10 air-steam ratio. The calculated activation energy of HP at 1:100 air-steam ratio had a good match with the pure steam oxidation and literature.

With the analysis of percent alumina versus activation energy, graphs were obtained for each oxidizing environment. It can be generally said that in the data set, the larger the aluminum content, the higher the activation energy of the alumina oxide. Alumina is formed due to the diffusion of aluminum from the bulk that reacts with the oxygen rich environment. As mentioned earlier, activation energy can be derived from the Arrhenius relationship that used the reaction rate constants. However, it can also be represented in terms of diffusion: $D = D_0 \exp\left(-\frac{Q}{RT}\right)$. Where D is the diffusion coefficient and D_0 is the preexponential factor. The explanation of higher activation energy is due to the relationship between D and K_p, where higher rates of diffusion or reaction rate constant would lead to a lower activation energy. Further analysis from other research has determined the relationship between diffusion coefficient and activation energy. A study by Ping et al. investigated the diffusion kinetics of chromium in the Super304H stainless steel [35]. Ping et al. found in the chromia former that higher diffusion coefficients lead to lower diffusion activation energy.

Overall, can be said that the stability of the oxidation of both HP and AFA are affected compared to pure steam. However, the mass change when compared to pure steam is relatively similar and hence the performance in terms of mass change is also similar. Alumina and chromia both do form readily however with the AFA alloys, chromia is sometimes found at the surface instead of alumina. This needs to be further examined but is thought to be due to the intermetallic that are formed at or near the oxide layer prevent alumina formation.

Chapter 5

Tracking of Aluminum in Long-Term Oxidation

The goal of this chapter is to characterize the performance of AFA alloys at longer periods of oxidation at 1000 hours with a focus on the aluminum profile. The proposed method is to track the concentration of aluminum from the center of the sample to the inner diameter or the surface of the alloy. Using line scans from EDS analysis, the concentration of the aluminum content can be tracked as you move from the center to the surface. Developing an aluminum profile would provide better insight to understand the mobility of aluminum in oxidizing environments. Additionally, it would help in determining mechanisms or obstacles in play that would prevent the formation of alumina at the surface as observed in previous chapters. The selected parameters were to oxidize at 900°C at a 1:100 air-steam ratio. The parameters were selected to be "worst-case" scenario the alloy would experience with target to remain in the parabolic nature regime.

5.1 Introduction

Diffusion profiles of dopants in semiconductors have been researched as such, the semiconductor technology has greatly improved in the past two decades or so. Work done by Tsai et al. has investigated concentration profiles of phosphorus diffusion in silicon [36]. With experimental work, the diffusion profile of phosphorus was fitted into Fick's law of diffusion.

Phosphorus was tracked as an impurity concentration using differential conductivity. The sheet conductance was then obtained in linear scale and semi-logarithmic scale. Finally, the concentration profile was obtained from the sheet conductance. Another work by Benzarti et al. looked at magnesium diffusion profile in GaN that were grown by metal-organic vapor-phase-epitaxy [37]. The use of a secondary ion mass spectroscopy allowed for the magnesium profiles to be determined. The concentration of magnesium was tracked as a function of depth with variable growth temperatures from 1090°C to 1150°C.

With the aim of this chapter, a concentration profile of aluminum is desirable. Studies of how aluminum is depleted during oxidation have been investigated for other types of applications such as turbines. A study by Jalowicka et al. looked at the aluminized CoNiCrAlY coating during higher temperature oxidation [38]. They found that different oxidizing temperatures, the alumina scale had different lengths. Furthermore, different precipitates such as the γ-precipitate phase are attributed to an aluminum depleted zone.

Other alloys such as the Fe-Cr-Al have been studied as well. Marechal et al. looked at the oxidation behavior of Fe-Cr-Al alloys of the aluminum content [39]. They have determined that the oxidation resistance is affected when the aluminum content has fallen below the critical layer due to the insufficient amount of base metal forming new oxide. In addition, aluminum depletion is observed at temperatures over 1100°C. How aluminum behaves under oxidation is crucial as it can vary depending on the temperature and alloying elements.

5.2 Methodology

In this chapter, the sample prep and selection remained the same as previous chapters. This is done to keep consistency and the overall better understanding of the specific alloy. It

should be noted again that due to the limited number of materials, only the HP and AFA 2.6% samples were used for the long-term oxidation experiments. However, in this chapter, the oxidation time was extended to reflect a long-term oxidation and the cycling of on/off the furnace was not performed until the end of the oxidation cycle. Additionally, there was only one selected temperature at 900°C. Three oxidation times were examined in this study at 0 hours (no oxidation), 100 hours, and 1000 hours in pure steam.

Microstructural Analysis

In this chapter, a deeper microstructural analysis was performed as oxidized samples at 1000 hours may exhibit a different structure. Microstructures of both HP and AFA – 2.6% was imaged at each oxidation time (0 hours, 100 hours, and 1000 hours). To obtain optical images, the samples had to be etched first. A different etchant solution than the one in chapter 2 was made to specifically etch these HP and AFA – 2.6% alloys. The mixture contained 20wt% of nitric acid and 4wt% of hydrofluoric acid. The mounted and polished samples were then exposed to the etchant for approximately eight seconds before rinsing off.

Composition Analysis and Aluminum Tracking

Element composition was tracked specifically for the 1000 hour oxidized samples. Line scans were performed as usual but with longer depths of ~30μm instead of the 12μm from previous chapters. Additionally, multiple line scans were performed to obtain an average. Each sample had line scans taken from the left, middle, and right side of the samples under SEM-EDS. Each element detected was then averaged out for the average composition. Along with line scans, a selected box area was also performed along with the sample as well. A box area was drawn from the top oxide layer with a depth of ~5μm. This was performed as needed until the depth

was ~35µm deep. Composition values were then analyzed and plotted to show composition changes through depth at 1000 hours.

5.3 Mass Change and Composition Check

Mass change was measured for the 100 hours and 1000 hours experiments for the HP and AFA – 2.6% alloy. Table 8 shows the before and after mass change after each oxidation period. HP experienced mass loss in both 100 hours and 1000 hours. AFA – 2.6% experienced mass gain in both 100 hours and 1000 hours.

Table 8. Mass change of HP and AFA – 2.6% for each oxidation period

Alloy	Oxidation Time (hrs)	Before (g)	After (g)	Percent Change
HP	100	9.07839	9.07709	0.014 (decrease)
HP	1000	10.66251	10.65236	0.0952 (decrease)
AFA - 2.6%	100	11.78359	11.78769	0.035
AFA - 2.6%	1000	9.12020	9.12674	0.072

To check for the composition, a baseline of the composition was first established by taking a general area scan of the sample at x100 and compared to the reported nominal compositions by the vendor from Table 1 in chapter 3. Three separate locations were scanned for a total of 300 seconds arbitrarily (location A, B, and C) near the center of the sample. With three different locations and compositions given, an average was calculated for the HP and AFA – 3.6% alloy. Figure 51 shows the compositions given by SEM-EDS and the average for the HP alloy and figure 52 shows the composition and average for AFA – 2.6%.

Location A			Location B			Location C		
Element	Weight%	Atomic%	Element	Weight%	Atomic%	Element	Weight%	Atomic%
C K	3.92	15.66	C K	4.02	16.03	C K	3.81	15.29
Si K	1.53	2.62	Si K	1.54	2.62	Si K	1.58	2.72
Cr K	28.11	25.96	Cr K	27.80	25.59	Cr K	27.22	25.23
Fe K	33.28	28.62	Fe K	33.99	29.13	Fe K	34.20	29.52
Ni K	33.16	27.13	Ni K	32.65	29.13	Ni K	33.18	27.24
Totals	100.00		Totals	100.00		Totals	100.00	

Average

Element	Weight%	Atomic%
C K	3.9	15.7
Si K	1.6	2.7
Cr K	27.7	25.6
Fe K	33.8	29.1
Ni K	33.0	27.8
Totals	100.00	

Figure 51. Arbitrarily locations of HP alloy near the center with SEM-EDS composition taken at x100. The average composition is given in the bottom table.

Location A			Location B			Location C		
Element	Weight%	Atomic%	Element	Weight%	Atomic%	Element	Weight%	Atomic%
C K	3.81	14.98	C K	3.81	14.98	C K	3.81	14.96
Al K	2.32	4.06	Al K	2.32	4.06	Al K	2.49	4.36
Si K	1.47	2.47	Si K	1.47	2.47	Si K	1.48	2.48
Cr K	29.22	26.55	Cr K	29.22	26.55	Cr K	28.93	26.24
Fe K	26.68	22.57	Fe K	26.68	22.57	Fe K	27.13	22.91
Ni K	36.50	29.37	Ni K	36.50	29.37	Ni K	36.16	29.05
Totals	100.00		Totals	100.00		Totals	100.00	

Average

Element	Weight%	Atomic%
C K	3.6	14.3
Al K	2.4	4.3
Si K	1.5	2.5
Cr K	29.0	26.5
Fe K	27.0	23.0
Ni K	36.5	29.5
Totals	100.00	

Figure 52. Arbitrarily locations of AFA – 2.6% alloy near the center with SEM-EDS composition taken at x100. The average composition is given in the bottom table.

Recalled from Table 1, the average values of the composition here do match well with the nominal that was given from the vendor. This assured that the SEM-EDS was detected with accurate values and the samples are true to what was reported.

5.4 Microstructure of HP and AFA 2.6%

Microstructures of the AFA and HP alloy were obtained via SEM for 0 hours, 100 hours, and 1000 hours at 900°C. Figure 53 shows the comparison of the AFA and HP alloy for each temperature oxidized. The microstructure of AFA – 2.6% does not change when oxidized for 1000 hours at 900°C compared to 100 hours and 0 hours. This same observation was held for HP alloy as well. Microstructural changes were not observed and the oxidation at 900°C for all time ranges has no effect.

With verification of no change to the microstructure, a check for the composition was made again to see if there was any difference in the bulk. A box area scan via SEM-EDS was performed in the bulk material of the oxidized sample for 100 hours and 1000 hours for the AFA – 2.6% and HP alloy. Each alloy for each time was scanned three times to find an average concentration. The tabulated values are found in figure 54.

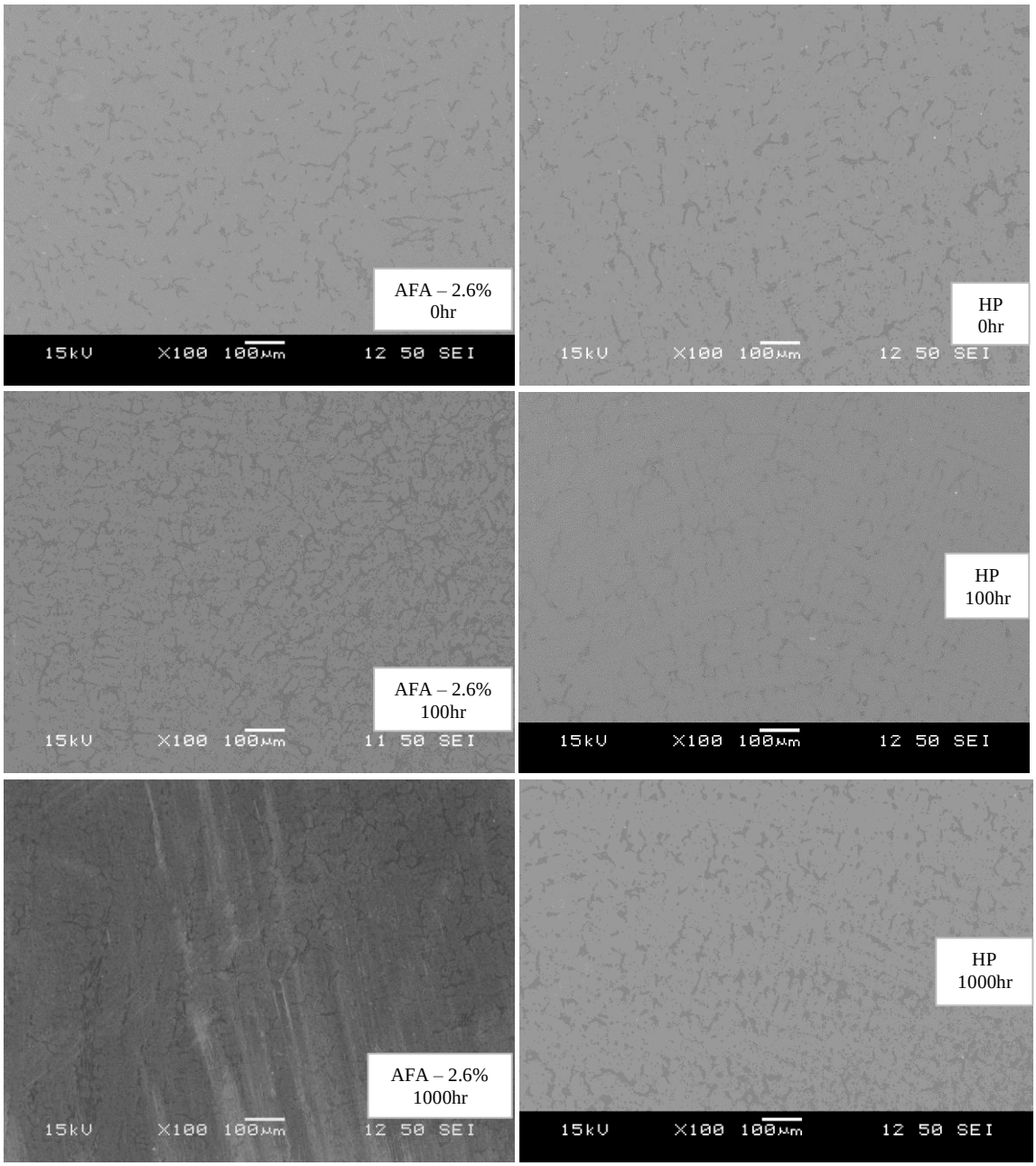

Figure 53. SEM images of microstructure of AFA and HP alloy at 0 hours, 100 hours, and 1000 hours.

HP - 100hr					
Scan	Al	Cr	Ni	Fe	Si
a	0.0	27.8	34.6	36.0	1.6
b	0.0	27.4	35.3	35.6	1.7
c	0.0	27.5	34.4	36.4	1.7
Average	0.0	27.6	34.8	36.0	1.7

HP - 1000hr					
Scan	Al	Cr	Ni	Fe	Si
a	0.0	29.4	33.5	35.5	1.6
b	0.0	30.2	33.3	34.7	1.8
c	0.0	29.3	33.5	35.6	1.6
Average	0.0	29.6	33.5	35.3	1.7

AFA – 2.6% - 100hr					
Scan	Al	Cr	Ni	Fe	Si
a	2.8	30.6	38.1	26.8	1.8
b	2.7	30.3	38.2	27.2	1.6
c	2.8	31.8	37.0	26.9	1.6
Average	2.8	30.9	37.8	27.0	1.6

AFA – 2.6% - 1000hr					
Scan	Al	Cr	Ni	Fe	Si
a	3.0	30.6	37.3	27.3	1.8
b	3.0	30.3	37.8	27.1	1.8
c	3.1	30.6	37.4	27.2	1.8
Average	3.0	30.5	37.5	27.2	1.8

Figure 54. Tabulated values of the bulk scans of AFA – 2.6% and HP alloy at 100 hours and 1000 hours.

5.5 Line scans and Box Scans of HP and AFA – 2.6%

Line scans were performed on the AFA – 2.6% and HP alloy as well. Line scans at 0 hours and 1000 hours were performed and compared for their respective elements. Line scans were done via SEM-EDS and had a minimum line depth of 30μm and scanned for five minutes. The intensities of each element were obtained and plotted separately for comparison. An example is given to show a typical line scan that was performed on the sample in figure 55. The three elements of interest were the nickel, chromium, and aluminum content in the samples. Figures 56 shows the nickel content for the AFA – 2.6% and HP alloy.

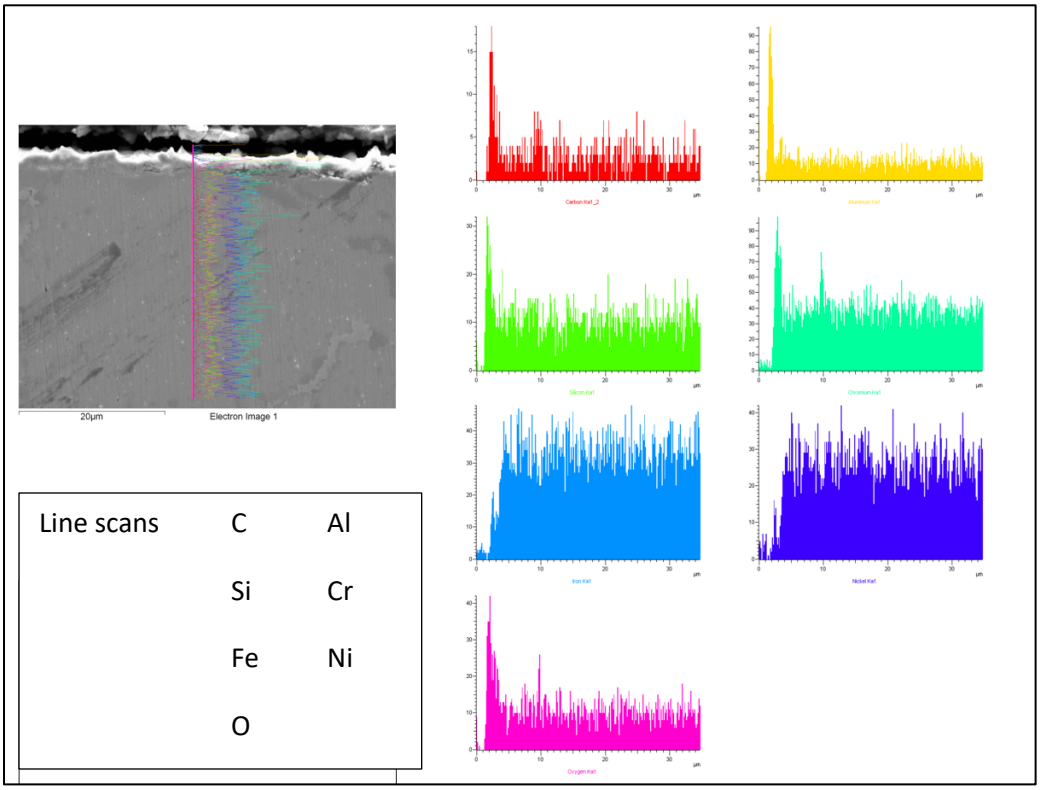

Figure 55. Example line scan that was performed on the long-term oxidized sample. The line scan graphs were then converted to tabulated values for post processing.

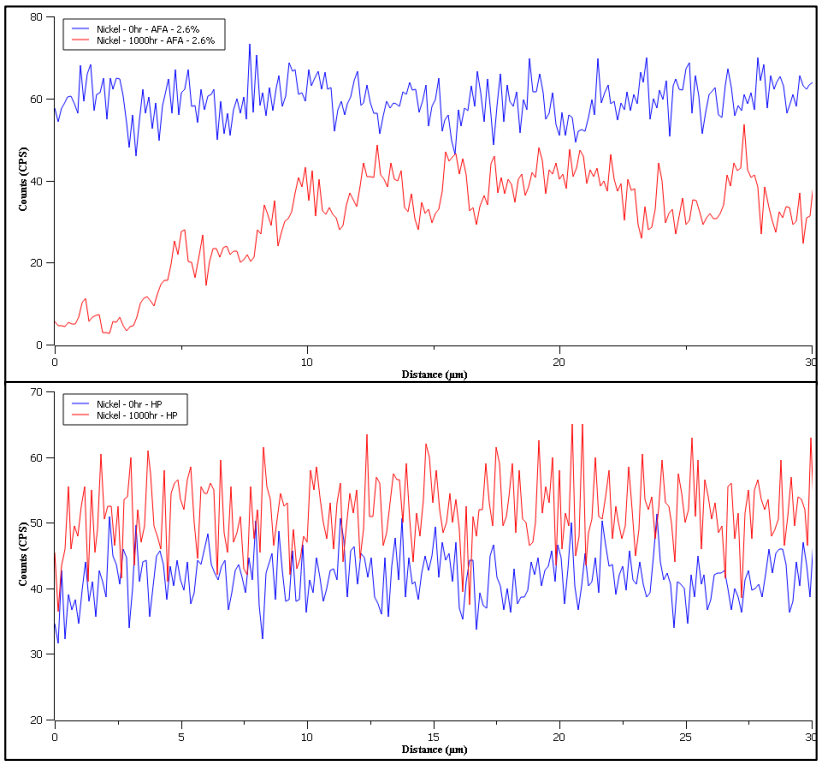

Figure 56. Nickel content of AFA – 2.6% and HP alloy for 0 hours and 1000 hours at 900°C

Elemental scans for chromium and aluminum were also obtained each time. Figure 57 shows the chromium content for the AFA – 2.6% and HP alloy. Lastly, AFA – 2.6% was scanned for aluminum content.

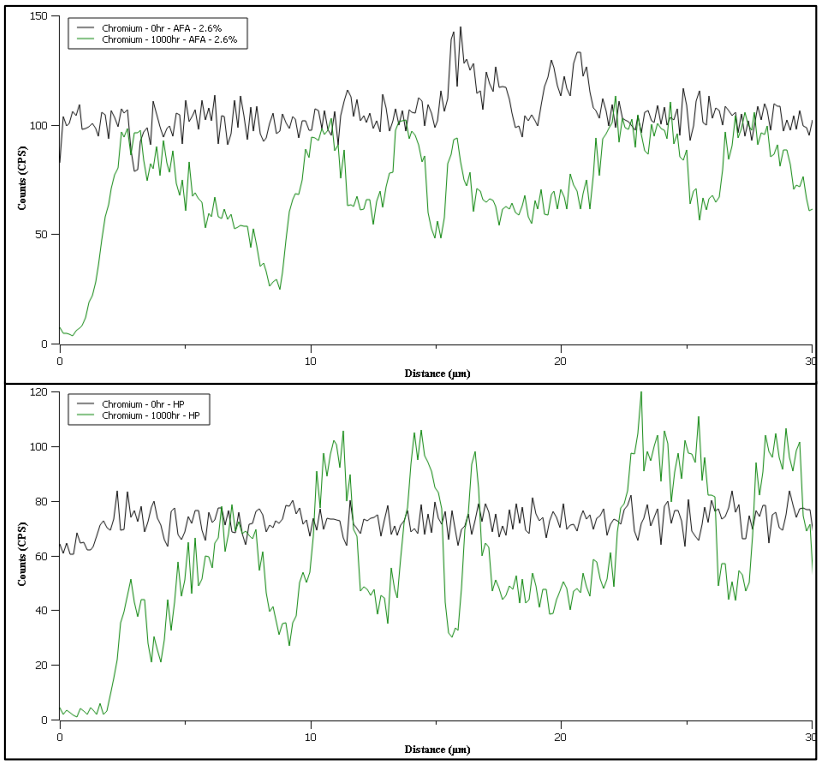

Figure 57. Chromium content of AFA – 2.6% and HP alloy for 0 hours and 1000 hours at 900°C

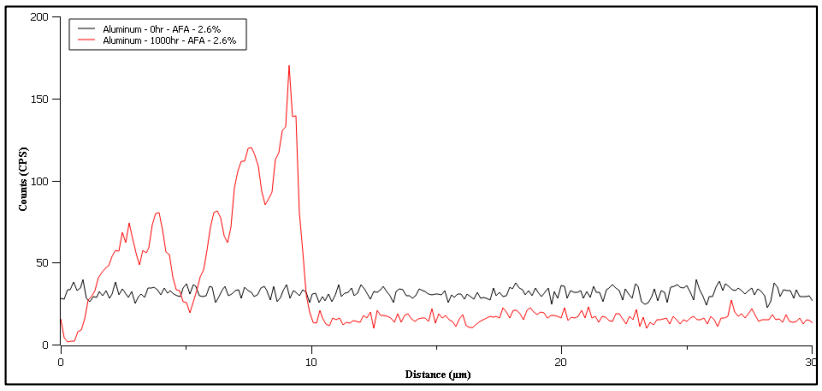

Figure 58. Aluminum content of AFA – 2.6% for 0 hours and 1000 hours at 900°C

Due to the limitation of the line scans of only providing a single point data, it was not ideal to continue the analysis of the aluminum profile. This led to the decision and use of the box area scans. Instead of applying a straight-line scan, a box area was drawn at the top layer and scanned over the area. Additional scans were then done with the new box drawn below the previous box. Tracking of the depth was done with the scale bar of the image and ImageJ processing. To keep the area of the box as similar as possible, a traced-out paper cutout was used to recreate the box areas. Figure 59 shows the box area scans for HP and the boxes that were drawn throughout the depth of the sample for 1000 hours. The depth of the scans was made to reach at least 30µms with a scan time of five minutes per box.

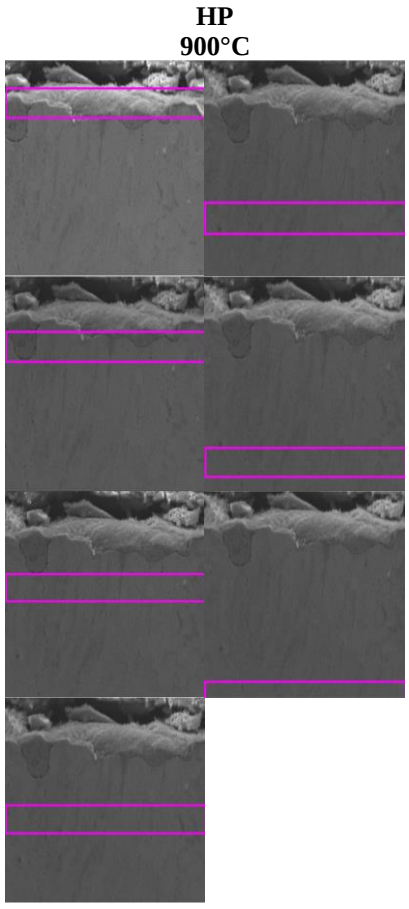

Figure 59. Box area scans for HP alloy at 900°C for 1000 hours.

Table 9. Box Area scans for chromium content in HP alloy oxidized for 1000 hours at 900°C.

HP - Box Area Scan Average of Chromium

Distance A	Chromium A	Distance B	Chromium B	Distance C	Chromium C	Average Distance	Average Chromium	S.D. Cr
2.0	60.5	3.8	45.9	4.0	40.2	3.3	48.8	10.5
7.0	30.3	9.4	20.3	10.2	19.4	8.9	23.3	6.1
11.7	19.1	14.5	18.7	15.5	18.5	13.9	18.8	0.3
17.0	18.1	20.2	17.6	20.8	16.7	19.3	17.5	0.7
22.7	16.1	25.3	16.9	25.3	16.5	24.4	16.5	0.4
28.0	19.0	29.5	20.2	29.7	19.7	29.0	19.6	0.6
33.0	21.4	34.6	21.7	34.4	20.5	34.0	21.2	0.6

Table 10. Box Area scans for nickel content in HP alloy oxidized for 1000 hours at 900°C

HP - Box Area Scan Average of Nickel

Distance A	Nickel A	Distance B	Nickel B	Distance C	Nickel C	Average Distance	Average Nickel	S.D. Ni
2.0	1.6	3.8	15.1	4.0	18.5	3.3	11.7	8.9
7.0	27.4	9.4	36.2	10.2	37.9	8.9	33.8	5.7
11.7	39.0	14.5	39.1	15.5	39.5	13.9	39.2	0.3
17.0	39.9	20.2	39.3	20.8	40.1	19.3	39.8	0.4
22.7	39.9	25.3	40.8	25.3	41.3	24.4	40.7	0.8
28.0	39.7	29.5	38.9	29.7	39.9	29.0	39.5	0.6
33.0	37.3	34.6	38.1	34.4	38.0	34.0	37.8	0.4

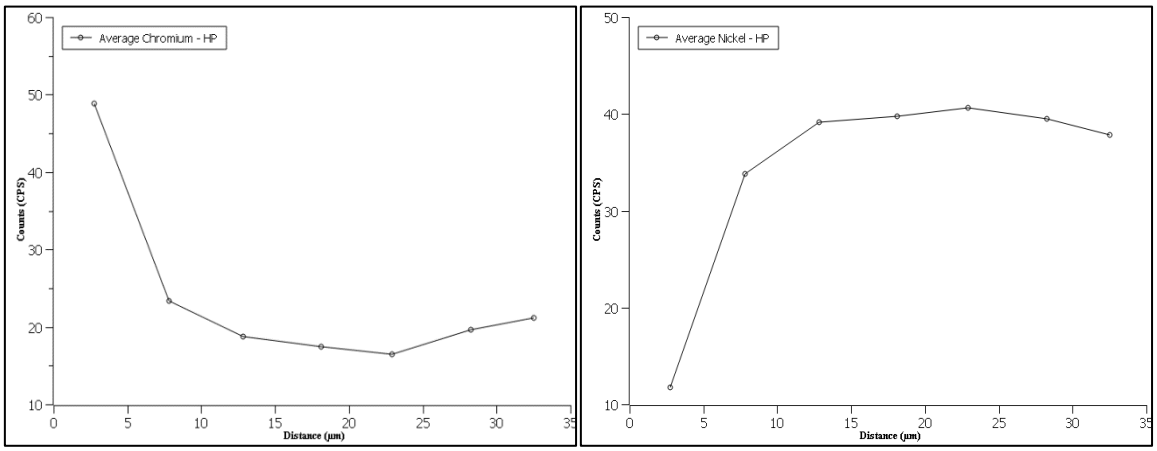

Figure 60. HP alloy scans for chromium content (left) and nickel content (right) for 1000 hours at 900°C.

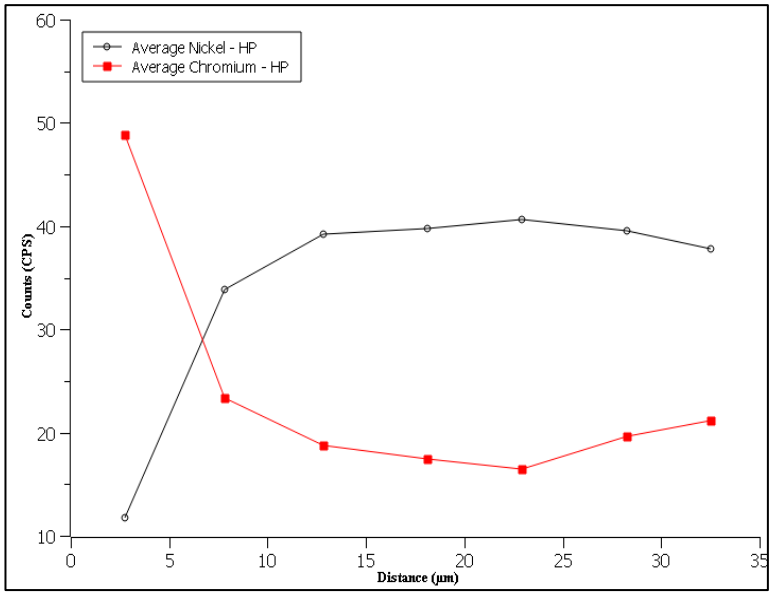

Figure 61. HP alloy scans of both nickel and chromium comparison for 1000 hours at 900°C

Tables 9 and 10 show the tabulated values of each element in the HP alloy along with the calculated average and standard deviation. The content of chromium matches well with SEM images of the oxide layer that is formed for HP. Nickel content also decreases at the surface due to the presence of the oxide layer being formed.

The same process that was performed on the HP alloy was done for the AFA – 2.6%. For AFA – 2.6%, two locations were scanned. Location 1 was scanned with the same process as HP, but location 2 scans differed slightly. Each of location 2's box area scans were done three times to obtain an average. Figure 62 and table 11 show the images of the box area scans and tabulated values for location 1. Figure 63 and table 12 shows the images of the box area scans and tabulated values for location 2.

Table 11. Box area scans of AFA – 2.6% with tabulated aluminum values below based on distance from the top layer of oxide. Oxidation is done at 900°C for 1000 hours.

Location 1	
Distance	Aluminum Content
2.1	17.9
5.6	2.4
9.5	2.2
15.4	2.0
20.1	1.7
25.8	1.6
31.1	1.9
35.2	1.8

AFA – 2.6%
Location 1
900°C

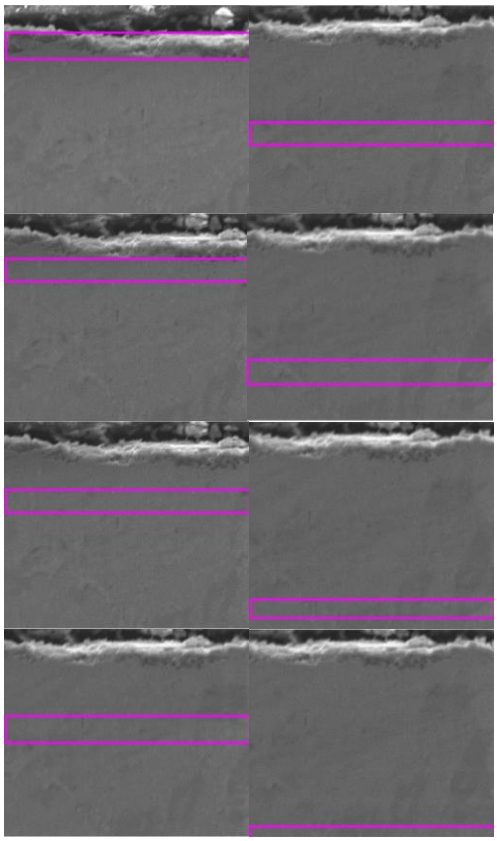

Figure 62. Box area scans for AFA-2.6% at 900°C for 1000 hours.

Table 12. Box area scans of AFA – 2.6% with tabulated aluminum values below based on distance from the top layer of oxide. Oxidation is done at 900°C for 1000 hours.

AFA - 2.6% - Location 2

Distance A	Al A	Distance B	Al B	Distance C	Al C	Average Al	Average Distance	S.D. Al
2.7	7.0	3.0	9.7	2.5	11.8	9.5	2.7	2.4
8.2	2.1	7.4	2.3	7.9	3.2	2.5	7.8	0.6
12.4	2.0	13.0	2.6	13.1	2.1	2.2	12.8	0.3
18.1	1.6	18.0	2.1	18.3	2.4	2.1	18.1	0.4
22.7	2.2	23.1	2.4	23.0	2.5	2.3	22.9	0.1
28.1	2.3	28.4	2.4	28.3	2.4	2.4	28.3	0.1
32.4	2.3	32.2	2.4	33.1	2.0	2.2	32.6	0.2

AFA – 2.6%
Location 2
900°C

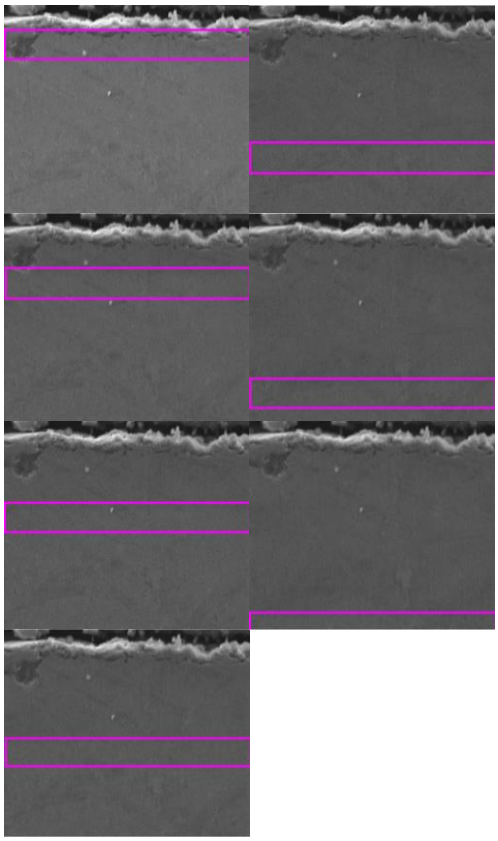

Figure 63. Box area scans for AFA-2.6% at 900°C for 1000 hours.

The tabulated averages for AFA – 2.6% and HP alloy was then plotted to the graphs below in figures 64 and 65. Averages of chromium and nickel were obtained from tables 13 and 14.

Table 13. Box area scans of AFA – 2.6% with tabulated chromium values below based on distance from the top layer of oxide. Oxidation is done at 900°C for 1000 hours.

AFA - 2.6% - Location 2 - Chromium

Distance A	Chromium A	Distance B	Chromium B	Distance C	Chromium C	Average Distance	Average Cr	S.D. Cr
2.7	28.9	3.0	27.4	2.5	26.2	2.7	27.5	1.4
8.2	24.4	7.4	24.6	7.9	25.1	7.8	24.7	0.4
12.4	26.3	13.0	26.3	13.1	25.3	12.8	26.0	0.6
18.1	28.4	18.0	27.6	18.3	28.2	18.1	28.1	0.4
22.7	26.2	23.1	27.2	23.0	26.4	22.9	26.6	0.5
28.1	27.4	28.4	27.5	28.3	27.4	28.3	27.4	0.0
32.4	26.1	32.2	26.1	33.1	27.3	32.5	26.5	0.7

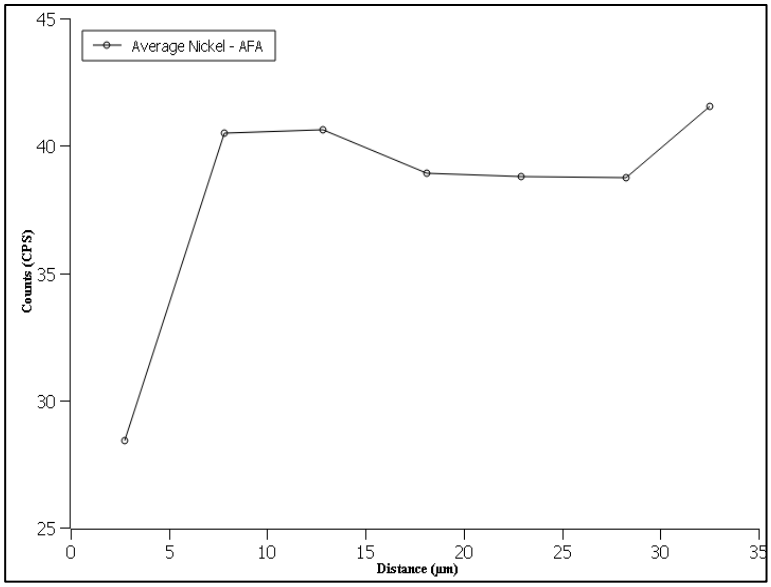

Figure 64. Average nickel content for AFA – 2.6% done at 900°C for 1000 hours.

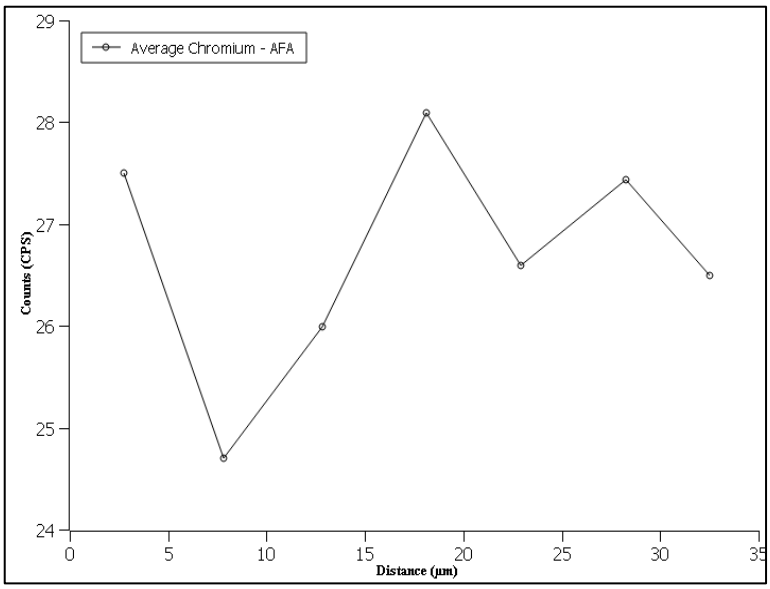

Figure 65. Average chromium content for AFA – 2.6% done at 900°C for 1000 hours.

Table 14. Box area scans of AFA – 2.6% with tabulated Nickel values below based on distance from the top layer of oxide. Oxidation is done at 900°C for 1000 hours.

AFA - 2.6% - Location 2 - Nickel

Distance A	Nickel A	Distance B	Nickel B	Distance C	Nickel C	Average Distance	Average Ni	S.D. Ni
2.7	31.3	3.0	28.1	2.5	25.9	2.7	28.4	2.7
8.2	41.4	7.4	40.3	7.9	39.9	7.8	40.5	0.8
12.4	41.1	13.0	40.2	13.1	40.5	12.8	40.6	0.5
18.1	38.7	18.0	39.9	18.3	38.2	18.1	38.9	0.9
22.7	38.8	23.1	39.0	23.0	38.5	22.9	38.8	0.2
28.1	39.0	28.4	38.8	28.3	38.4	28.3	38.7	0.3
32.4	41.2	32.2	41.7	33.1	41.7	32.5	41.5	0.3

The aluminum content was also plotted as well for location 1 and location 2. Location 1 aluminum profile was plotted and compared to location 2. Although location 1 was only scanned once, the plots do match well with each other. Figure 66 shows the location1 and location 2 of the aluminum profile comparison and figure 67 shows the overall comparison of the elements for AFA – 2.6% and their profiles for location 2.

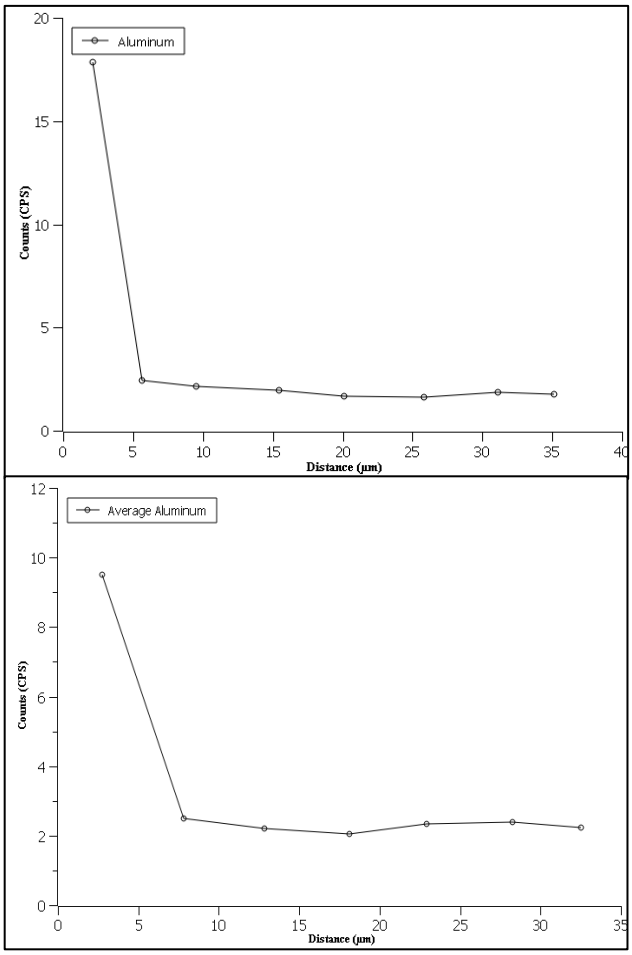

Figure 66. AFA – 2.6% aluminum profiles for location 1 and location 2 done at 900°C for 1000 hours.

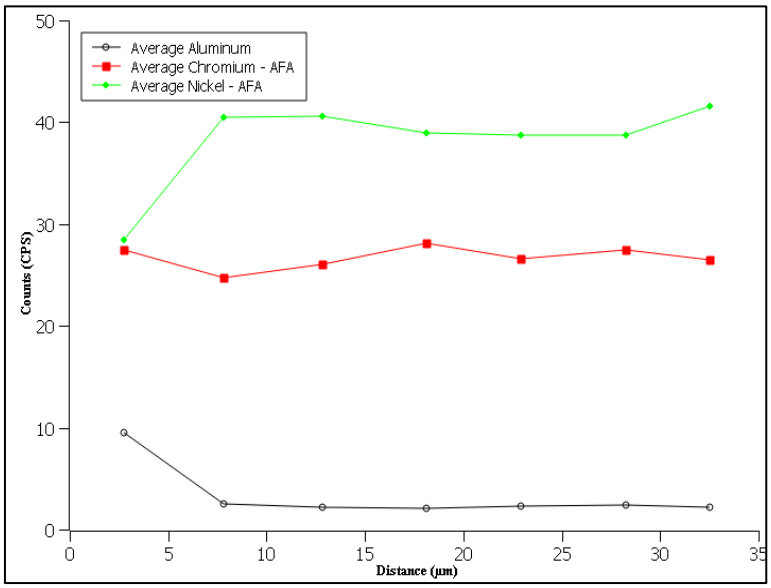

Figure 67. AFA – 2.6 element profiles for location 2 done at 900°C for 1000 hours.

5.6 Summary

The aluminum content and other elements of AFA – 2.6% and HP alloy was evaluated for 100 hours and 1000 hours. Aluminum, chromium, and nickel content was tracked across 30μm via SEM-EDS. Element content was first performed with line scans however after analysis, it was determined box area scans represented the overall element content better. This is due to the reason that the oxidized sample is not uniform across. Some areas may present more intermetallic that can result in a higher value of chromium than another line scan. To account for this variation, box area scans were done as it can capture more than a single point of data. This will represent the element content better than the actual depth of the sample.

Aluminum content was found to be higher at the oxide scale which matches well with other results confirming the oxide scale. From the oxide scale, aluminum content does taper off and stays relatively constant. For nickel content, there is a decrease in nickel content at the oxide layer where it forms for both HP and AFA – 2.6%. For chromium content, the AFA – 2.6% shows chromium content that is near the bulk composition and for the HP alloy, it shows an increase in chromium content. At 1000 hours, AFA – 2.6% is forming alumina at the surface and hence the aluminum content is changed to form alumina while chromium remains the same. For the HP alloy, since chromia is the main oxide former, it will have an increase in chromium content due to the formation of the chromia.

This project showed the first step in understanding how aluminum works with the oxide formation but does not reflect depletion rates. There has been a determination with this chapter that further study is needed to study the depletion rate of aluminum and other elements. At 1000 hours, the data presented here shows that the samples are still performing like the 100-hour cycles. A proposed study of increasing the oxidation time to 10,000 hours or close to a year's

worth of oxidation is suggested. There is a hypothesis that at that range of time, there will be depletion occurring.

Chapter V

Oxidation Performance on Welded Surface

The goal of this chapter is to assess welded regions of HP and AFA – 2.6% alloys. In industry, the steel tubes are welded together to make the final reactor. It is very common for industries/foundries to weld the tubes together. The objective is to take samples of both HP and AFA – 2.6% and have them autogenously welded on the inner diameter section of the sample. After welding, the samples will be then oxidized along with non-welded baseline samples. This study will provide valuable insight to the oxidation kinetics performance of the welded regions and be of use for a deciding factor in its potential use in industries. The samples will be oxidized for 100 hours with mass change tracking per 10-hour cycle. The test will be run at the standard three temperatures of 800°C, 850°C, and 900°C. The oxidation environment was selected to be pure steam.

6.1 Introduction

In practical applications, welds may need to be performed for design aspects and/or repair situations. At the weld the weld experiences strain and strain that subject the pipes to different mechanical issues. Additionally, the weld also introduces chemical compatibility issues with different weld materials that may lead to lesser corrosion resistance. There have been some studies on welding material where the weld material is doped with rare earth metals to improve corrosion resistance. Samanta el al. looked at the effect of rare earth metals and their oxidation behavior in tungsten inert gas welds on AISI 316L stainless steels [40]. Results showed that the addition of rare earth metals does improve oxidation resistance, however the weld zone is still less protective than the base metal at high temperatures. Extending this issue, the goal is to weld AFA metals together and oxidize and characterize the weld zone. A comparison will be made to see how the performance holds compared to unwelded material.

6.2 Methodology

In this chapter, the process of prepping samples for oxidation experiments was kept the same. Once the samples were prepped as usual for oxidation experiments, they would be autogenously welded first before oxidation. Samples were kept to roughly the same dimensions as previous chapters as well. The welds that were created on the samples were made across the sample as seen in figure 68. Welds were performed autogenously with a TIG welder.

Figure 68. Schematic drawing of location of welds on samples before oxidation.

In this chapter, AFA – 2.6% and HP alloy will be used again and compared to each other and the non-welded samples. Experiments were done at 800°C, 850°C, and 900°C in pure-steam

oxidizing environment. Microstructure results were also etched with the same etchant before chapters with 20wt% nitric acid and 4wt% hydrofluoric acid.

6.3 Microstructure Analysis

Microstructures were obtained optically and via SEM. The welded areas did show a different microstructure. Figure 69 shows the non-welded microstructure of AFA – 2.6% compared to the welded microstructure. Here the welded microstructure shows much finer grain size compared to the non-welded. There is still directionality that is caused from the welding as well. In addition to the comparison of the non-weld to welded, comparison of the welded microstructure was looked at across the oxidized temperatures. Figure 70 shows the comparison of the welded microstructure at 800°C, 850°C, and 900°C for AFA 2.6%.

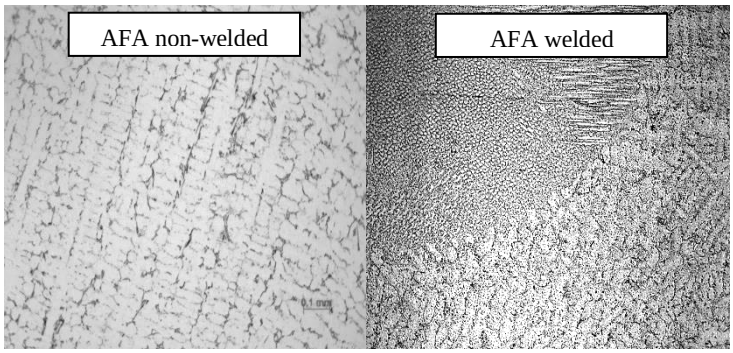

Figure 69. AFA – 2.6% non-welded versus welded microstructure.

Like the study in chapter 3, the temperature does not affect the microstructure as it does not reach high enough to cause a microstructural change. Across all temperature ranges, the welded microstructure displays finer grains than the non-welded microstructure. It should also be noted that the microstructure for HP alloy is similar and is not affected by the temperature range used in the pure-steam oxidation.

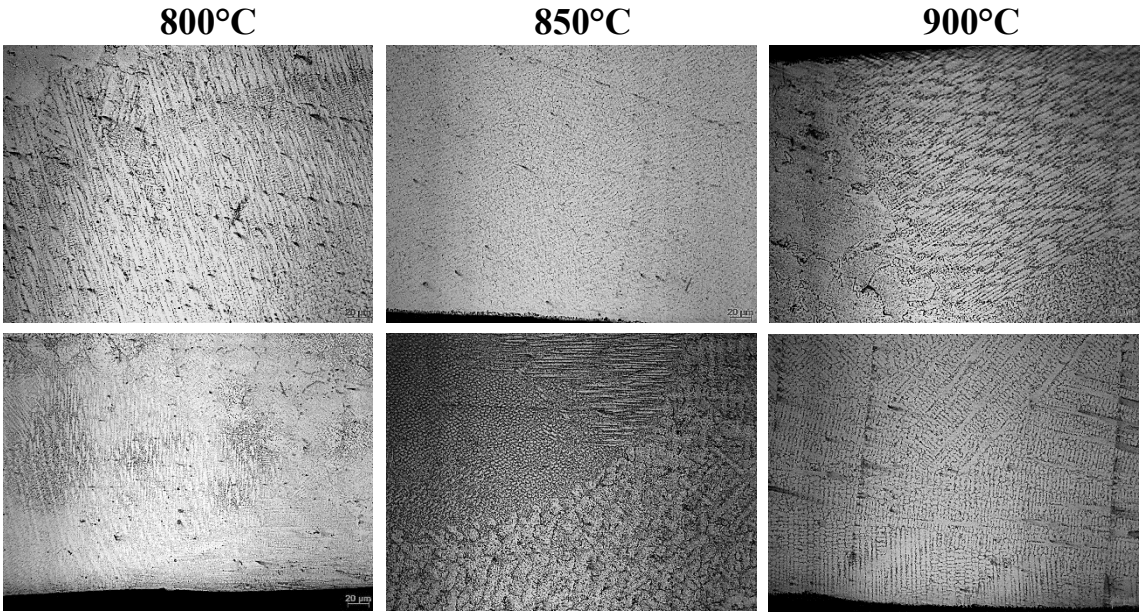

Figure 70. AFA – 2.6% microstructure of the welded regions across the tested temperatures.

Additional analysis of the welded regions was also looked at via SEM. Determination of visually what the welded regions look like under SEM was performed. Images of welded regions match well with the optical microstructures. Figure 71 shows the AFA – 2.6% and HP alloy SEM images at 800°C. Figure 72 shows the AFA – 2.6% and HP alloy SEM images at 850°C. Lastly, figure 73 shows the AFA – 2.6% and HP alloy SEM images at 900°C.

HP – 800°C

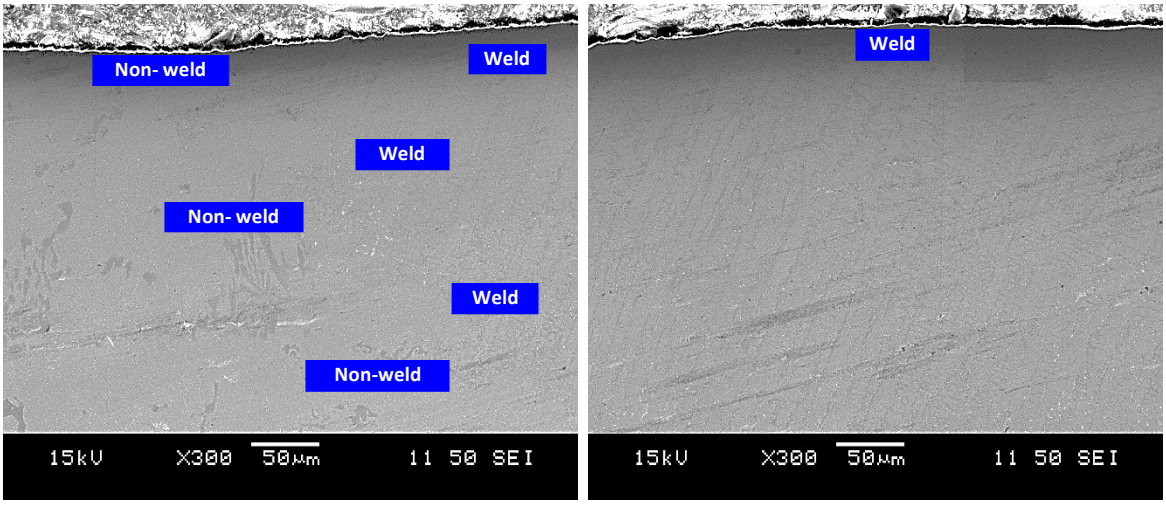

AFA 2.6% – 800°C

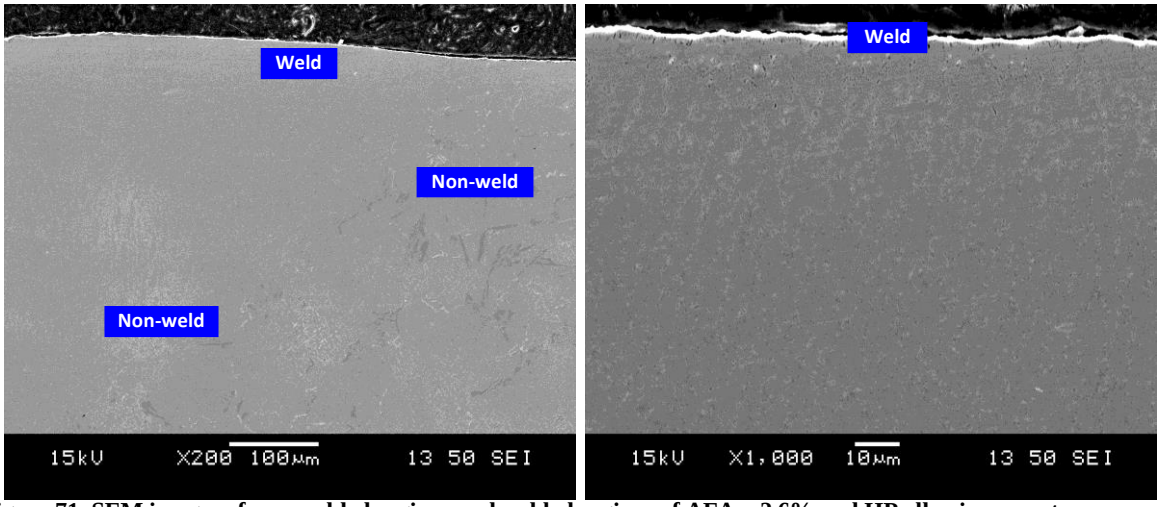

Figure 71. SEM images of non-welded regions and welded regions of AFA – 2.6% and HP alloy in pure-steam.

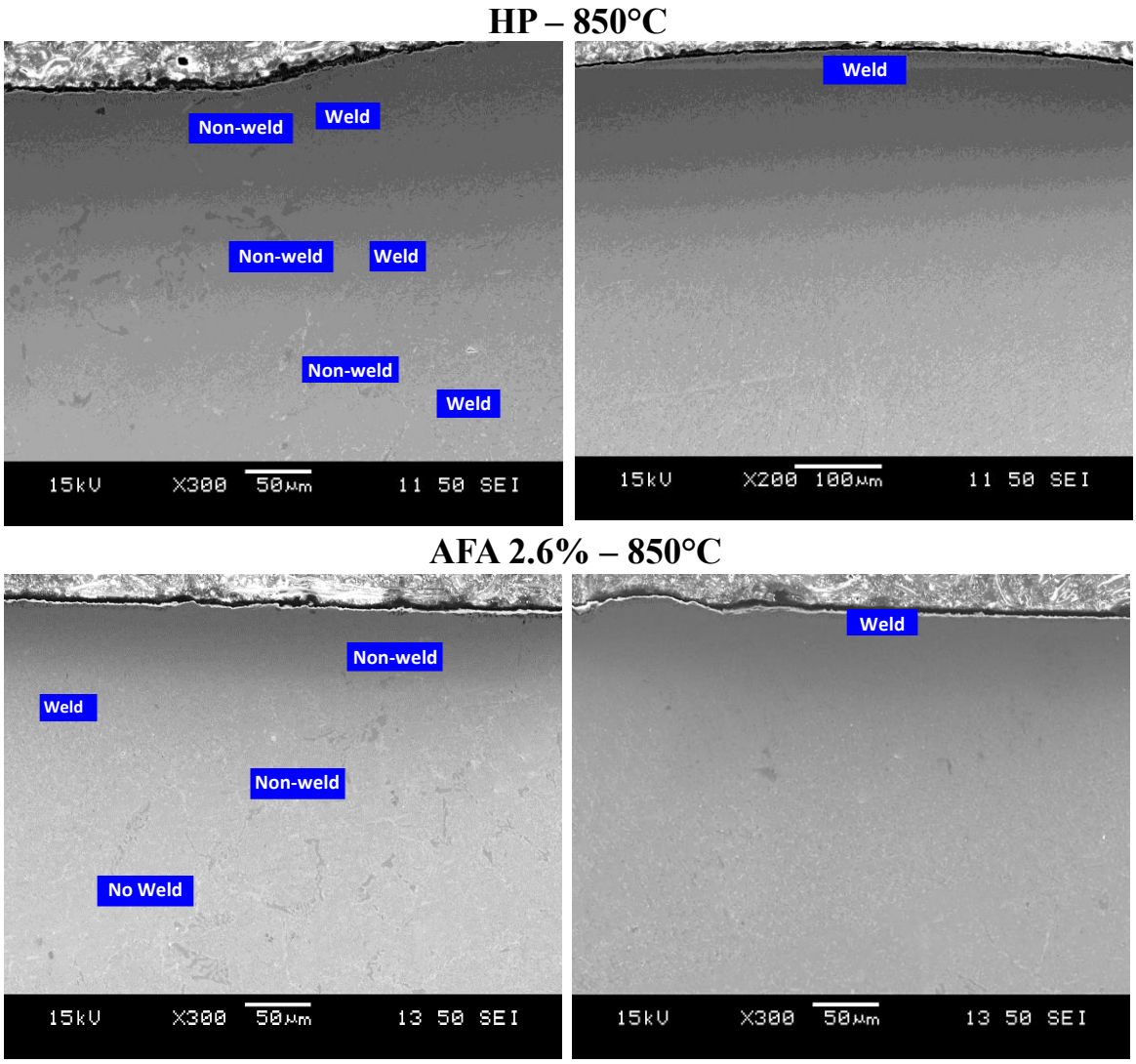

Figure 72. SEM images of non-welded regions and welded regions of AFA – 2.6% and HP alloy in pure-steam.

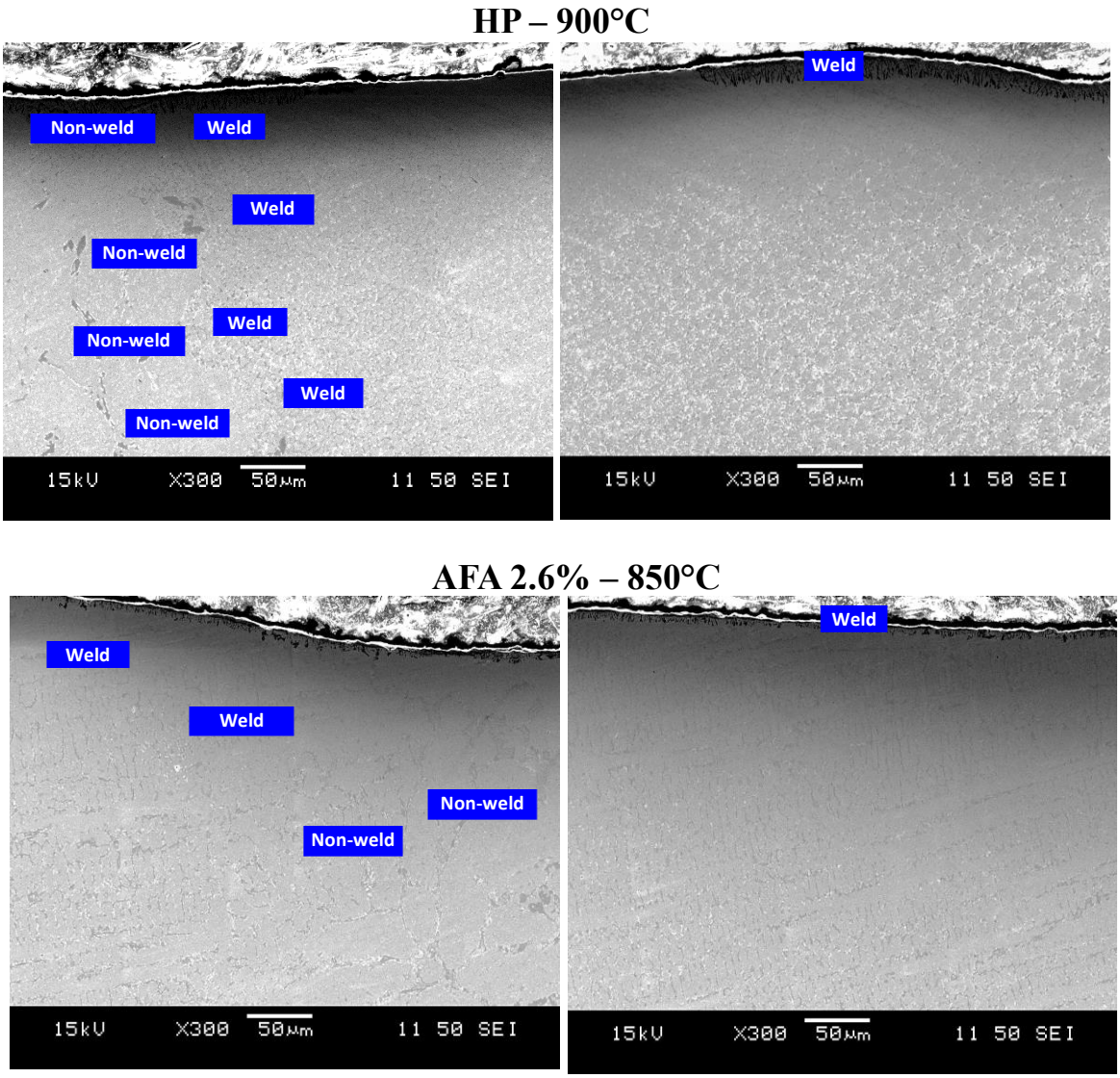

Figure 73. SEM images of non-welded regions and welded regions of AFA – 2.6% and HP alloy in pure-steam.

6.4 Line Scan of Non-weld and Welded Regions

In addition to the microstructure analysis. Line scans were performed via SEM-EDS to characterize the surface chemistry. Line scans were performed over welded samples to see if the same intermetallic phases appear as the non-welded. In the SEM images, the dark spots were determined to be rich in chromium. The line scans that follow over the areas match well with the finer grains on the welded samples as well. Figure 74 shows an example of a line scan that was performed on AFA – 2.6% at 800°C on a welded and non-welded sample. In summary, all other

temperatures for both AFA – 2.6% and HP alloy presented the same consistency with the chromium rich phase.

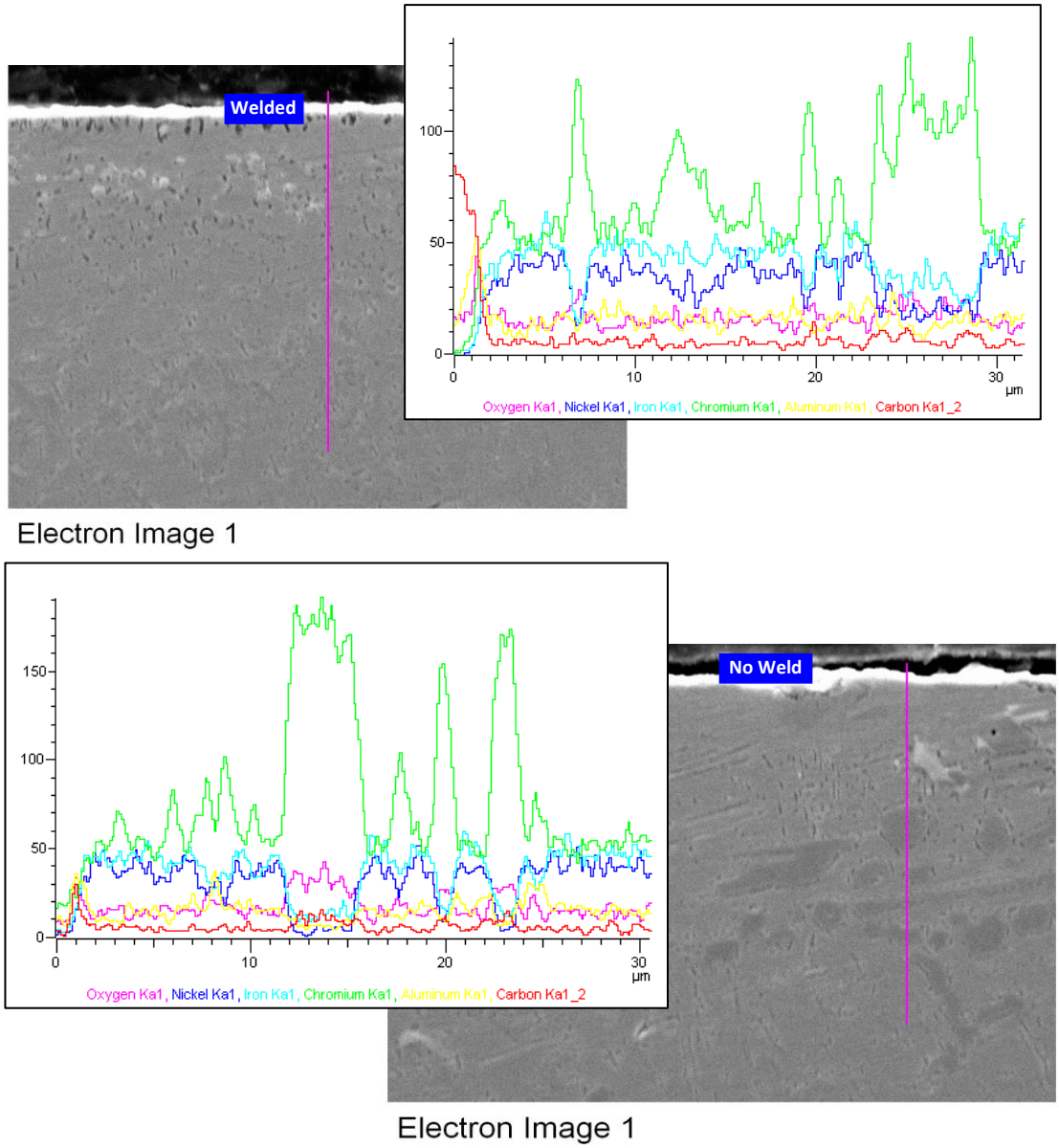

Figure 74. AFA – 2.6% line scan of welded and non-welded region showing chromium rich phase.

6.5 Mass Change Analysis

Mass changes were obtained for the welded and non-welded samples for the AFA – 2.6% and HP alloy. Figure 75 shows the average mass change comparison of the welded and non-welded samples from 800°C, 850°C, and 900°C. For the case of the AFA – 2.6% mass change, the data of the welded samples had similar mass change and oxidation kinetics. This makes sense as it maintains the same chemistry even though there is a microstructural change. Due to the same chemistry, the autogenous weld on the AFA-2.6% samples does not negatively impact the corrosion resistance.

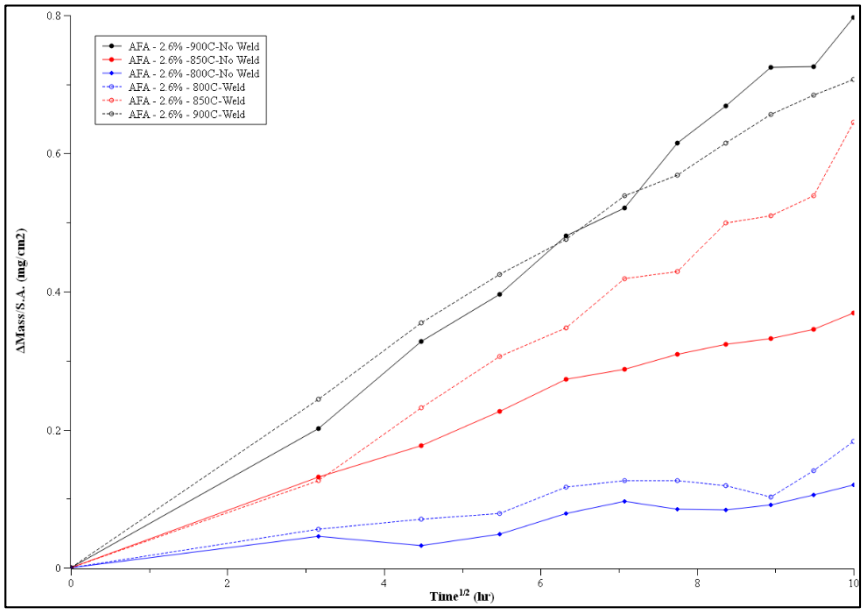

Figure 75. The average mass change of AFA – 2.6% of welded and non-welded samples.

For the case of the HP alloy, the mass change data or oxidation kinetics improved slightly at the middle range temperature of 850°C and 800°C. In this case, HP did not experience mass loss but rather a small positive mass change. The largest contrast in results here was the 900°C range for welded and non-welded samples. In the pure-steam experiment with non-weld, HP experienced significant mass loss due to spallation of chromia. In the case of the welded sample,

it experiences the opposite effect where it had positive mass change. Figure 76 shows the average mass change comparison of HP alloy between the temperatures.

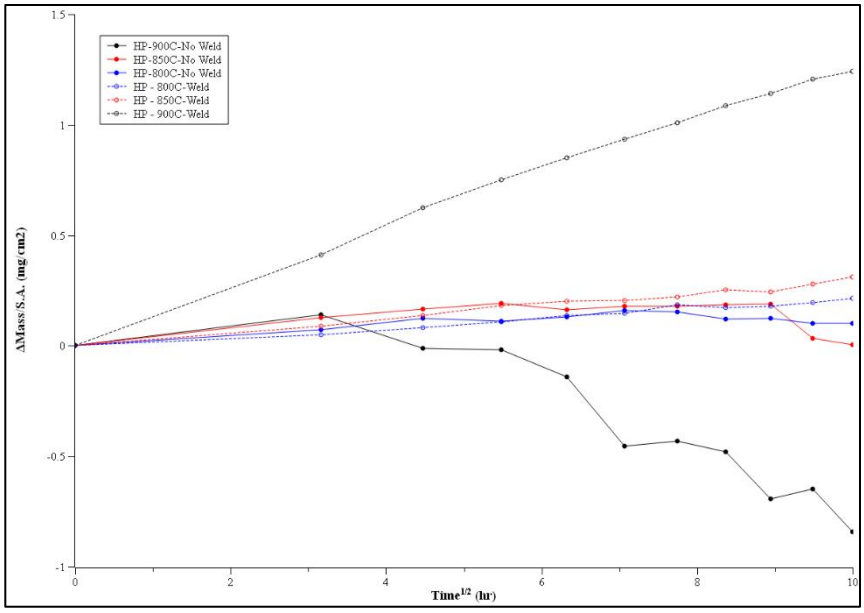

Figure 76. The average mass change of HP of welded and non-welded samples.

6.6 Summary

In this chapter, the oxidation performance of welded regions was evaluated and compared to the non-welded samples. Microstructural changes were observed due to the autogenous welding on the samples. Microstructural changes were observed between welded and non-welded however there was no difference in welded microstructure with respect to temperature. The microstructure of the welded region had much finer grain size compared to non-welded samples. SEM analysis of the welded microstructure was also performed to match with the optical results.

Line scans via SEM-EDS were also performed on both welded and non-welded samples. The dark phases found on SEM images were rich in chromium and line scans reflected as so. The finer grain size in the welded region gave smaller chromium rich intermetallic than the non-

welded. Lastly, the mass change data was obtained from the welded samples and compared to the non-welded samples in pure steam. With similar chemistry, the corrosion resistance of the AFA-2.6% samples did not have a negative impact. In the case of HP alloy, the corrosion resistance improved with no mass loss due to spallation in the welded samples. Welded samples overall had no significant change to the oxidation kinetics compared to pure steam.

Chapter V II

Conclusion

In this dissertation, the oxidation kinetics and performance of several AFA alloys were compared to the HP alloy. Alloys were prepped accordingly before the respective experiments. The experiments tested were pure steam, air-steam ratios, long-term oxidation, and pure steam oxidation on welded regions. Pure steam, air-steam ratios, and pure steam oxidation on welded regions were tested at 800°C, 850°C, and 900°C for 100 hours. The air-steam ratios tested two different flow rates of air at 4ml/min and 50 ml/min. The long-term oxidation experiment carried out an oxidation experiment that lasted for 1000 hours at 900°C. Element profiles were obtained in all experiments and specific elements were tracked in the long-term oxidation experiment. Results also included oxidation kinetics of mass change data, determination of time exponent of rate law, reaction rate constants, and activation energies.

It was observed that HP in pure steam oxidation did not perform well compared to the AFA. HP experienced spallation and contributed to its mass loss and validity of the mass change

data. In the air-steam ratios, HP still had the same issues as pure steam with mass loss whereas AFA performed relatively similar. The addition of air in the oxidation experiment did simulate real world conditions, however it did not affect the performance of the AFA. Welded regions of AFA also performed similarly to the non-welded regions as well. HP did experience a slight improvement to its oxidation kinetics in the welded regions. In general, AFA did perform better in most cases compared to HP in the oxidizing experiments performed in the dissertation. Air-steam ratios and welding do not harm the corrosion resistance of AFA.

Oxidation rate kinetics were obtained for the pure steam and air-steam ratio experiments. The average activation energy for AFA in pure steam was found to be 345.5 kJ/mol and the activation energy for HP was found to be 195.6 kJ/mol from the experimental data. These values do reflect well from the literature and are found to be within respectable range. The larger activation energy of AFA compared to HP also reflects well in the literature and Ellingham diagram. For the air-steam ratios, the average activation energy for AFA for 1:100 was 214.7 kJ/mol and for 1:10 was 291.4 kJ/mol. HP had a calculated activation energy of 270.7 kJ/mol for 1:100 and 71.6 kJ/mol for 1:10.

In the long-term oxidation and aluminum tracking, it was determined that longer oxidation times were required to see depletion rates in aluminum, nickel, and chromium. Aluminum was tracked with box area scans to capture the average aluminum concentration per area box scan. From the average values, it was plotted. Aluminum concentration matched well to the pure steam and air-steam ratio line scans of showing the oxide. Chromium and nickel profiles were also generated as well.

7.1 Application of AFA

One of the main goals of the research project is to provide an answer to industries if AFA is a viable replacement and/or use of new alloy for petrochemical processes. The collective data and results of this dissertation has done a significant amount of work to prove the oxidation kinetics and resistance of AFA is at the minimal same or better than HP (current use of alloy for petrochemical industries). Not only did the AFA perform better in terms of air-steam ratios (conditions that are like what industries use), it also can serve in a larger range of conditions such as temperature and corrosive environments. In summary, the data and results complied in this dissertation argues strongly that AFA should be considered and is a viable replacement of the HP (CFA) alloy for steel reactors in petrochemical industries.

7.2 Future Work

It is not without a doubt that further study is needed to continue to improve the understanding and application of AFA. As mentioned earlier in chapter 5, there needs to be a longer oxidation time to see aluminum depletion rates. This would provide valuable data to confidently answer the life cycle use of the AFA and begin to derive experimental diffusion coefficients of aluminum and other major alloying elements. Other future work that needs to be addressed is understanding the design aspect of the AFA. Determining optimal oxide thickness to minimize maintenance on steel reactors and/or improve efficiency of the production is of another high interest.

Another improvement that can be made is improving the overall activation energy calculations. In this study, three temperatures were selected which in term gives three reaction rate constants. Some papers do tests at a larger temperature range and as such can give more reliable data or reflective data of the true value.

7.3 Acknowledgements

SEM-EDS and XRD were all performed at the Advanced Analysis Facility at the University of Wisconsin-Milwaukee. Sample materials were provided by MetalTek International. The project was partially funded by ARPA-E; DE-AR0000690 and the UW-Milwaukee Advanced Opportunity Program.

References

1. “Ethane Production Expected to Increase as Petrochemical Consumption and Exports Expand - Today in Energy - U.S. Energy Information Administration (EIA).” Accessed November 12, 2018. https://www.eia.gov/todayinenergy/detail.php?id=25632.
2. Dorcheh, A. S., & Galetz, M. C. (2016). Challenges in developing oxidation-resistant chromium-based alloys for applications above 900°C. JOM, 68(11), 2793–2802. https://doi.org/10.1007/s11837-016-2079-7
3. Gulbransen, E. A., & Andrew, K. F. (1957). Kinetics of the oxidation of chromium. Journal of The Electrochemical Society, 104(6), 334. https://doi.org/10.1149/1.2428576
4. Kofstad, P., & Lillerud, K. P. (1980). On high temperature oxidation of chromium: II . properties of and the oxidation mechanism of chromium. Journal of The Electrochemical Society, 127(11), 2410–2419. https://doi.org/10.1149/1.2129481
5. Mejlbro, Leif. The Complete Solution of Fick’s Second Law of Diffusion with Time-Dependent Diffusion Coefficient and Surface Concentration. Cementa, 1996.
6. Conti, Franco, and George Eisenman. “The Non-Steady-State Membrane Potential of Ion Exchangers with Fixed Sites.” Biophysical Journal 5, no. 2 (March 1965): 247–56. https://doi.org/10.1016/S0006-3495(65)86714-5.
7. Daniel Monceau, Bernard Pieraggi. Determination of Parabolic Rate Constants from a Local Analysis of Mass-Gain Curves. Oxidation of Metals, 1998, 50 (5 - 6), pp.477-493. ff10.1023/A:1018860909826ff. ffhal-03607751f
8. Langevoort, J.C., L.J. Hanekamp, and P.J. Gellings. “On the Kinetics of Oxidation of Austenitic Stainless Steels AISI 304 and Incoloy 800H.” Applied Surface Science 28, no. 3 (May 1987): 189–203. https://doi.org/10.1016/0169-4332(87)90121-8.
9. Talekar, Anjali, Dhanesh Chandra, Raja Chellappa, Jaak Daemen, Nobumichi Tamura, and Martin Kunz. “Oxidation Kinetics of High Strength Low Alloy Steels at Elevated Temperatures.” Corrosion Science 50, no. 10 (October 1, 2008): 2804–15. https://doi.org/10.1016/j.corsci.2008.08.008.
10. Grosvenor, A. P., B. A. Kobe, and N. S. McIntyre. “Activation Energies for the Oxidation of Iron by Oxygen Gas and Water Vapour.” Surface Science 574, no. 2 (January 10, 2005): 317–21. https://doi.org/10.1016/j.susc.2004.10.043.

11. Abuluwefa, H. T., R. I. L. Guthrie, and F. Ajersch. “Oxidation of Low Carbon Steel in Multicomponent Gases: Part I. Reaction Mechanisms during Isothermal Oxidation.” Metallurgical and Materials Transactions A 28, no. 8 (August 1, 1997): 1633–41. https://doi.org/10.1007/s11661-997-0255-7.
12. Chen, R.Y., and W.Y.D. Yeun. “Review of the High-Temperature Oxidation of Iron and Carbon Steels in Air or Oxygen.” Oxidation of Metals 59, no. 5 (June 1, 2003): 433–68. https://doi.org/10.1023/A:1023685905159.
13. Adomako, N. K., Kim, J. H., & Hyun, Y. T. (2018). High-temperature oxidation behaviour of low-entropy alloy to medium- and high-entropy alloys. *Journal of Thermal Analysis and Calorimetry*, *133*(1), 13–26. https://doi.org/10.1007/s10973-018-6963-y
14. Fujii, C. T., & Meussner, R. A. (1964). The mechanism of the high-temperature oxidation of iron-chromium alloys in water vapor. *Journal of The Electrochemical Society*, *111*(11), 1215. https://doi.org/10.1149/1.2425963
15. Bittel, J. T., L. H. Sjodahl, and J. F. White. “Oxidation of 304L Stainless Steel by Steam and by Air.” CORROSION 25, no. 1 (January 1, 1969): 7–14. https://doi.org/10.5006/0010-9312- 25.1.7.
16. Gesmundo, F, and F Viani. “Application of Wagner’s Theory to the Parabolic Growth of Oxides Containing Different Kinds of Defects,” n.d., 10.
17. Cheng, X.-W., Z.-Y. Jiang, B. J. Monaghan, R. J. Longbottom, D.-B. Wei, A. C. Hee, and L.- Z. Jiang. “Degradation of Ferritic Stainless Steels at 1200 °C in Air.” Materials and Corrosion 69, no. 1 (January 1, 2018): 63–75. https://doi.org/10.1002/maco.201709577.
18. Tedmon, C. S. “The Effect of Oxide Volatilization on the Oxidation Kinetics of Cr and Fe-Cr Alloys.” Journal of The Electrochemical Society 113, no. 8 (August 1, 1966): 766–68. https://doi.org/10.1149/1.2424115.
19. Sand, T. (2022). *High-Temperature Corrosion Properties of Chromia- and Alumina-Forming Alloys* (dissertation).
20. Quadakkers, W. J., D. Naumenko, E. Wessel, V. Kochubey, and L. Singheiser. “Growth Rates of Alumina Scales on Fe–Cr–Al Alloys.” Oxidation of Metals 61, no. 1 (February 1, 2004): 17–37. https://doi.org/10.1023/B:OXID.0000016274.78642.ae.

21. Jönsson, Bo, and Alla Westerlund. “Oxidation Comparison of Alumina-Forming and Chromia-Forming Commercial Alloys at 1100 and 1200 °C.” Oxidation of Metals 88, no. 3 (October 1, 2017): 315–26. https://doi.org/10.1007/s11085-016-9710-4.
22. Muralidharan, G., Y. Yamamoto, M. P. Brady, B. A. Pint, D. Voke, and R. I. Pankiw. “Development of Cast Alumina-Forming Austenitic Stainless Steel Alloys for Use in High Temperature Process Environments - OnePetro.” Dallas, Texas: NACE International, 2015. https://www.onepetro.org/conference-paper/NACE-2015-6114.
23. Muralidharan, G., Y. Yamamoto, M. P. Brady, L. R. Walker, H. M. Meyer III, and D. N. Leonard. “Development of Cast Alumina-Forming Austenitic Stainless Steels.” JOM 68, no. 11 (November 1, 2016): 2803–10. https://doi.org/10.1007/s11837-016-2094-8.
24. Yamamoto, Y., M.P. Brady, M.L. Santella, H. Bei, P.J. Maziasz, and B.A. Pint. “Overview of Strategies for High-Temperature Creep and Oxidation Resistance of Alumina-Forming Austenitic Stainless Steels.” Metallurgical and Materials Transactions A 42, no. 4 (April 1, 2011): 922–31. https://doi.org/10.1007/s11661-010-0295-2.
25. Prenzlow, E. A. (2016). *High Temperature Oxidation of Alumina Forming Cast Austenitic Stainless Steels Within an Environment of Pure Steam* (thesis).
26. Young, D. J., & Pint, B. A. (2006). Chromium volatilization rates from CR2O3 scales into flowing gases containing water vapor. *Oxidation of Metals*, *66*(3–4), 137–153. https://doi.org/10.1007/s11085-006-9030-1
27. Fromhold, A. T., & Fromhold, R. G. (1984). Chapter 1 an overview of metal oxidation theory. *Reactions of Solids with Gases*, 1–117. https://doi.org/10.1016/s0069-8040(08)70006-2
28. Lampke, T., Meyer, D., Alisch, G., Wielage, B., Pokhmurska, H., Klapkiv, M., & Student, M. (2011). Corrosion and wear behavior of alumina coatings obtained by various methods. *Materials Science*, *46*(5), 591–598. https://doi.org/10.1007/s11003-011-9328-2
29. Mirhashemihaghighi, S., Światowska, J., Maurice, V., Seyeux, A., Zanna, S., Salmi, E., Ritala, M., & Marcus, P. (2016). Corrosion protection of aluminium by ultra-thin atomic layer deposited alumina coatings. *Corrosion Science*, *106*, 16–24. https://doi.org/10.1016/j.corsci.2016.01.021

30. Raj, V., & Mubarak Ali, M. (2009). Formation of ceramic alumina nanocomposite coatings on aluminium for enhanced corrosion resistance. *Journal of Materials Processing Technology*, *209*(12–13), 5341–5352. https://doi.org/10.1016/j.jmatprotec.2009.04.004

31. *Ellingham H. J. T., J Soc Chem Ind (London)* ***63*** *125 (1944)*

32. Caplan, D., & Cohen, M. (1961). The volatilization of chromium oxide. *Journal of The Electrochemical Society*, *108*(5), 438. https://doi.org/10.1149/1.2428106

33. Rebak, R. B. (2017). Versatile oxide films protect FeCrAl alloys under normal operation and accident conditions in light water power reactors. *JOM*, *70*(2), 176–185. https://doi.org/10.1007/s11837-017-2705-z

34. Karthikeyan, R., Seshadri, S., Sarma, V. S., & Kamaraj, M. (2023). Long-exposure air and steam oxidation characteristics of in 617 alloys. *Corrosion and Materials Degradation*, *4*(1), 90–103. https://doi.org/10.3390/cmd4010006

35. Ping, S. B., Xie, F., Wang, R. K., Zheng, Z. J., & Gao, Y. (2016). Diffusion Kinetics of Chromium in a novel Super304H stainless steel. High Temperature Materials and Processes, 36(2), 175–181. https://doi.org/10.1515/htmp-2015-0227

36. Tsai, J. C. C. (1969). Shallow phosphorus diffusion profiles in Silicon. *Proceedings of the IEEE*, *57*(9), 1499–1506. https://doi.org/10.1109/proc.1969.7325

37. Benzarti, Z., Halidou, I., Bougrioua, Z., Boufaden, T., & El Jani, B. (2008). Magnesium diffusion profile in gan grown by MOVPE. *Journal of Crystal Growth*, *310*(14), 3274–3277. https://doi.org/10.1016/j.jcrysgro.2008.04.008

38. Pillai, R., Jalowicka, A., Galiullin, T., Naumenko, D., Ernsberger, M., Herzog, R., & Quadakkers, W. J. (2019). Simulating the effect of aluminizing on a conicraly-coated ni-base superalloy. *Calphad*, *65*, 340–345. https://doi.org/10.1016/j.calphad.2019.04.004

39. Maréchal, L., Lesage, B., Huntz, A.M. *et al.* Oxidation Behavior of ODS Fe–Cr–Al Alloys: Aluminum Depletion and Lifetime. *Oxidation of Metals* **60**, 1–28 (2003). https://doi.org/10.1023/A:1024604428747

40. Samanta, S. K., Mitra, S. K., & Pal, T. K. (2006). Effect of rare earth elements on microstructure and oxidation behaviour in TIG weldments of Aisi 316L Stainless Steel. *Materials Science and Engineering: A*, *430*(1–2), 242–247. https://doi.org/10.1016/j.msea.2006.05.063